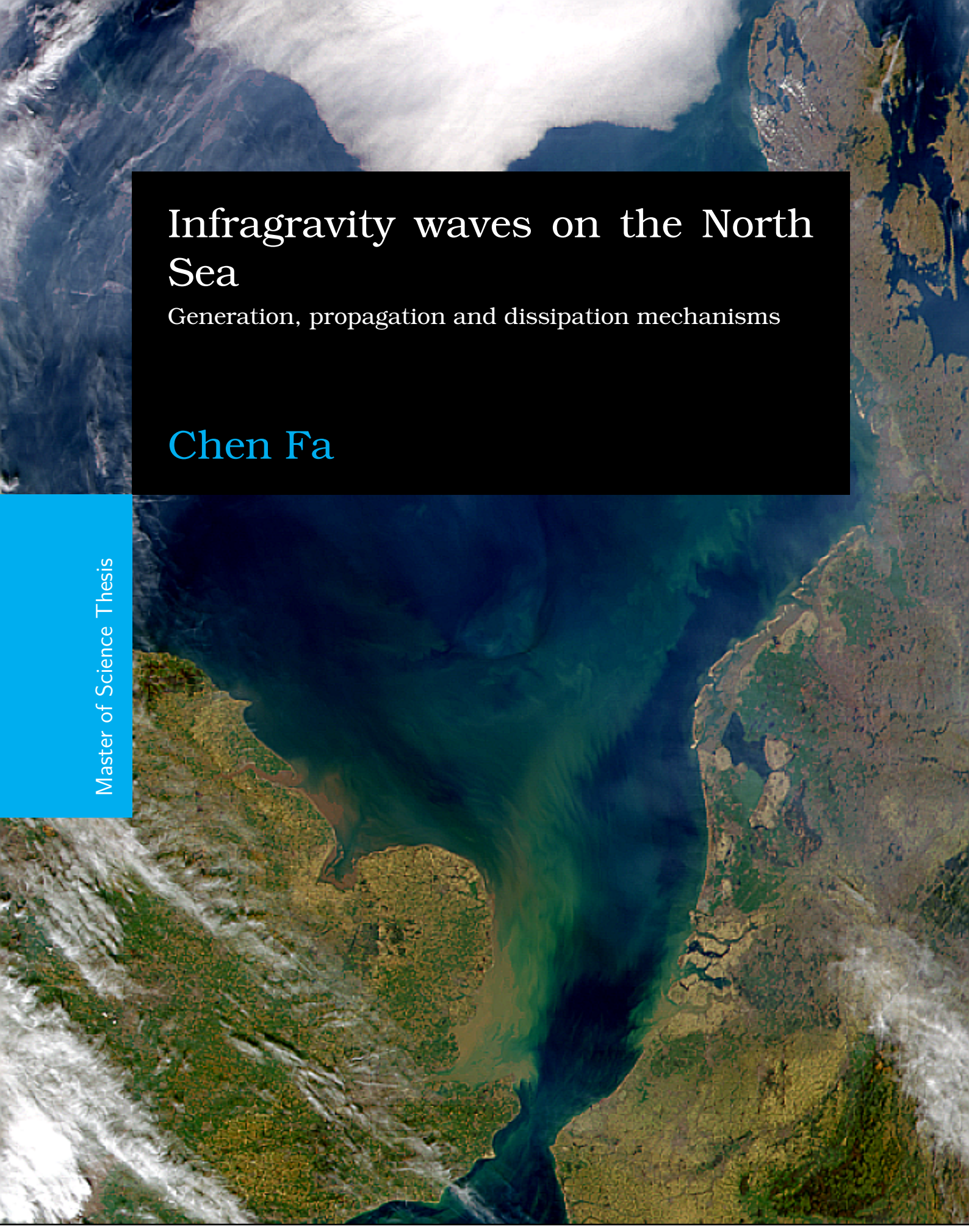

Infragravity waves on the North Sea

Generation, propagation and dissipation mechanisms

Chen Fa

Master of Science Thesis

TU Delft Delft University of Technology

Infragravity waves on the North Sea

Generation, propagation and dissipation mechanisms

Master of Science Thesis

For the degree of Master of Science in Coastal Engineering at Delft University of Technology

Chen Fa

October 5, 2021

Faculty of Civil Engineering and Geosciences (CEG) · Delft University of Technology

Delft University of Technology
Department of
Hydraulic Engineering

The undersigned hereby certify that they have read and recommend to the Faculty of Civil Engineering and Geosciences (CEG) for acceptance a thesis entitled

Infragravity waves on the North Sea

by

Chen Fa

in partial fulfillment of the requirements for the degree of

Master of Science Coastal Engineering

Dated: October 5, 2021

Supervisor(s):

Prof.dr.ir. A.J.H.M. Reniers, Chair

Dr.ir. D.P. Rijnsdorp, Daily Supervisor

Reader(s):

Dr.ir. M.F.S. Tisser

Dr.ir. M. Zijlema

Dr. ir. M.A. de Schipper

Abstract

Recent analysis on measurements in the North Sea has shown a large amount of wave energy ranging in infragravity bands in the North Sea during storm events. To better understand the generation and propagation of free infragravity waves, the SWAN model is used to inspect the infragravity wave pattern, the infragravity wave origins, and the corresponding contribution from different coastlines in the North Sea. The local equilibrium between sea swell wave and infragravity wavebands is applied to parameterize the source infragravity wave along the coastlines bordering the North Sea following the approach of Arduin et. al. (2014). The empirical parameter α_1 representing the radiating energy level from each coastline and bottom friction coefficient χ representing the dissipation strength are combined to calibrate the model. 10 storm events with an observed infragravity wave height over 10cm are chosen to gain detailed insight into the evolution of free infragravity waves under extreme conditions in SWAN.

A correlation between α_1 and χ is found. A relatively good explanation between measured and predicted infragravity wave height can be obtained as long as a large α_1 and a large χ are implemented in the model or vice versa, showing an accuracy of up to 78% in the open sea.

Based on a proper combination of two variables, the contribution of infragravity energy from each coastline varies spatially in predicted results. The Danish coastline is the dominant region radiating infragravity wave to the open sea and the reflected free infragravity waves could reach the adjacent coastlines such as Netherlands and UK. Behind the peak of an extreme storm event, the excitation of free infragravity energy is observed along the south of the UK coast originating from Denmark. The north of Holland coasts also radiate large amounts of free infragravity energy but is unable to have a prominent impact in the centre of the North Sea due to energy dissipation.

These results imply that the radiated infragravity waves can be influential in distant coastlines in the North Sea during storm events and the changes of local coastal dynamics can be attributed to a different generation region due to the storm characteristics.

Preface

The finalizing of this master report marks the end of my work as a student at the Delft University of Technology. Through the process, I faced many challenges and also learned a lot. I am grateful for the support from all the committee. Thank you for all the input and guidance that help me adapt to a new environment of doing research, for enlightening me with good ideas, and for your expertise in the field that leads me in the right direction.

I would like to express my deepest gratitude to all of you. My committee chair, Prof. Reniers, thank you for giving me constructive feedback in every important meeting and the guidance at the beginning of the project to let me get the hang of it. Dirk, I feel a great honor to have you as my daily supervisor. I can always reach you whenever I need help. Thank you for your time and guidance in all kinds of work, no matter big or trivial until the end of my thesis. Matthieu, Marion, and Marcel, thank you for the comments during the meeting and for reviewing my report in detail which help me to correct my work and improve the final report a lot.

I would like to thank my family, especially my father, for supporting me to study in the Netherlands and for all the caring and encouragement during these two years that helps me go through the pandemic time. Thanks also to my friends Monica and Marisol, I had a great time with you during my study career in Delft. The moment when we shared our struggling and happiness are kept deep in my mind. I owe special thanks to Mengdi, who support and accompany me during my thesis, for always being there for me.

Hamburg
October 5, 2021

Chen Fa

Table of Contents

List of Figures

List of Tables

Chapter 1

Introduction

Nearshore waves prominently affect the coastal communities including harbor and residential environment. Wave conditions and current circulation induce the dynamic changes of morphology at the shore [43]. Infragravity wave height nearshore is an important indication of coastal safety, the presence of nearshore infragravity waves can cause dune erosion during storm events [56], potential overtopping, overwash [42] and harbor resonance [47]), thus can be a significant parameter for design criteria in coastal engineering field [44]. Research embracing the distribution and propagation pattern of infragravity waves not only helps us deepen the comprehension of the low-frequency waves but also shows practical meaning in the understanding of wave forces to the environment.

Infragravity (IG) waves are surface gravity waves with frequencies between $0.005 - 0.05Hz$ lower than the wind waves. IG waves are generated mostly along shorelines by nonlinear interactions of the sea-swell waves (frequencies $0.05 - 0.4Hz$) [38] [27]. The energy transfer is prominent in shallow water and force the bound IG wave which is marginal in deep water. Other generation mechanisms such as time-varying breakpoint in the surf zone also contribute to the energy transfer to IG bands [63]. With the steepening and breaking of sea-swell waves, the bound components are transformed into free IG waves that get released from sea-swell wave groups. The energetic IG waves can prevail over sea-swell (SS) waves on mild slope, affecting the nearshore wave characteristics. Under extreme conditions, the wave motion of IG waves can dominate over the SS waves and play an important role in the shape changes of the beach [55], [12]. As a result of the increase of non-linear wave interactions between SS waves and IG waves, the considerable IG wave height compared to the water depth can adversely affect coastal safety.

Recent research focusing on the IG waves at intermediate water depth has shown a significant difference between total IG energy levels and local bound IG energy according to the IG wave observations on the North Sea [51] [53]. This could be explained by the radiated free IG wave energy that origins from the nearshore region along the coast, revealing a large propagation distance of free IG waves [52]. In some cases, the IG wave source from one shoreline can travel to other distant coasts [53], which leads to the interest of researchers in the propagation pattern of free IG waves at oceanic scales.

Novel observations of infragravity waves with periods between 50 and 200 seconds have been collected by Rijkswaterstaat at some locations on the North Sea. This provides a unique picture of the presence of the infragravity waves. A reliable method to simulate the propagation of IG waves will be presented in this report and gives a clear view of the distribution of IG waves on the North Sea. It also allows us to gain insight into the primary generation, propagation and dissipation mechanisms of IG waves in regional sea under severe weather events.

1-1 Research Objective and Questions

This research focuses on the IG wave pattern observed on the North Sea and the related driving mechanisms. To that end, we use a wave model to reproduce the generation and evolution of free IG waves in the North Sea and analyze the measurement records to show the impacts of storm conditions and bottom friction on distribution and origins of IG waves. Based on the up-to-date knowledge of research on free IG waves, the main research objective is to:

Investigate the main mechanism that impact the generation, propagation and dissipation of free IG waves on the North Sea and evaluate the model skill to provide an adequate explanation of their origins and distributions.

For further clarification, The main objective has been split into the following research questions:

- What's the proportion of free IG and bound IG waves in the total IG wave signal observed in the North Sea?
- How do extreme weather conditions and bottom friction affect the generation and propagation of free IG waves in the North Sea?
- What assumptions should be applied to simplify the complicated evolution process of free IG waves?
- How can we verify the validity of the model?
- Can we determine the source of free IG waves incident to the Dutch coast?
- How much of measured energy does radiation IG from distant shorelines explain?
- When and where is the model not possible to explain the measured IG energy levels?
- Which shorelines are major contributors of free IG energy in the North Sea?

1-2 Approach and methodology

In this report, we study the temporal and spatial IG energy variations and introduce the contribution and origins of IG waves observed during storm events in the North Sea. The spectral wave model SWAN is used to better understand the IG wave conditions. Empirical

free IG waves are applied as source terms along the coastlines based on the wave action balance between sea-swell wave and IG wave. To calibrate the model and assess the reliability of this method in the estimation of IG waves, different simulations are run to inspect the impacts of bottom friction and emissivity of source IG term on evolution features using 10 severe storm events. Comparisons between the measuring and predicted IG parameters show to what extent the radiated IG wave can explain the bursts of IG wave energy in the open sea. The validated model results are analyzed further to examine the contributions of different coasts, dominant sources and origins of the IG wave energy.

This thesis includes 6 chapters. Chapter 1 shows the background information of the project and gives the motivation of the study on the infragravity waves which gives rise to the objectives, questions, and corresponding approaches of this research with a thesis outline. Chapter 2 introduces the defination of the infragravity waves, the physical mechanisms related to the process of generation, propagation and dissipation in both nearshore region and regional sea with a look into global ocean based on the up-to-date related works. Chapter 3 presents the function of SWAN with an extensive implementation to infragravity waves and describes the methodology used to simulate the free IG waves including the model set-up and parameterization of source IG terms. Chapter 4 discusses the process to calibrate the model using two storms via varying the value of empirical calibration parameter and friction coefficient to discover the optimum configuration for the SWAN model. Chapter 5 shows the validation results of the model during three storm events representing extreme, moderate and mild weather conditions respectively. The optimum combination of the empirical parameters is used to investigate the origins of free IG wave energy at different stations. Chapter 6 analyses the limitation and uncertainties of the research and reflects on the possible causes for differences between the predicted and observed results, summarizes the conclusions of this project and gives recommendations for future work.

Chapter 2

Literature Review

The wave interaction in sea-swell bands generates gravity waves with a range of periods approximately between 25s to 200s are denoted as infragravity waves. When the incident sea-swell wave groups approach the beach, they experience shoaling and the shape grows steeper gradually and ultimately breaking. The bound IG waves forced by sea-swell wave groups are released as free IG waves. Under different beach environments, the dominant wave changes with variation of energy level. On a mild slope, IG waves dominate over sea-swell waves along the shoreline, imposing a larger impact on the run-up, overtopping and possible dune erosion [19]. On a steep bottom slope, the IG waves have a chance to travel out of the surf zone while a proportion of outgoing IG waves are trapped forming edge waves alongshore. When traveling across irregular rocky coastlines under a variable bathymetry, a standing IG wave might occur [75]. In this section, the previous research on the generation, propagation and dissipation mechanisms of IG waves will be summarized.

2-1 Generation mechanisms

The primary generation mechanisms of IG waves is known from shoaling and breaking of nearshore wind waves and they can contribute to the IG energy level in deep water after reflection along coastlines [31] [63]. Other mechanisms are also found related to the bursts of IG waves such as generation by atmospheric convection cells and by wind gusts in deep water.

2-1-1 Air pressure at a large scale

When cold air moves over a relatively warm sea surface behind a cold front, the heat from seawater conduct to the upward air mass rising to a higher layer. The movement of the air mass forces the convection cells which transfer heat circularly. With the advance of the entire system, the speed of these cells varies and create the pressure variations locally. The fluctuations of the wind speed caused by convection cells above the seawater generate

low-frequency sea waves, The amplitude of the waves can be prominent observed at sea, on condition that the wind speed of the convection cells system is close to the speed of these long waves. This generation mechanism mostly takes place in the shallow region for instance in the southern North Sea. For bottom topography under deep water or in a steep slope, the resonance phenomena hardly occur by varying wind speed resulted from convection cells due to the differences in propagation speed [15].

2-1-2 Wind gusts

Apart from the nearshore generation mechanism, evidence shows that IG waves can also be generated in deep water. Wind gusts can arise the interactions between wind speed variations and surface wave through Bragg resonance. Bragg resonance originally refers to the wave triads energy transfer via nonlinear resonance between waves with the same frequencies in a homogeneous fluid. For the cases considered here, the variation of wind speed incurs the oscillation of surface waves. The wave length of wind gust oscillations can meet the Bragg resonance conditions with a magnitude of 1 km. The gust effects results in an uneven growth of wave field. If the bottom topography is periodically modulated, the Bragg resonance can be closed [71] [17]. This is similar to the wave motion over changing topography such as bottom ripples.

2-1-3 Nearshore generation from wave groups

Wave interaction between different short wave frequencies can generate the IG waves through different mechanisms. When short wave groups propagate in constant depth, the gradients in radiation stress first cause bound IG waves [38]. The forced 2nd order bound waves are locked in the group with a phase shift of 180°. While in varying depth towards shallow water, the phase shift between IG wave band and short wave band changes along with the amplitude. In the extreme situation with water depth close to zero, increasing long waves lags 90°compared to the wave group. In addition, the energy transformation between bound IG wave and free IG wave would also affect the IG generation in surf zone.

Long wave generation by a time-varying breakpoint in surf zone

The breakpoint forcing generation mechanism has a large relation to the increase of outgoing free IG wave energy. The amplitude of outgoing free IG wave relies on the breakpoint position, group frequency and beach slope [63]. A range of incident wave harmonics added up to a wave group with different amplitudes experience wave breaking in varying break positions restricted in the forcing region. At the breakpoint region (or forcing region), with the advancing breaking of the short wave under a varying bathymetry, long waves are released propagating both onshore and offshore away from the forcing region. The long wave propagating seaward also contributes to the total free IG wave. The long-wave towards the shoreline is reflected, forming a standing wave just shoreward of the forcing region. The existence of outgoing long waves as a product of the varying breakpoint is also found to suppress the response of standing waves. Outside the forcing region, wave interaction between reflected outgoing wave and wave directly generated from breakpoint region start to play a role due to the phase relationship in terms of amplitude.

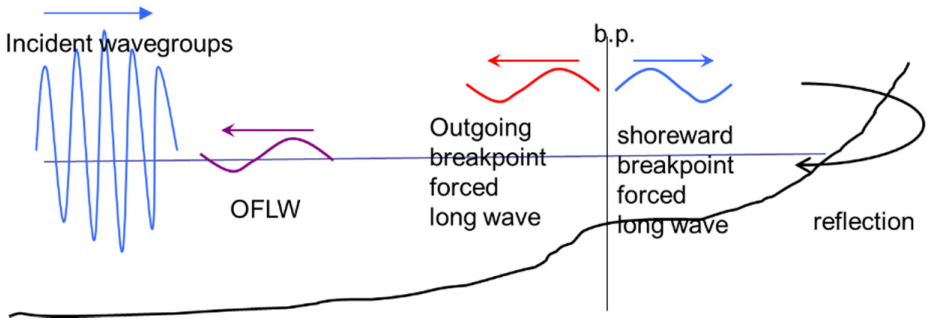

Figure 2-1: Theoretical sketch of incident wave groups on a coast and the outgoing free long wave (OFLW) reflecting off the breakpoint (b.p.). The breakpoint forcing mechanism produces an outgoing breakpoint forced long wave seaward and a shoreward breakpoint forced long wave onshore. The shoreward long wave will be reflected and can propagate towards the sea [67], from https://www.mdpi.com/2077-1312/4/1/12.

Free IG wave released from bound IG wave

Wave groups are associated with a second-order current which is called bound IG wave observed in the deep ocean. The height of the bound IG wave is connected to the radiation stress of wave groups in the equation [38],

$$\eta(x,t) = -\frac{S_{xx}}{\rho(gh - c_g^2)} + const. \tag{2-1}$$

η represents the amplitude of bound IG wave responding to the horizontal change of radiation stress S_{xx} of short waves. The gradient of radiation stress imposes the variation of surface elevation in anti-phase with wave groups which is locked in. In conclusion, the nonlinear interaction between short waves with different wavelength forces the undulation of mean sea level which has the same length as the wave envelope. This second-order current is so-called bound IG wave [38][5].

With decreasing depth, the denominator is close to zero. The response of the surface to the stress will increase. The phase between short wave groups and bound IG wave does not keep constant anymore and shifts from 180°resulting in the time lag. This gives a chance for the energy transfer between short wave and bound IG wave, especially under a mild slope [41] [35]. Under a steep slope, the growth of IG waves due to this mechanism is weak while the breakpoint mechanism dominates instead [5]. As the depth decrease further, short waves will break first and release IG wave propagating as free IG waves [41] [35] [3].

Free IG wave generation due to depth variations without short wave breaking

As short waves and bound IG wave experience shoaling when encountering depth changes, the phase shifts induce the generation of free IG wave. Similar to the case in the breakpoint mechanism, the generated free IG would propagate both seaward and shoreward but the outgoing free long waves in this mechanism are quite small thus can be negligible. Assume a decreasing water depth without breaking waves, a group of short waves along with bound IG waves propagate towards the slope. With the decrease of depth, free long wave successively

emerges overtime under continuous forcing. The previously generated free IG wave travels faster than the newly generated one and has a larger peak, the combined free IG waves show an extended tail in front of the wave group toward the shore. This mechanism is usually found in mild slopes [11] [37].

Bore merging

In the surf zone, incident waves break and propagate towards the shoreline in the form of bores. When a faster bore catches up with the bore in front which has a lower speed, the bores merge as a new wavefront. The process occurs in mild slope as such the larger bores get enough time to overtake smaller one [33]. In addition, it has been proved to cause the increase of the wave period which has an impact on low-frequency waves [60]. While IG waves already generated outside of the inner surf zone can disturb the bore merging process which makes it difficult to filter out (separate) the part due to the bore merging. It should be noted that the bore merging mechanism has little contribution to the generation of IG waves in the surf zone compared to breakpoint moving and bound IG wave transformation mechanisms [66].

2-2 Propagation and dissipation

Similar to the short waves nearshore, the low-frequency IG wave will experience the same mechanisms: shoaling, refraction and reflection. The temporal and spectral spectrum variations varies with different frequency bands. Some mechanisms have a large impact on the energy dissipation such as bottom friction, wave breaking in surf zone and energy transfer between high and low frequencies. It is noted that energy transfer accounts for both increase and loss of IG wave energy [30]. The corresponding mechanisms is introduced in section 2-2-1.

As a source of IG waves in the open sea, the radiated free IG waves contribute to the energy transfer in far fields. The observed free IG waves accounts for the missing energy part in IG bands combined with forced bound components. This has been attributed to the generation of free IG waves along distant coastlines. A model that reproduce the propagation of free IG waves and the related observation in regional sea is elaborated in section 2-2-2.

2-2-1 Nearshore region

Radiation stress gradients forcing energy variations of long waves in surf zone

When short wave groups travel towards the shore, the radiation stress gradient varies with varying bathymetry, which forces the sea-level changes and induces energy transfer between sea swell waves and IG waves. After entering the surf zone, the energy flux of incident waves increases and reaches its peak before the breakpoint. In the middle of the surf zone, it decreases inducing an energy dissipation of IG wave accompanied by energetic wave motions with strong negative radiation stress gradients. With a mild bed slope, smaller sea swell waves near the shoreline can also transfer energy to IG waves. The dissipation of IG waves is also affected by bottom friction and wave breaking in the nearshore region. On the other

hand, researches had found that the effect of bottom friction can be excluded due to a small energy loss rate [30]. In the inner surf zone, the energy transfer also occurs between different IG components resulting in the steepening of long-wave front and even long wave breaking in shallow waters. This type of interaction causes energy accumulation in higher frequencies. Some evidence even shows an increase of short waves from IG bands. Under mild changing of slope close to the shoreline, the dissipation of the long waves can be prominent over the bottom friction dissipation [68]. The long wave breaking and negative work done by radiation stress appears to be the main reasons accounting for the IG energy loss inside the surf zone. The depth-limit breaking criterion hardly happens to IG waves [57] when the relative height of IG wave compared to the water depth δ is lower than the classical value 0.8 for short-wave breaking, which is defined as,

$$\delta = \frac{H^+}{h + \overline{\eta_c}}, \tag{2-2}$$

where H^+ is the low-frequency incident root mean square wave height, h is the still water depth, and η_c is the average of low-frequency free surface displacement.

Long wave reflection and edge waves

With the propagation of long waves closer to the shoreline, the shoaling rate (amplitude growth rate) and long wave breaking regime depends a lot on the bed slope. A dimensionless parameter β is used to quantify the slope [68],

$$\beta = \frac{\beta T}{2\pi}\sqrt{\frac{g}{H^+}}, \tag{2-3}$$

where β is the normalized bed slope parameter, H^+ is the incoming IG wave height and T is the IG wave period, g is the gravitational acceleration.

Under a mildly changing bathymetry namely a small $\beta < 0.3$, long wave breaking plays a role in the dissipation of IG wave energy in the swash zone, which dominates over the bottom friction mechanism [65] [30]. In relatively shallow water, the triad interactions between short waves and long waves decrease and self-self interactions inside the low-frequency band take place. On a steep slope regime ($\beta > 1.25$), the IG wave barely dissipates energy and the reflection efficiency is around 1 [14].

Reflection A reflection coefficient representing the ratio between the reflected and incident IG wave height with a correlation of the normalized bed slope parameter is defined as:

$$R = 2\pi\beta_H^2 \tag{2-4}$$

in which β_H is the normalized bed slope.

A strong dependency of reflection rate on frequencies has been observed both in numerical models [54] and wave experiments [68]. With a frequency smaller than 0.03Hz, a standing wave can be observed while for high frequencies, partial standing or progressive waves occur

in cross-shore transect [26] [14]. The correlation between reflection and bed slope using normalized bed slope parameter β_H are also inspected [3]. Higher reflection corresponds to a larger β_H value ($\beta_H > 1$) and lower reflection corresponds to a smaller value ($\beta_H < 1$). According to the field experiments and Delft-3D-surf beat model applied, the study found a transitional $\beta_H = 1.25$, above which the steep slope regime dominate with a high reflection rate and below which the mild slope regime take place with a lower R value [68] at the shoreline. The transitional number found by van Dongeren et al. (2007) depends on the local conditions referring to a specific cross-shore location [68]. Thus for other field experiments conducted later [14], a different transitional β_h is given on different beaches.

Edge waves and free waves The obliquely incident IG waves are reflected from shorelines experiencing reverse refraction. Part of IG waves can be trapped in the surf zone, also referred to as edge waves [22]. Edge waves are progressive along the shoreline and are trapped in the coastal region. IG edge waves have been widely observed in surf and swash zone especially on mild slope beds [48]. The longshore periodic features of standing edge waves may have an impact on the formation of beach cusps, crescentic bars, and rip current [9].

Those travelling across the surf zone and propagating freely towards the sea in cross-section direction are called leaky waves. Both leaky and trapped waves are free IG waves. The outgoing free IG wave is our focus in the study since they are capable of traveling over a long distance in the open sea. The different generation mechanisms of free IG waves have been introduced in the previous section. The dominant mechanisms accounting for the free IG generation depend on the beach environment. Compared to the edge waves, the free IG wave radiated from the shoreline can travel across regional or oceanic scales from one coast to another [1] [49].

The periods of edge waves are observed related to the beach steepness. On a steep slope, reflected edge waves tend to form 2 types: synchronous and subharmonics with whose periods are double times than the representative period of incident IG waves [5]. On a relatively mild slope, wave breaking dominates, and after breaking the resonance that forms the two types of edge waves under a steep slope does not occur anymore. Instead, edge waves of longer periods take place. It is also noted that the directional distribution of the outgoing IG waves is wider than the incoming IG waves that tends to be narrower especially on mild slope [31]. Under energetic wave motions, the generation of edge waves is limited in the presence of substantial wave breaking on a bar-trapped beach [54].

2-2-2 Open sea

Arduin et al. (2014) represents the free IG waves including both leaky waves and trapped waves in the spectral wave model WAVEWATCH 3 and gives a picture of the contribution of free IG waves at coastal regions and global scales. They defined an empirical source of IG energy along shorelines from spectra parameters of sea swell waves using a proportionality factor α_1. The impacts of the dissipation parameterization on the predicted IG wave heights are different on account of shelf configurations. Therefore, two regions with a narrow shelf and a wide shelf are investigated to calibrate the model. For the implementation in a narrow shelf on Oahu's north shore (Hawaii), the wave energy levels (including both sea swell and IG wavebands) observed in a close location to the source coastline are in good agreement with

the modeled result with an accuracy of around 93%. In the wide North Carolina shelf, the effect of bottom friction is explored through different model runs applying bottom friction to IG bands and/or SS bands. It is known that the free IG energy decreases faster traveling towards the deep water along with swells, suggesting a strong attenuation in free IG bands during heavy swells [18]. Bottom friction is a primary factor that attenuates the energy of sea swell waves but it is barely explored in IG frequency bands. The modeled results give a good explanation of observations with varying α_1 values applied for cases with and without bottom friction. A slightly larger α_1 should be implemented when including bottom friction in the model to compensate for the dissipated energy of free IG waves on the inner shelf or the part of trapped IG energy nearshore. However, the constant bottom friction parameters make little sense to treat the dissipation variations between the IG band and SS bands over time and space. Further investigations are required to describe the interactions of SS waves and IG waves in the model. With convincing model results in coastal regions, they also looked into the IG wavefield at global scales. The wide shelves of exposed coasts, including north-west Europe and the southern Australian bight are observed to have the most energetic energy bursts in IG bands. The pattern of IG wave distribution in the global map varies seasonally and has a large correlation with heavy storms. As a result of the restriction of measured data, the IG wave evolution at each region requires further exploration [1].

The approach of prediction of the incident offshore IG conditions in the North Sea is studied by Reniers et al. (2021) using the observed local frequency-directional spectrum in intermediate water depths (O(30) m), based on which the incident IG waves in deep water can be properly represented for the application of the future model. To that end, they analyze the observation records with the sea-swell and long wave data from 2010 to 2018 in a number of stations located in the North Sea. IG wave climate is examined to inspect the contribution of bound IG wave and free IG wave to the total IG variance dependent on the sea-swell waves. The IG response is found strongly related to the local sea-swell conditions at different observation locations and timing during the storm. A high bound IG contribution to total IG bands occurs at peak of the storm and conversely at the onset and waning of the storm. The ratio between bound and observed total IG variance shows spatial variability along the south boundary of the North Sea (Dutch coast) due to the relative direction between the coastline and the incoming waves. This suggests that differences in beach characteristics where the free IG wave originates from play an important role. A further look into the IG response for different storms and beaches (variation in beach slope and coast configuration) is expected to specify the incident free IG component using spatially dependent constant α_1 introduced in the approach of Ardhuin et al. (2014) [51].

In the same region, Rijnsdorp et al. (2021) explore the source and origin of the significant free IG wave energy for four severe storm events in the observation record. The spectral wave model SWAN is extended with the empirical source free IG term along the shorelines as boundary condition following the approach of Ardhuin et al. [1]. The empirical spectral shape of the source IG wave is defined as isotropic in direction and is imposed at intermediate water depths (approximately 15m) along the major coastlines that face the southern North Sea. The radiation of free IG waves acts as the only source in the model combined with bottom friction using the JONSWAP formulation of Hasselmann et al. (1973) as the sink. With a proper combination of empirical parameter α_1 and friction coefficient parameter χ, the model is able to explain up to 75% of the observed free IG wave energy. This indicates a major contribution of radiated IG waves from distant coastlines, in accordance with a previous

study on the shelf [62] and in the deep ocean [49]. In addition, it proves that the incident free IG waves originated from distant shorelines could impact the local coastal environment. Furthermore, the bottom friction can attenuate the energy of free IG waves on the relatively shallow North Sea basin and lead to a better model-data match when the majority of free IG energy comes from distant coastlines. Based on the difference between the four storms, the generation and origin of free IG waves also show large variability. Where the large sea-swell waves made landfall becomes an influential factor [53].

2-2-3 Impacts

The excitation of IG waves in coastal zones has a range of implications in hydro-sedimentary dynamics, for instance, the formation of rip channels due to rip current and sediment transport in cross-shore direction on sandy beaches. The IG waves are also capable of promoting run-up and overwash, eventually cause dune erosion and impact coastal safety. In the tidal inlet, IG waves can lead to large modulations of currents and sediment transport. The impacts on ice sheets as a result of energetic IG wave oscillations are also introduced here.

Rip current Rip currents are strong, narrow currents that originate from the shoreline and flow seaward as a fast-running river [7]. Rip currents are ranked as one of the severe threats to public safety in the coastal region, which can bring swimmers or materials far from the shoreline into deep water. Thus the surf zone circulation of a rip current is important for the exchange between the surf zone and edge of the surf zone to the open sea.

The main forcing mechanism arising from the generation of a rip current is the alongshore variation in wave forcing within the surf zone. The slow alongshore modulation of the water surface could force the rip currents which can pulsate on timescales of 20 seconds to 10 minutes.

Although the appearance of IG waves has no direct relevance to the formation of rip current, to some extent the resonance pattern between short wave groups and synchronous standing IG edge waves can explain the pattern of rip currents [64]. In terms of different rip types caused by either morphological or hydrodynamic or combined reasons, there can be a large difference between the instantaneous flow and the mean flow of rip current. The temporal and spatial variability in wave forcing causing VLF's and flash rips is present in any nearshore circulation. The dynamics of rip currents show more kinematics on shorter timescales: IG wave timescale (25s - 250s) and very low-frequency timescale (250s - 30min). It is noted IG wave motions have a temporal effect on the behavior of rip currents [59] though VLF pulsations are proved to be a dominant mechanism for the exchange, bringing occasionally material beyond the surf zone edge [39] [2].

Run-up and overwash On a mild sloping beach, the spectra of run-up or swash oscillations at wind frequencies show a large dependence on the wave periods. Run-up energy at IG periods grows with increasing incident short wave energy, which indicates saturation in the surf zone [25].

Over the reef face and flats, a large amount of incident wave energy is dissipated and the major frequency bands left are in the range of IG waves. After crossing the reef crest, IG

Figure 2-2: Rip current formed between sandbars, https://www.britannica.com/science/rip-current

wave increases along with the wave run-up through resonance as a result of the wavelength of IG wave approximately four times longer than the flat width [46]. Based on the wave model using Boussinesq-type equations, Shimozono et al. (2015) examined the coupling influence of wave interactions between SS wave and IG wave over fringing reefs during super typhoon validated by field survey. It shows a narrow reef could induce extreme run-up through the strong coupling of IG wan SS waves, while on a wider reef flat, the dominance of IG wave brings the existence of bores on steep beaches [61]. On reflective beaches or gravel beaches when the IG wave is not the dominant one in the swash zone, the saturation of the incident waves contributes to the swash oscillations through the interaction between uprush and back rush [40].

Overwash refers to the flush to the landward of a dune system may during storm events which cause rapid profile changes and possible dune destruction, thus increasing the flood risk of hinterland even the coastal infrastructure [20].

The study of Baumann et al. (2017) investigates the factors controlling the sediment deposition caused by washover along a dissipative beach. It is been identified that the IG wave governs the overwash flows in field experiment records. The exceptional wave motions with a significant wave height exceeding 1.5m driven by IG wave band arise large run-up, showing a strong correlation between IG wave and wave-induced run-ups on dissipative beaches [4]. In the case of steep, reflective, gravel barrier, IG wave motions have an impact on increasing wave run-up and lowering overwash thresholds, and increasing the magnitude of the overwash discharge [45] [56].

Sediment transport The contribution of the IG wave to the sediment dynamics and as a result the morphological changes of sandy coasts have been investigated due to the significant influence of IG bands compared to the incident SS bands [8] [76]. In the nearshore region, the local features in terms of beach profiles and wave conditions have a large impact on driving mechanisms and the direction of sediment transport. Based on field measurement on a

Figure 2-3: Overwash on Onslow Beach, North Carolina, USA, March 2013, screenshot from Google Earth.

relatively gentle beach (Sand Motor Beach with a slope around 1 : 35), De Bakker et al. (2016) found that local ratio of infragravity wave height to sea-swell wave height (H_{IG}/H_{SS}) is a good indicator to measure the relative importance of IG wave for sand suspension mechanisms. When H_{IG}/H_{SS} is lower than 0.4 on a relatively steep beach, incident short waves dominate over the IG waves and stir the sediment into a suspension state. They use another parameter r_0 to estimate the correlation of the IG wave orbital motion with the SS wave envelope and study the direction of IG-related sand fluxes. In the surf zone, negative r_0 meaning the presence of largest SS waves combined with offshore IG velocities leads to sand flux offshore. Closer to the shoreline when $r_0 > 0$, the largest SS waves with shoreward IG velocities result in onshore IG-induced flux. Whereas in the case $H_{IG}/H_{SS} > 0.4$, the dominance of IG wave brings substantial offshore-directed sand transport [13].

Dune erosion Dune erosion can cause a large change of coastal morphology and threaten the safety of low-lying hinterland from flooding due to the response to storm impacts. Nearshore wave motions raising the sand loss and retreat of the dune front are the main agents accounting for the morphodynamic of the beach. The energetic IG wave dominates in the inner surf zone and swash zone under severe storms. The impacts of IG waves on dune erosion are thought to be significant when approaching close to the beach. It is pointed out that the oscillations of IG waves reach the shoreface and can produce slumping of the wetted part of the dune face, leading to the avalanching of the dry part of the dune subsequently. Due to the difficulty of separating the role of IG waves and short waves, it is hard to verify the effect of IG waves only based on observational data [56].

A study investigates the effect of IG waves on dune erosion using numerical modeling and proves that IG waves may enhance the dune erosion on a dissipative sandy beach by approximately 20-30% under extreme storm events [69] [70].

The collision regimes of dune erosion are dependent on the storm characteristics (surge height, duration, and spatial variation along the shoreline) and beach profile (crest height, sediment

properties, vegetation, and longshore variation in topography and bathymetry). For a wide range of storm conditions, IG waves can exercise an influence over different regimes and cause a strong morphodynamic response on dissipative sandy beaches [5].

Tidal inlet Tidal inlet, a significant connection between ocean and inland, is featured with diverse morphology, hydraulic signature, and sediment transport patterns [29]. The hydro-sedimentary dynamics of tidal inlets is acknowledged as being related to the short waves over the last decade through field measurements [72]. Also, the presence of wave fluctuations in IG bands in tidal inlets is identified [6] [74].

Bertin et al. (2016) revealed the occurrence of low-frequency oscillations in water levels and current velocities. While the wave motions in IG bands only appear in ebb-tidal deltas and in a specific period from the beginning of the flood to a few hours after the high tide during a complete tide cycle. The reason for this phenomenon is caused by the blocking from the counter currents. Numerical modeling reproducing the generation and propagation processes of IG waves shows that breakpoint mechanism and bound IG wave shoaling mechanisms are the major contributors in the tidal inlet [6].

Ice sheet The seismic observation from a field measurement on the Ross Ice Shelf during 2004-2006 shows that the flexure and fracture of the ice shelf are related to the ocean swell (<30s) originating primarily under far-field Pacific storms and also IG waves with periods from about 250 to 50 s [10]. The free IG waves are found to propagate transoceanically from the generation region along the Pacific coast of North America to Antarctica causing a higher impact to the response of ice shelf compared to sea swell waves. The IG waves are originated from the remote continental shelves experience shoaling and the amplitude increase at the ice front when propagating into shallow water. The higher amplitude of IG waves than sea swell waves thus has a larger influence on the ice shelf integrity. Leading theories shows that the IG wave oscillations can expand the pre-existing crevasses and enable the collapse of ice shelves [58]. The mechanism that produces the initial crevasses remains unknown. It is assumed that IG waves could act as the primary trigger and initiate the collapse process [10].

Chapter 3

Methodology

This chapter elaborates on the methodology used for the prediction of IG wave variation and comparison between model results and measurements. Two mechanisms, radiation of free IG waves along shorelines and bottom dissipation, are considered in the simplified modeling process of IG wave evolution which is explained in the source and sink term in the governing formulations of SWAN. Boundary condition of incident free IG waves along the shorelines is implemented based on the wave interactions of sea-swell bands empirically. Finally, following an introduction of 10 storm events and observation data, the method to quantify the model-data agreement is given.

3-1 Introduction of SWAN model

Governing equations The spectral wave model SWAN (Simulating WAves Nearshore) is used as a tool for the random, short-crested, and wind-generated waves, estimating the wave characteristics from given wind and topography environment based on the wave action balance equation,

$$\frac{\partial N}{\partial t} + \nabla_{\vec{x}} \cdot [(\vec{c}_g + \vec{U})N] + \frac{\partial c_\sigma N}{\partial \sigma} + \frac{\partial c_\theta N}{\partial \theta} = \frac{S_{tot}}{\sigma}. \tag{3-1}$$

In this equation, the first term represents the temporal evolution of the wave action density N; the second term represents the propagation of wave energy in 2D geographical space, in which group velocity $\vec{c}_g = \frac{\partial \sigma}{\partial \vec{k}}$ following from the dispersion relation $\sigma^2 = g|\vec{k}| \tanh |\vec{k}|d$, and ambient current velocity $\vec{U}$ is assumed uniform in vertical direction; the third term represents the effect of shifting of the radian frequency due to variations in mean currents; the fourth term represents depth-induced and current-induced refraction; the fifth term represents the spectral changes of all sources and sinks.

In the first term, the wave energy variation are indicated by action density N instead of energy density E. The energy density $E(\sigma, \theta)$ distributes wave energy over radian frequencies σ and propagation direction θ. The evolution of energy density over time and space gives

$N(\vec{x}, t; \sigma, \theta)$. The action density defined as $N = E/\sigma$ is conservative during propagation in the presence of ambient current, whereas energy density E is not [73].

Several physical processes can be included by means of the source terms in the right-hand side of equation (3-1),

$$S_{tot} = S_{in} + S_{nl3} + S_{nl4} + S_{ds,w} + S_{ds,b} + S_{ds,br}. \tag{3-2}$$

From left to right, the term denotes wave growth by the wind S_{in}, nonlinear transfer of wave energy (triads S_{nl3} and quadruplets S_{nl4}), wave decay due to white capping $S_{ds,w}$, bottom friction $S_{ds,b}$ and depth-induced wave breaking respectively $S_{ds,br}$.

Dissipation by bottom friction The bottom friction has a larger impact on the coastal waters compared to the oceanic waters due to shallower water. Nevertheless, the North Sea is featured by mild beaches and relatively shallow water depth. The propagation of IG wave in the North Sea over long distance is also under a large impact of bottom friction.

Bottom friction is the dominate mechanism for bottom dissipation for continental shelf seas with a sandy seabed [32]. The wave-induced motion of the water particles transfer energy to the turbulent motion in the thin boundary layer at the bottom. The energy dissipation of wave thus depends on the characteristics of the seabed and wave field itself. The dissipative character that determines the magnitude of energy loss is represented by an empirical coefficient.

There are three bottom-friction model options to estimate the bottom friction coefficient in SWAN: the drag law model of Collins (1972), the eddy-viscosity model of Madsen et al. (1988) and the empirical JONSWAP model of Hasselmann et al. (1973).

The corresponding bottom friction source term for these models is expressed as,

$$S_{ds,b} = -C_b \frac{\sigma^2}{g^2 \sinh^2 kd} E(\sigma, \theta), \tag{3-3}$$

in which σ is frequency, C_b is a bottom friction coefficient that generally depends on the bottom orbital motion represented by root-mean-square orbital bottom velocity U_{rms}:

$$U_{rms}^2 = \int_0^{2\pi} \int_0^{\infty} \frac{\sigma^2}{g^2 \sinh^2 kd} E(\sigma, \theta)\, d\sigma d\theta. \tag{3-4}$$

The constant friction coefficient recommended is $C_b = C_{JONSWAP} = 0.038 m^2 s^{-3}$ from the results of JONSWAP experiment. Later the constant friction coefficient is also represented by the symbol χ.

Typical SWAN applications SWAN is used to obtain realistic estimates of wave parameters in coastal areas, lakes and estuaries from given wind, bottom and current conditions. It is fully spectral (in all directions and frequencies) and computes the evolution of wind waves with shallow water and ambient current.

SWAN is stationary and optionally non-stationary and can be applied in Cartesian or curvilinear (recommended only for small scales) or spherical (small scales and large scales) coordinates. SWAN can be used on any scale relevant for wind-generated surface gravity waves. However, SWAN is specifically designed for coastal applications that should actually not require such flexibility in scale.

In this report, we had some insight into the evolution of IG waves over the entire storm period in the North Sea. Simulations under non-stationary mode in spherical coordinates will be run to observe the variation of 2-dimensional IG wave spectra and investigate the agreement with observations.

3-2 Parameterization of infragravity waves

The aim of this study is to use SWAN to model the propagation of free IG waves in the North Sea using the wave-action balance equation. The modeling in this thesis is based on the hypothesis that the free IG waves in the North Sea originate from the shorelines where they were generated by the sea-swell waves (Section 2-1). Following the approach from Ardhuin et al. (2014) [1], an isotropic empirical IG source was used to account for the radiation of free IG waves from the coastlines bordering the North Sea. In this study the radiated free IG wave is the only generation source in the model. Other possible IG sources for instance wind gusts and air pressure are not considered here.

The empirical IG source term [1] is based on a correlation between the IG wave energy with the product of sea-swell parameters $H_{m0,SS}T^2_{m0,-2,SS}$,

$$H_{IG} \approx \alpha_1 H_{m0,SS} T^2_{m0,-2,SS} \sqrt{g/D}. \tag{3-5}$$

In the formula, H_{IG} and $H_{m0,SS}$ represent the significant wave height of IG wave and SS wave, α_1 is a dimensional empirical coefficient that varies from one site to another with seconds because it is the rate of transfer of energy per unit time, g represents the gravitational acceleration, and D represents the mean water depth. Bulk sea swell wave height $H_{m0,SS}$ and wave period $T_{m0,-2,SS}$ in equation (3-5) are taken at a location seaward of the surf-zone. Ardhuin et al. (2014) found a better fit using $T_{m0,-2}$ compared to other period measured such as $T_{m0,-1}$ or peak period T_p.

The significant wave height of SS wave used in equation 3-5 is given by,

$$H_{m0,SS} = 4\sqrt{m_0}, \tag{3-6}$$

and the mean period is defined as,

$$T_{m0,-2,SS} = \sqrt{\frac{m_0}{m_{-2}}}, \tag{3-7}$$

in which the 'nth-order moments' of the spectrum is given,

$$m_n = \int_{0.04Hz}^{0.5Hz} E_{SS}(f) f^n \, df, \tag{3-8}$$

where E_{SS} represents the hourly surface elevation variance density of the SS waves obtained by averaging over six 10 min blocks.

Based on the empirical relationship (equation 3-5), free IG wave energy is imposed in the SWAN model. Assuming an isotropic directional distribution and an empirical frequency distribution, Ardhuin et al. (2014) defined the IG source term as,

$$E_{IG}(f,\theta) = 1.2F(f)\frac{(\alpha_1 H_{SS} T_{SS}^2/4)^2}{\Delta f}[min(1, 0.015Hz/f)]^{1.5} \times \frac{1}{2\pi}, \tag{3-9}$$

where two-dimensional variance density spectrum $E_{IG}(f,\theta)$ in terms of frequency f and direction θ is calculated as source term that will be input along the shoreline with a resolution of 0.0025 Hz and 48 degrees of freedom, $F(f)$ describes the shoaling of a broad wave spectrum, the frequency band $\Delta f[s^{-1}]$ ensures the unit consistency in two sides of equation (3-9).

The term $F(f)$ accounts for the conservation of energy with changing water depth. For each frequency,

$$F(f) = \frac{kg^2}{c_g 2\pi f}, \tag{3-10}$$

in which k is wave number and c_g is group velocity.

The frequency distribution of the wave spectrum depends on the term k/c_g. The spectral shape of the IG source is given by a frequency shape that is constantly up to $f = 0.015Hz$ and decreases with $f^{-1.5}$ for higher frequencies. If the frequency band is lower, in particular when $f < 2mHz$, the measured wave field in the open sea is mostly driven by atmospheric pressure instead of free IG wave radiated from shorelines [21] [16], which prescribes a lower frequency limit for the modeling.

An example source IG term is shown in figure 3-1a and 3-1b. The variance density is constant up to 0.015Hz and decreases gradually till 0.05Hz. The actual frequency resolution Δf between the prescribed highest and lowest discrete frequency is not constant as shown in figure (3-1b), the distribution of which is logarithmic in the model.

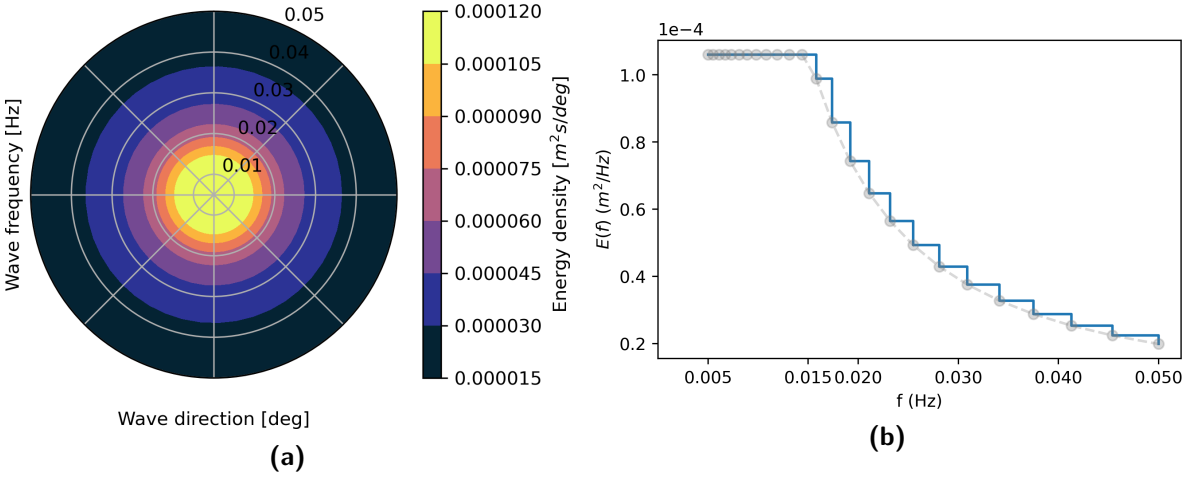

Figure 3-1: IG energy density spectrum and directional distribution of source term

3-2-1 Numerical implementation

To account for the generation of free IG wave energy radiated from shorelines, the source IG terms are implemented through the OBSTACLE functionality. A user can specify a line along which the IG source term has to be imposed. At the computational cells along this line, the IG source term (equation 3-9) is enforced. A user can define multiple lines, and assign a different α_1 for an individual line. This allows users to specify a variable IG source strength for different coastlines.

At each grid point where the IG source term is imposed, the user needs to input sea swell wave parameters. The user can specify a nonstationary spatial field of sea-swell parameters through the INPGRID/READINP functionality in SWAN. In the model computation, the sea-swell values are obtained at the location along the IG source lines to compute the local IG source term. These sea swell wave parameters can be directly defined by users or can be taken from another model's results. In this thesis, the sea swell wave parameters were obtained from the ECMWF-ERA5 reanalysis [53].

ECMWF (European Centre for Medium-Range Weather Forecasts) has a long history with reanalysis in climate monitoring applications since 1980. ERA5 is the fifth generation ECMWF atmospheric reanalysis of the global climate from 1950 onwards. The original datasets from ERA5 at ECMWF provide hourly estimates of a large number of atmospheric, land, and oceanic climate variables. A detailed description of the sea surface dynamics can be available over the global domain, which gives a good opportunity to have insight into the distribution of IG waves in a larger scale.

The wave model that is used for ocean wave forecasting at ECMWF is the WAM model [36]. Similar to the SWAN model, it describes the rate of change of the wave spectrum due to advection, wind input, dissipation due to white capping, and nonlinear wave-wave interactions. The main difference lies in the numerical propagation schemes in the geographical and spectral spaces, which distinguishes them in application scale: WAM is more suitable on oceanic scales whereas SWAN calculates wave propagation from deep water to shallow water.

The global SS waves to be applied in SWAN model are estimated from hindcast via WAM model. SS wave parameters (H_{SS} and T_{SS}) are downloadable from the ECMWF website by selecting the required data types. The source IG terms to be implemented as the input in SWAM is calculated using the parametrization method from Arduin et al. (2014) based on the correlation between SS wave and free IG wave.

In general, α_1 represents the rate of wave energy transformed from incident bulk waves to radiated IG waves directed to the open sea. In reality, the incident sea-swell wave energy varies in time and space which produces a varying radiation IG wave energy using a constant calibration parameter α_1.

With the sea-swell parameters obtained from a suitable source, the main uncertainty of the IG source term lies in α_1 (see equation 3-9). The strength of the IG source is directly related to this calibration parameter α_1. The factors that could influence the energy transfer between SS wave and free IG wave in surf zone in terms of reflection of free IG waves have been described in section 2-2-1. As an experimental parameter, this α_1 is used to correct the source IG term using the global SS wave obtained from hindcast.

Basically, the increase of α_1 value means the more intensive free IG wave energy applied in source term. The larger α_1 is, the stronger wave energy in IG band is released from the

coastlines under the same bulk wave conditions. Since different coastlines bordering the North Sea have a diversity of the geographical environment with respect to shelf width, bottom topography, slope steepness, and local weather impact. For instance, IG wave is largely released on a mild slope in nearshore region whereas a steep slope is unable to produce a large amount of IG waves along coastlines. In addition, the dynamic changes of beach bathymetry due to the wave motions along coastlines in time and space increase the uncertainty of the applied value of α_1. These geographical features and time-varying wave conditions influence the actual wave interaction occurring in surf zone, applying various values to α_1 provides us a chance to understand how the varying of the source free IG wave energy influence the variation of IG wave across the open sea during storm events. Thus a further calibration is required to improve the accuracy of the model using field experiments.

3-2-2 Model set-up

In this study, SWAN operates in a spherical coordinate system with all geographic locations and orientations defined in geographic longitude and latitude. To study the variations of IG wave over a storm, the model is run in nonstationary mode. The physical processes considered here includes shoaling, de-shoaling and refraction of all six processes available in SWAN model (see equation 3-2), indicating the energy transfer between IG wave and the bulk wave due to the bathymetry changes. The wind growth is not considered here because the variation of source free IG wave radiating from shorelines is the only process we focus and we assume local wind variation has minor impacts on the propagation. First simulations without bottom friction will be implemented and then the simulations adding bottom friction process will be inspected to have some ideas about the impact of the bottom friction as well as the combined impacts with the variation of α_1.

Boundary conditions The offshore boundary is set to let free IG waves pass through without obstacles, which is also the case in reality. The nearshore boundary condition is set with various strengths of free IG radiating in all directions.

The IG source line is specified along all coastlines out of surf zone at around 30m bordering the North Sea as implemented in the study from Arduin et al. (2014). Six countries representing six different IG sources are shown in figure 3-3.

As input SS wave parameters H_{SS} and T_{SS} changes over time, the 'relative' strength between the changing SS wave and IG wave is kept constant since $alpha_1$ is constant in time, which means the IG source strength is always equal for the same wave conditions but varies over the storm period.

Model resolution Rijnsdorp et. al. (2021) have gained some first insight into the resolution implemented in the SWAN model regarding the applications in the North Sea. It has been validated that the following spectral resolution required in SWAN simulating the IG wave is feasible [53].

25 discrete frequencies are assigned in IG frequency range from 0.005Hz to 0.05Hz with default logarithmic spacing. The combination of spatial and directional resolution are $\Delta\lambda = 0.025°$for latitude (2.775km), $\Delta\phi = 0.0166°$(1.843km) for longitude and $\Delta\theta = 8°$.

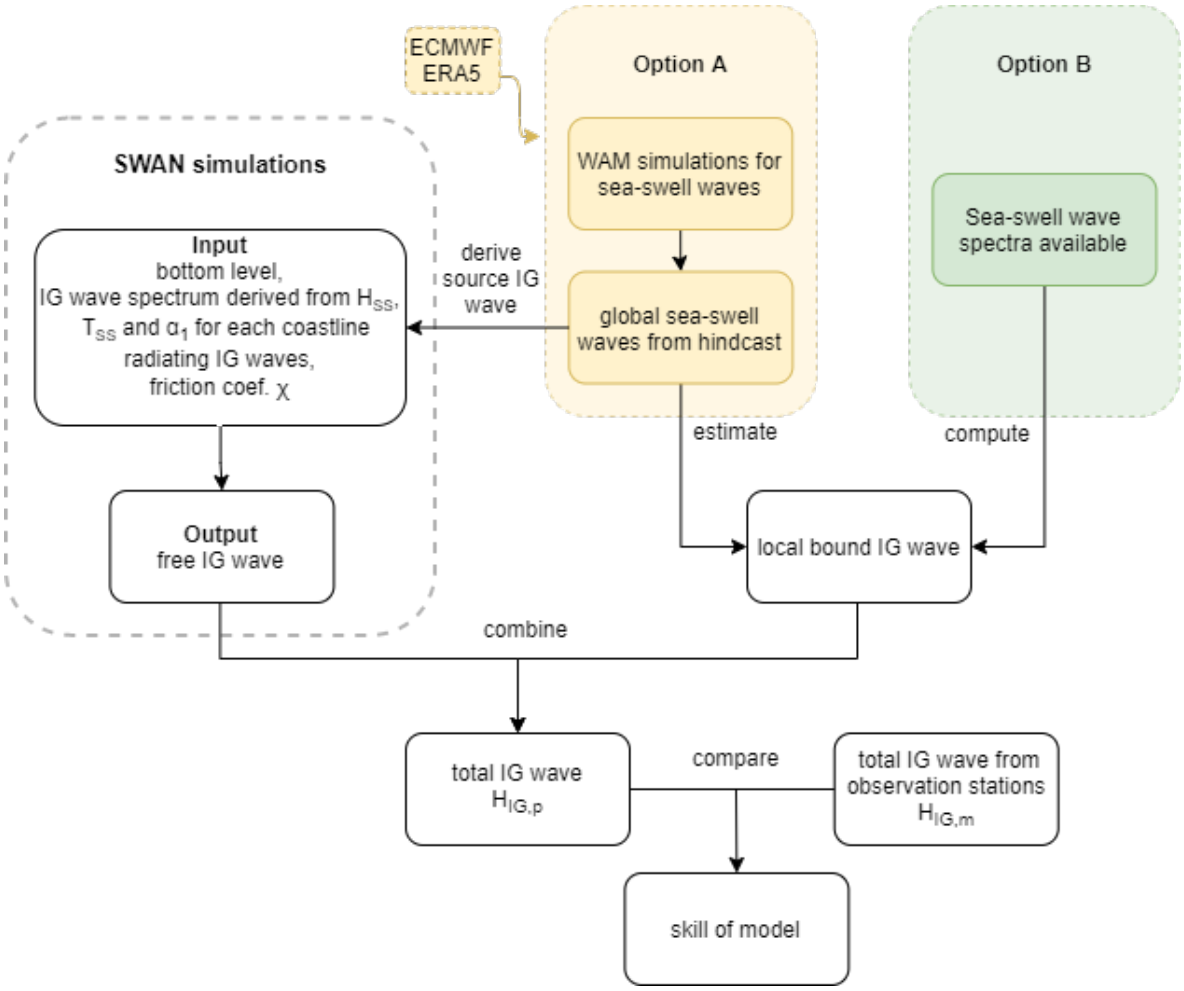

Figure 3-2: Flow diagram showing the derivation of source IG wave and bound IG wave

Source terms Adding bottom friction in simulations induces a new friction coefficient χ $[m^2/s^3]$. In this study, the JONSWAP bottom friction formulation is used. The bottom friction coefficient χ was obtained through calibration. An default value $\chi = 0.038 m^2 s^{-3}$ is used initially which is typically used for sea-swell waves [77]. The formula is shown in 3-3.

Origin of radiated free IG waves Separate simulations with only one coastline radiating free IG wave energy are conducted to distinguish the contribution of the coastline to the total IG energy observed in the measurement station.

3-3 Calibration and validation method

This section presents the methods used for data processing. First, the storms are selected to study the generation of IG waves under extreme climate conditions. During the period of each storm, measured data will be compared to the predicted ones derived from the corresponding time series of IG waves at a number of observation stations. As a result of the availability

of different measured data, only three main stations are used to do the calibration and the others can be examined as an additional reassurance.

The sea swell data are downloaded directly from ECMEF - ERA5, which requires to be processed to satisfy the input data format in SWAN. As SWAN computes the predicted IG parameters (H_{IG}, T_{IG}) over the North Sea during the storm period. The temporal output is commanded at measurement stations. To visualize the predicted results, post-processing scripts are developed using Python.

3-3-1 Storm

The storm period of interest is selected from measurement data in record The measuring data is directly from MES stations

The period is selected during typical storm conditions. The storms whose measured total IG wave height is higher than 10 cm are used to check the capability of SWAN since only severe storm conditions are considered.

Two storms Xaver and Friedhelm are used to calibrate the model since the source IG wave observed in stations from different coastlines has a special contribution each. First simulations without bottom friction (Section 4-1) are looked into to have a general understanding of the IG wave distribution and origins, which determines the difference of applied parameters for a different part of coastlines bordering the North Sea. The other storms will be left to validate the model after the proper coefficients are found.

Storm	Period	Duration (days)	$H_{SS,max}$ (m)	Peak time	$\theta_{SS,p}$ (°)
Xaver	2013-12-03 ~ 09	6	11.2	12-05, 21:00	-39
Egon	2017-01-09 ~ 15	6	10.4	01-13, 02:00	-
Friedhelm	2011-12-08 ~ 15	10.3	10.6	12-08, 22:00	-42
Axel	2017-01-01 ~ 08	7	9.7	01-03, 03:00	-42
Carmen	2010-11-10 ~ 15	5	6.4	11-11, 21:00	-109
Tini	2014-02-10 ~ 18	8	6.5	02-08, 21:00	-130
Ulli & Andrea	2012-01-02 ~ 08	6	9.9	01-03, 17:00	-135
Berit	2011-11-23 ~ 29	6	9.0	11-25, 00:00	-102
Christiaan	2013-10-25 ~ 30	5	6.3	10-31, 23:00	-41
Eleanor	2018-01-01 ~ 19	18	11.9	01-15, 02:00	-

Table 3-1: Storm information containing sea-swell wave parameters. Peak time means the time when sea swell wave height is the largest. $\theta_{SS,p}$ denotes the direction of the peak sea-swell wave height observed at station A12. Direction information of storm Egon and Eleanor are excluded due to data unavailability. Since not all of the storm centers happens in the middle of the North Sea, the $\theta_{SS,p}$ only gives part of the direction information of each storm.

3-3-2 Observation

Several measuring stations are inspected to have insight into the IG wave energy. Here the method of comparing the measured and predicted data will be elaborated.

Measuring stations In this study, the following 7 locations as shown in Table 3-2 are used to explore the prediction capability of the SWAN model. These stations have been recording the surface variations continuously since 2009. The collected data are used to determine manifold wave information including tide, surge, water level, sea swell, and part of IG wave conditions. These stations distributed around the North Sea have a range of depth from 18 m to 46 m (figure 3-3).

Measured data Measurement stations located in the North Sea have been recording the wave characteristics including sea-swell and longwave frequency band over the past nine years ($2010 \sim 2018$). Table 3-3 shows the two types of data collected in these stations. The raw data collected from instruments have been proceeded to the accessible data form. Sea-swell spectra in six consecutive 10min blocks are averaged and are combined with corresponding blocks of low-pass filtered surface elevation to create a set of hourly wave parameters [51].

Source of bound IG wave A12, Q1 and EUR stations measured sea-swell spectra which can be used to compute the bound IG wave height directly using Option B (see figure 3-2). While for the other four stations, the bound IG wave parameters are estimated from the ECMWF-WAM model given the lack of sea-swell spectra data (Option A in figure 3-2).

Name	Latitude (°)	Longitude (°)	Depth (m)
A12	55.417	3.817	32.6
Q1	52.925	4.150	28.2
EUR	51.998	3.275	34.8
D15	54.317	2.933	41.0
F16	54.117	4.017	46.6
IJM	52.488	4.263	18.2
LG	51.926	3.670	23.4

Table 3-2: The depths and the coordinates of observation locations

Observation	Frequency range (Hz)	Original data form
Sea-swell wave	$0.04 \sim 0.5$	surface elevation spectra
long wave	< 0.025	surface elevation time series

Table 3-3: Observed data form of sea swell wave and IG wave

3-3-3 Comparison with the measured data

The computation domain is over the North Sea domain, whose longitude from 5°W to 10°E and latitude from 50°N to 62°N.

The output IG wave parameters from SWAN gives the information of free IG wave. To compare the predicted free IG energy with measured free IG energy, the measured free IG

wave energy originally comes from total measured IG energy subtracting bound IG wave energy given by,

$$H_{IG,total} = \sqrt{H_{IG,f}^2 + H_{IG,b}^2}. \tag{3-11}$$

The skill defines the accuracy of the model prediction. According to Gallagher et al. (1998) [23] [50] and replace H_{rms} by H_s, we get:

$$skill = 1 - \frac{\sqrt{\overline{(H_{IG,m} - H_{IG,p})^2}}}{\sqrt{\overline{(H_{IG,m})^2}}}, \tag{3-12}$$

where the subscripts m and p refer to measured and predicted values and the overline means averaging.

Simulations are run for each coastline to look into the contribution separately. The combined free IG wave energy are used to be compared to the measured one. When bottom friction is not included in the simulation, the total IG wave height from all sources can be computed directly due to the linear relationship between α_1 and IG wave height instead of running the combined simulation with all coastlines again. The combines total IG wave height predicted is given by,

$$H_{IG,total} = \sqrt{(H_{IG,DEN}^2 + H_{IG,NL}^2 + H_{IG,NOR}^2 + H_{IG,UK}^2 + H_{IG,BE}^2 + H_{IG,GER}^2)}. \tag{3-13}$$

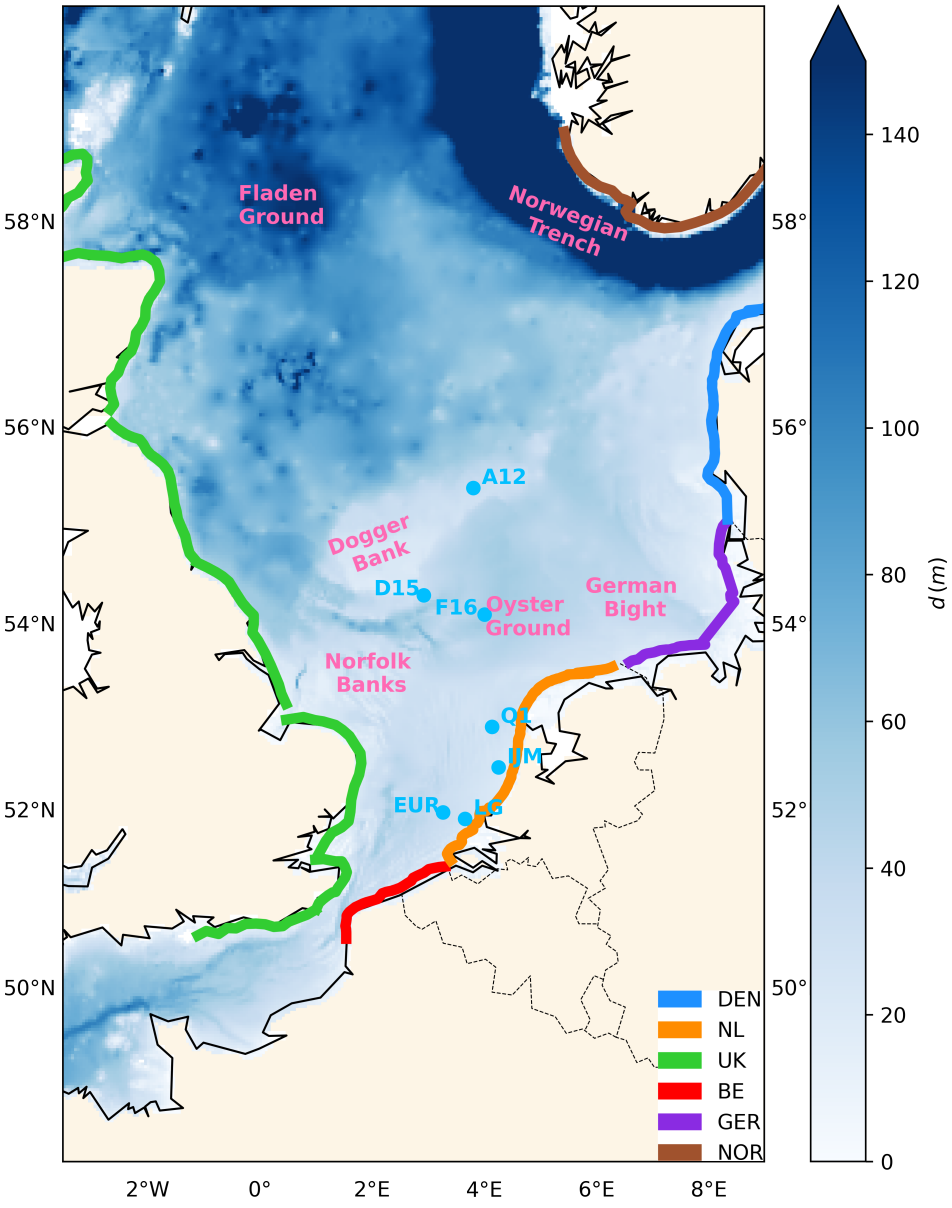

Figure 3-3: IG source coastlines and observation locations marked with geographic features

Chapter 4

Calibration

The calibration study is conducted to decide the combination set of source calibration parameter α_1 and friction coefficient χ for 2 storm events (Friedhelm and Xaver). To study the influence of bottom friction, simulations without bottom friction are compared to those with bottom friction. In both cases, the optimal results are given.

4-1 Simulations without bottom friction

The simulation results without bottom friction are illustrated here. There are 4 types of skills calculated to evaluate the prediction accuracy using the SWAN model: three separate skills using data from station A12, Q1 and EUR and one combined skill using all data from 3 stations. A constant $\alpha_{1,All}$ of $0.0018 s^{-1}$ is used for all coastlines first which is of the same order of magnitude as the values used in previous study [1].

A smaller difference between observed and predicted free IG wave height at station A12 can be noticed compared to Q1 and EUR when $\alpha_{1,All} = 0.0018\, s^{-1}$ (see figure 4-1a, 4-1b, 4-1c and 4-1d, 4-1f). It is observed that DEN is the dominant contributor to the total IG energy especially at station A12 both for Xaver and Friedhelm. The trend of the black line (total predicted free IG wave) and the green line (IG wave energy from DEN coastline) are similar, see figure 4-1a and figure 4-1d. The dominance of DEN is more apparent in Friedhelm since the other coastlines show a marginal contribution compared to Xaver. Storm Friedhelm provides us a good chance to look into the influence of the DEN coastline radiating IG source energy prominently.

At A12, it is noted the predicted IG wave height seems to lag behind the measured ones especially in Friedhelm, as shown in figure 4-1d. The peak of the measured and predicted wave height occurs at Day 2 and Day 3.5 respectively. Prior to the peak of the storm, a large discrepancy between measured and predicted data appears at A12 (figure 4-1a and 4-1d). The measured total IG wave captures the signals of IG wave energy that are not from radiation. In addition, the IG energy level is poorly predicted out of the storm. The proportion of missing energy source before the peak of the storm and even before and after the thrust of the storm

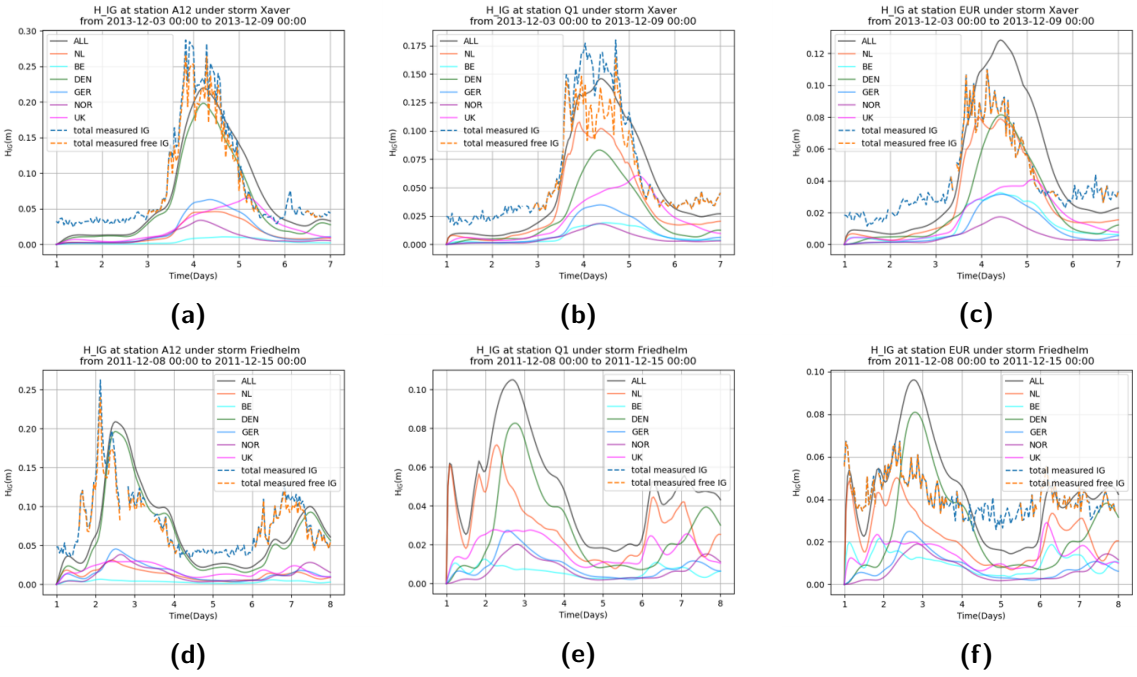

Figure 4-1: Variation of IG wave height and contributions of individual coastlines at A12, Q1 and EUR over storm Xaver (a,b,c) and Friedhelm (d,e,f), $\alpha_1 = 0.0018\,s^{-1}$ at station A12 (a,d), EUR (b,e), and EUR (c,f) with a constant $\alpha_1 = 0.0018\,s^{-1}$.

indicates the generation of IG wave energy from other mechanisms that are not considered in the SWAN model. An assumption is the local generation of IG wave due to the topography changes or regional climate variations. On top of that, the IG wave radiating from other coastlines and previous storms could also play a role.

At EUR, the predicted free IG line goes far beyond the measured free IG line following the shape of DEN line (figure 4-1c and 4-1f). The dissipation mechanism is required to attenuate the part of energy exceeding the measured IG wave energy level. The exclusion of bottom friction might explain the overprediction here.

Next we have a look at the different performances for storm Xaver and Friedhelm. Overall, the highest IG wave height with 25 cm is observed at station A12 both during storm Xaver and Friedhelm in which the energy from DEN dominates (figure 4-1a and 4-1d). Focusing on storm Xaver, we can observe the growth of UK line at the tail of the storm in Day 5 (figure 4-1a, 4-1b and 4-1c). It turns into a major contributor over the DEN and NL in Day 4 behind the peak of the storm. Moreover, a higher contribution of free IG waves from NL is detected at Q1 and EUR than at A12, where the measurement stations is positioned close to NL coastline.

The observed differences of dominate coastlines and magnitude of IG wave height in measurement stations are related to the direction of the storm. During storm Xaver, the sea-swell waves coming from north-west head to the DEN coastlines and the reflected IG waves travel across the sea, reaching the south of UK. The highest IG wave height at UK therefore lag behind the highest IG wave height at DEN or NL as IG wave requires time to cross from DEN to UK.

In general, SWAN performs better for storm Xaver than for Friedhelm using the calibration parameter value $\alpha_1 = 0.0018\,s^{-1}$. The underprediction problem before the peak of storm at A12 is not as apparent as under storm Friedhelm. However, same patterns at A12 are noticed for other storms (see appendix from figure A-9a to A-14a). To decrease the impacts from this problem, only partial data, namely the data after peak of the storm will be used in the following skill calculation at A12.

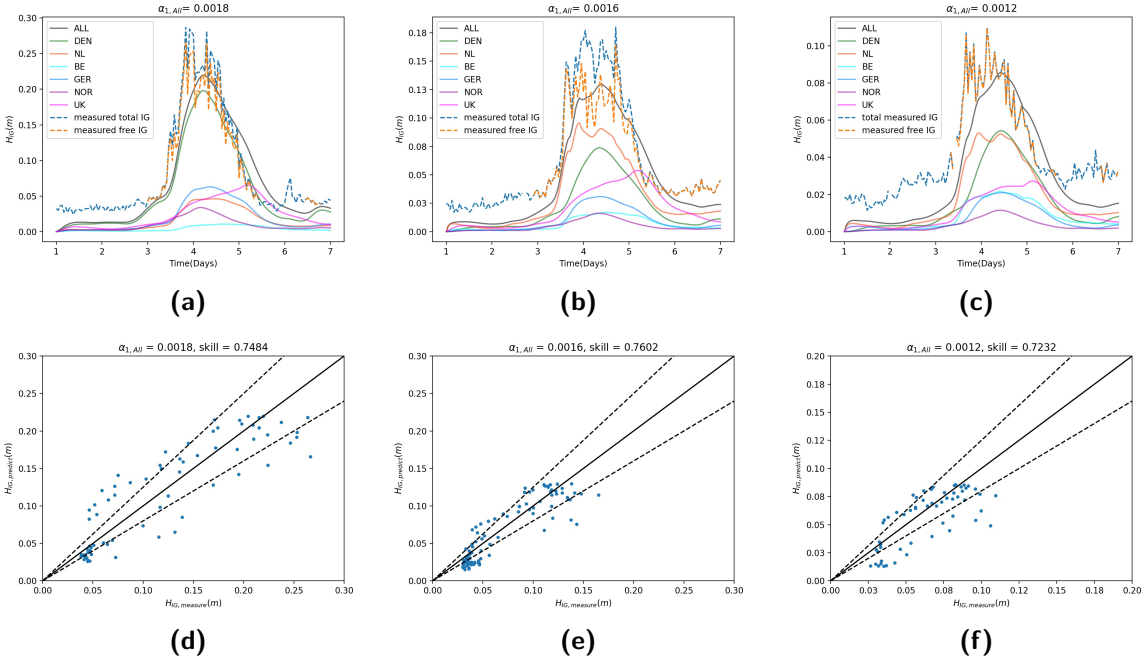

Figure 4-2: Variation of IG wave height (top panels) and comparison of the modeled $H_{IG,predict}$ and measured $H_{IG,measure}$ (bottom panels) at A12, Q1 and EUR over storm Xaver, A12: $\alpha_1 = 0.0018\,s^{-1}$, Q1: $\alpha_1 = 0.0016\,s^{-1}$, EUR: $\alpha_1 = 0.0012\,s^{-1}$, no bottom friction. 20% error bands are indicated by the dashed lines (d,e,f).

The influence of radiated IG wave energy can be observed via varying the α_1 value excluding the impacts from bottom friction. The α_1 is kept constant for each coastline in the simulations. figure 4-2a, 4-2b and 4-2c shows a variance of the optimum result for each station under storm Xaver. A lower $\alpha_{1,ALL}$ at EUR implies a potential compensate for the friction dissipation (figure 4-2c). The reduction of radiation energy from DEN at Q1 also gives a slightly better fit between measured and predicted wave height (figure 4-2b).

For storm Friedhelm followed by a smaller storm Hergen, the modulation of $\alpha_{1,All}$ does not give a better result at EUR as shown in figure 4-3d, which means the excessive radiation energy is not the main reason causing the weak prediction. The trend of the total measured free IG wave height line follows the changes in turns and peaks of NL line in figure 4-3b, suggesting the dominant influence at EUR from NL coastline.

The variation of the skill with varying $\alpha_{1,ALL}$ for each station is shown in figure 4-4a under storm Friedhelm. The two key parameters used to assess the accuracy of model results are mean skill and standard deviation of skill. Mean skill tells the result with the highest capability on average. Standard deviation describes the variability among different stations.

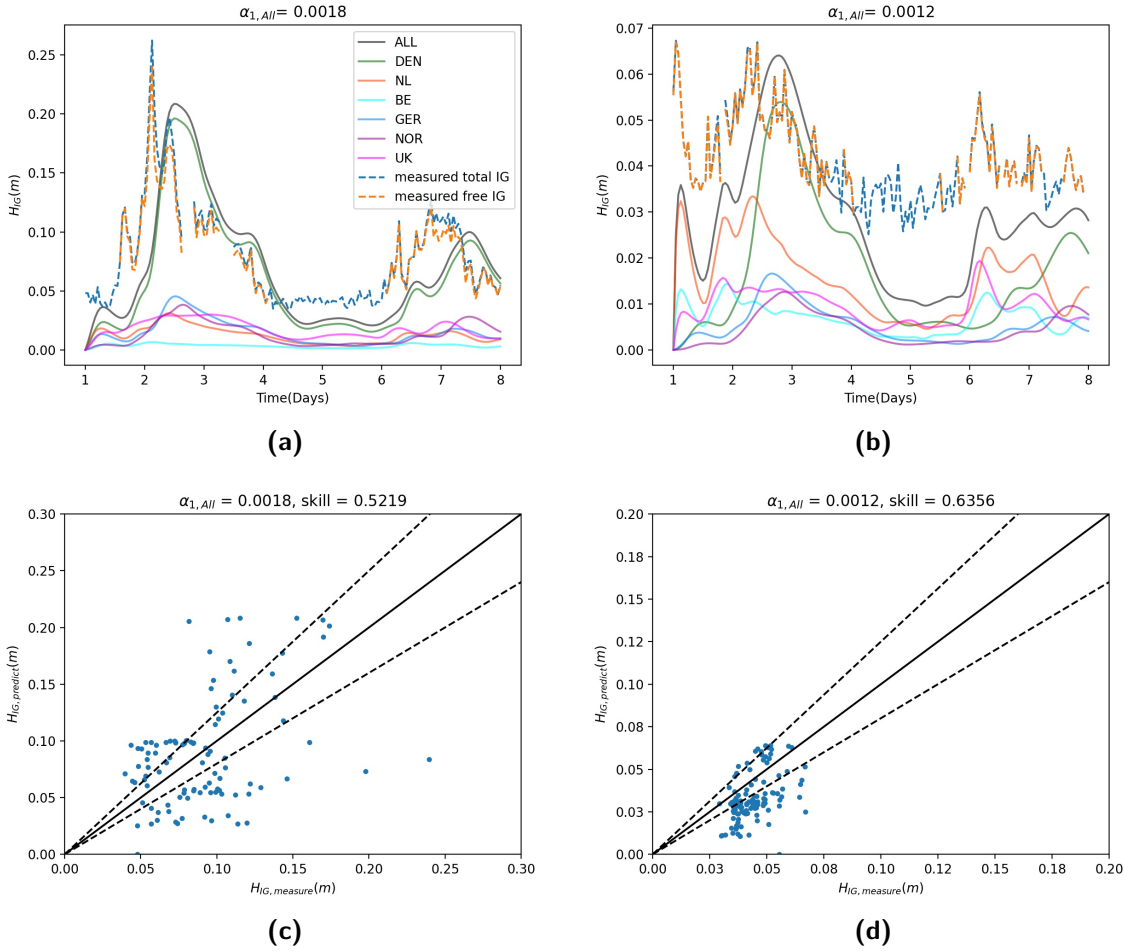

Figure 4-3: Variation of IG wave height (top panels) and comparison of the modeled $H_{IG,predict}$ and measured $H_{IG,measure}$ (bottom panels) at A12, Q1 and EUR over storm Fridhelm, A12: $\alpha_1 = 0.0018\,s^{-1}$, EUR: $\alpha_1 = 0.0012\,s^{-1}$, no bottom friction. 20% error bands are indicated by the dashed lines (c,d).

Our goal is to find a combination with the mean skill as high as possible and with the standard deviation as low as possible.

For Friedhelm, the optimum calibration value is approximately $\alpha_{1,All} = 0.0012\,s^{-1}$. When $\alpha_{1,All} = 0.0017\,s^{-1}$, the standard deviation among 3 stations is the smallest. Since only the DEN is the main contributor, this value could be a reference of $\alpha_{1,DEN}$ for subsequent simulations applying different source energy for separate coastlines.

The use of partial skill increases the skill value marginally for Xaver but largely for Friedhelm since the underprediction before the storm is less for Xaver than for Fredhelm at A12 (comparing the mean skill line between figure 4-4a and 4-4b for Fridhelm, and figure 4-4c and 4-4d for Xaver).

4-2 Simulations with bottom friction

Only varying source calibration parameter α_1 does not improve the simulation results. Based on our analysis, the simulation results including bottom friction are inspected in this section.

First, the source calibration parameter is kept constant for each coastline. Through varying the value of $\alpha 1_{1,ALL}$ and χ (which is also written as C_b in equation 3-3), we expect to discover the relationship between two variables and to obtain an optimum combination. Next, a constant χ with several varying α_1 applied to different coastlines will be looked into to refine the variation of source energy from original regions.

4-2-1 Varying calibration parameter for entire coastlines and friction coefficient

Figure 4-5a and 4-5b shows an correlation between friction coefficient χ and calibration parameter $\alpha_{1,All}$ under storm Friedhelm and the optimum combination can be found with low standard deviation and high mean skill values. The highest skill is found when $\alpha_{1,All} = 0.0026$ and $\chi = 0.032$ with a mean skill value 0.78. Since the DEN coastline dominates over other coastlines radiating IG wave energy in storm Friedhelm, the combination with high mean skill is consistent with those with low standard deviation, showing less discrepancy between A12, Q1 and EUR. For Xaver, we can observe the same "linear" correlation between $\alpha_{1,All}$ and χ in figure 4-5c. As long as we select small $\alpha_{1,All}$ combined with small χ or large $\alpha_{1,All}$ combined with large χ, the optimum calculated skill has minor fluctuations. Since our next step is to allocate different source calibration parameter values to each coastline, a proper χ is required first. The skill with this χ value should have a high average value and a low spreading in three stations. Thus $\chi = 0.010$ is chosen to do the following calibration deriving from figure 4-5c and figure 4-5d.

Storm	Criteria	χ	$\alpha_{1,All}$	Mean skill	Standard deviation
Friedhelm	SD	0.022	0.0022	0.7663	0.0016
	M	0.032	0.0026	0.7802	0.0072
Xaver	SD	0.006	0.0016	0.7361	0.0025
	M	0.018	0.0022	0.7544	0.0310

Table 4-1: The optimum combinations of $\alpha_{1,All}$ and χ, SD means the result is based on minimum standard deviation and M means the result is based on the maximum mean skill value.

Referring to figure 4-5a and 4-5b, the two combinations using two criteria do not show much variation in mean skill and standard deviation, verifying again that only DEN matters in Friedhelm. For Xaver, the two combinations show a marginal improvement in mean skill but the values of standard deviation deteriorate 10 times. It thus becomes a trade-off problem, whether we pursue a better result for three stations or a good averaging performance for each station. The figures showing the variation of IG wave height over the storm period will be given enabling us to select an optimum combination visually.

We can have a look at the skill variations in detail at each station and for combined situations in figure 4-6a and 4-6b. The constant $\alpha_{1,All}$ and χ value are chosen from the optimum result with the highest mean skill under Xaver. The varying of χ and $\alpha_{1,All}$ at x-axis thus accounts

for the influence from the friction dissipation and the calibration of source energy while keeping the other variable constant.

In figure 4-6a, the increasing value of friction coefficient χ results in an obvious increase of EUR skill while imposing little influence on other stations. It shows a larger impact on EUR station through varying the friction coefficient. Varying the source energy calibration parameter $\alpha_{1,All}$ has a larger impact on all stations compared to the varying of χ, see figure 4-6a and figure 4-6b. EUR is the most sensitive one with the largest variation in skill in both cases.

The peak skill shows less difference between A12 and Q1 but not the same case at EUR. It is assumed the variation of skill from EUR would largely influence the choice of optimum combination.

4-2-2 Varying calibration parameter for three parts of coastlines

From section 4-1, $\chi = 0.010\, m^2 s^{-3}$ is kept constant in the calibration process varying three different α_1 value here using storm Xaver. According to the contributions to IG wave energy from different regions, we separate all the coastlines into 3 parts: UK as the first part, BE, NL and GER as the second part, DEN and NOR as the third part referring to figure 3-3. $\alpha_{1,UK}$ used in the titles of figures means the value applied only for UK, while $\alpha_{1,NL}$ means for BE, NL and GER and $\alpha_{1,DEN}$ means for DEN and NOR.

Keeping $\alpha_{1,UK}$ constant, the variation of $\alpha_{1,NL}$ and $\alpha_{1,DEN}$ gives convergent results. The optimum result with highest mean skill is shown in the yellow zone in the middle of figure 4-7a. However, the optimum combination with lowest standard deviation (SD) lies at bottom left with a lower $\alpha_{1,DEN}$.

Keeping $\alpha_{1,NL}$ constant, the optimum combination with highest mean skill (M) value is replaced by a strip instead of an enclosing circle, indicating that the variation of $\alpha_{1,UK}$ does not influence the optimum $\alpha_{1,DEN}$ value. $\alpha_{1,DEN}$ maintains around 0.0022 ignoring the variation of $\alpha_{1,UK}$ if $\alpha_{1,UK} < 0.0013$. A larger $\alpha_{1,UK}$ will not give a better result. In terms of SD in figure 4-7d, the less spreading result is present in a lower $\alpha_{1,DEN}$ value.

Keeping $\alpha_{1,DEN}$ constant, a similar behaviour is observed as the case with constant $\alpha_{1,NL}$. The difference exists in contour map of SD, where the least spreading results combines a higher $\alpha_{1,UK}$ and a lower $\alpha_{1,NL}$.

For 3 cases with varying α_1 for specific coastline or coastlines, we extract the two combinations from each with the lowest SD value and highest M value. Combining all 6 combinations, only the one with highest M value and the three with lowest SD value are left to inspect the variation of IG wave height in details. A summary of the optimum combinations from Xaver is shown in table 4-2.

To sum up, the first combination with $\alpha_{1,All} = 0.0016\, s^{-1}$ and $\chi = 0.006\, m^2 s^{-3}$ and the second combination with $\alpha_{1,UK} = 0.0014\, s^{-1}$, $\alpha_{1,NL} = 0.0016\, s^{-1}$, $\alpha_{1,DEN} = 0.0022\, s^{-1}$ and $\chi = 0.010\, m^2 s^{-3}$ will be used for the validation.

Combination	Storm	χ	$\alpha_{1,UK}$	$\alpha_{1,NL}$	$\alpha_{1,DEN}$	M	SD	Figure
1	Friedhelm	0.032		0.0026		0.7802	0.0072	A-1
2	Xaver	0.006		0.0016		0.7361	0.0025	A-2
3	Xaver		0.0010	0.0018	0.0020	0.7431	0.0032	A-3
4	Xaver		0.0010	0.0018	0.0018	0.7461	0.0032	A-4
5	Xaver	0.010	0.0012	0.0018	0.0018	0.7472	0.0007	A-5
6	Xaver		0.0014	0.0016	0.0022	0.7553	0.0336	A-6
7	Xaver		0.0008	0.0018	0.0022	0.7625	0.0348	A-7

Table 4-2: A summary of optimum combinations. Combination 1 and 2 has 2 variables χ and $\alpha_{1,All}$. Combination 3 7 has a constant χ and 3 variables $\alpha_{1,UK}$, $\alpha_{1,NL}$ and $\alpha_{1,DEN}$.

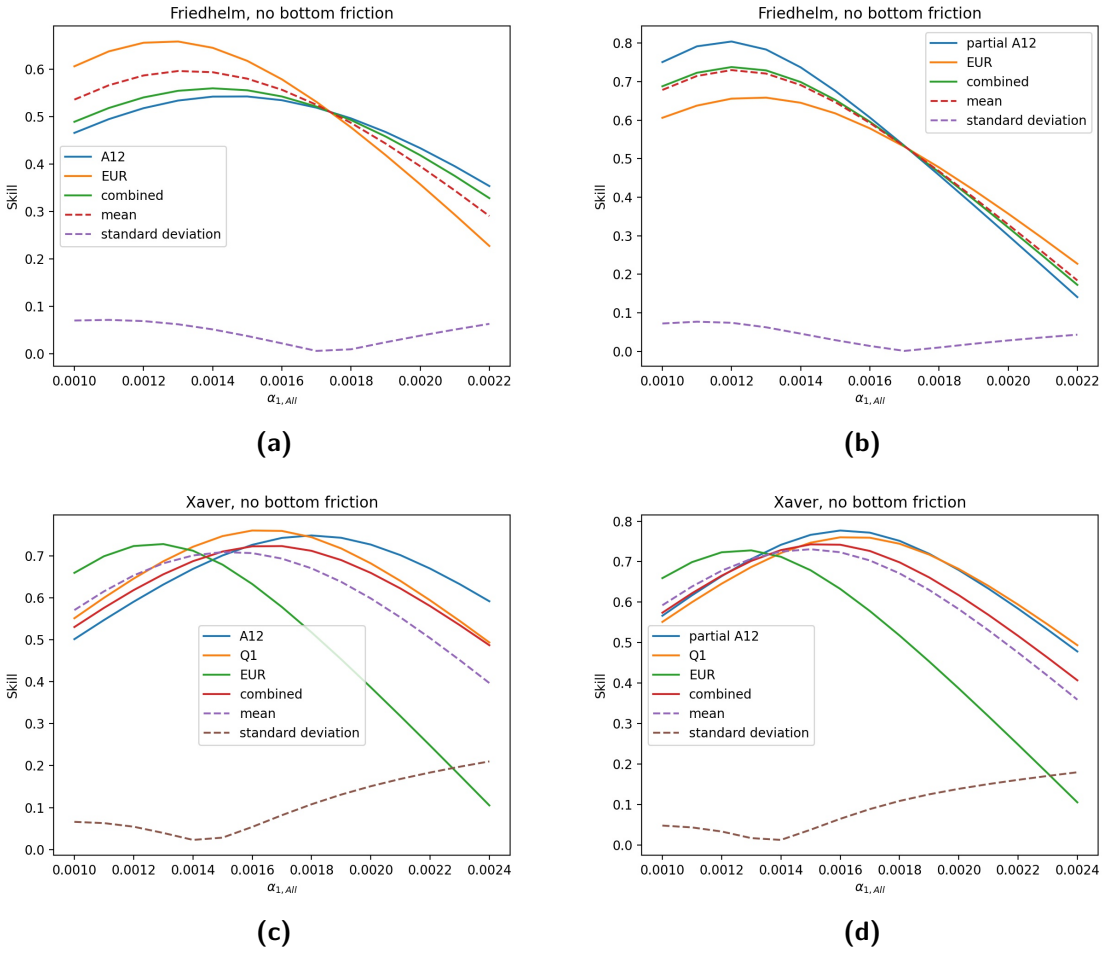

Figure 4-4: Skill variation as a function of varying α_1 in different stations for storm Xaver (a,b) and Friedhelm (c,d). Comparing the skill lines (a,c) using complete A12 data and (b,d) using A12 data after the peak of the storm, the mean skill improves marginally. To remove the underprediction due to the ignorance of other physical processes prior to the peak of the storm at A12, only partial A12 data is included in the following skill calculation. Friedhelm (b):The optimum $\alpha_{1,All} = 0.0012\,s^{-1}$ and the least spreading shows with a smaller $\alpha_{1,All} = 0.0017\,s^{-1}$. Xaver (d): The optimum $\alpha_{1,All} = 0.0016\,s^{-1}$ and the least spreading shows with a smaller $\alpha_{1,All} = 0.0014\,s^{-1}$.

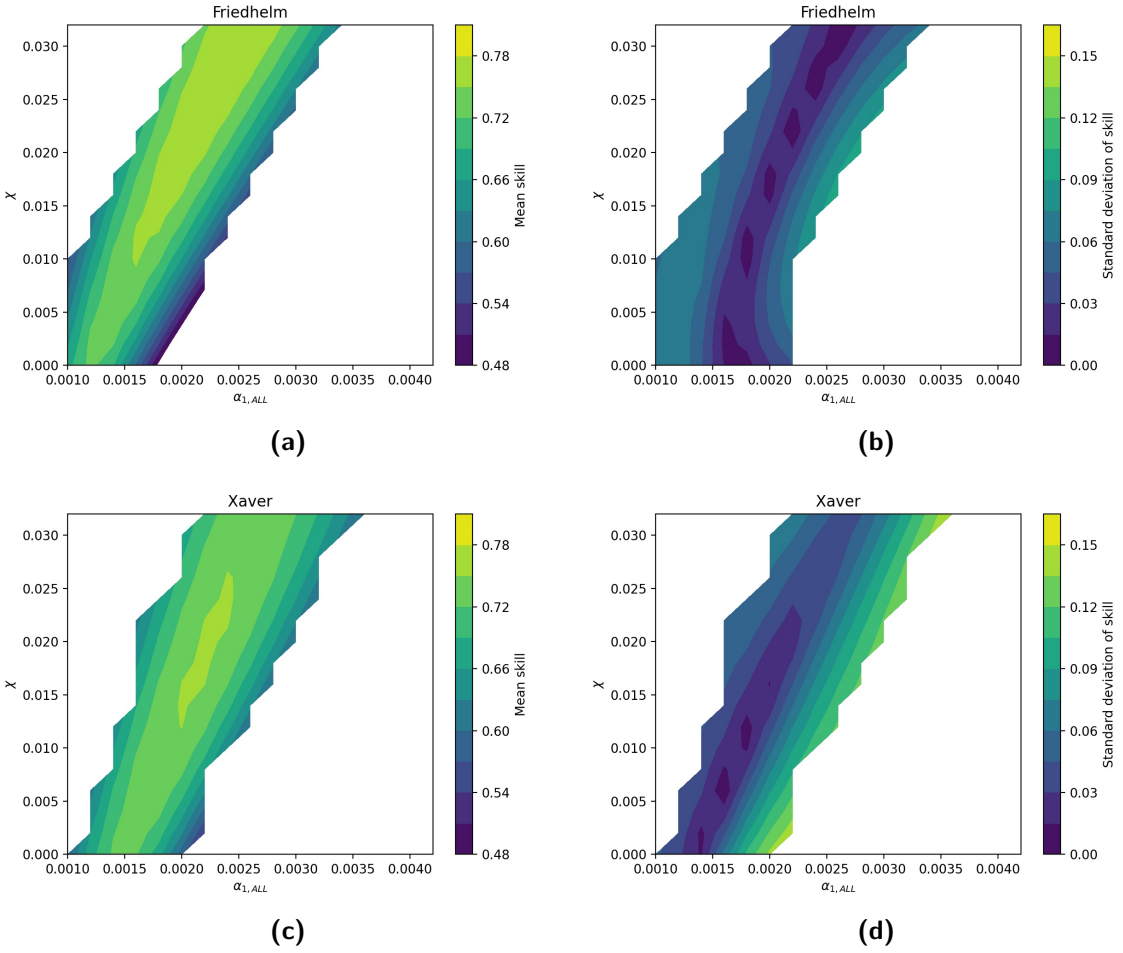

Figure 4-5: Mean (a,c) and standard deviation skills (b,d) between different observations stations as a function of varying combinations between α_1 and χ for Friedhelm (top panels) and Xaver (bottom panels). Left (a,c): The highest mean skill is shown in the middle with lightest color. Right (b,d): The lowest standard deviation is located in the left bottom color with small values on both α_1 and χ.

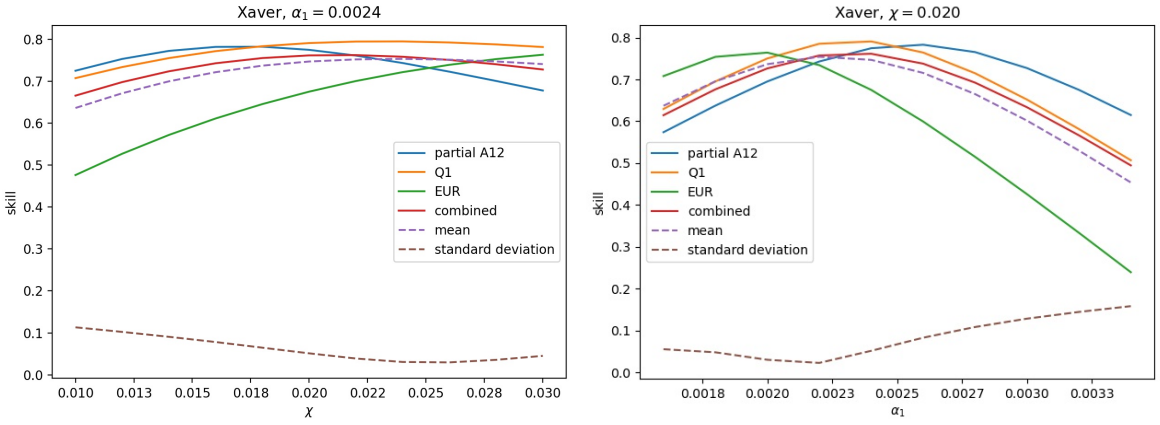

(a) **(b)**

Figure 4-6: Skill variation as a function of χ (a) and α_1 (b) for Xaver to inspect the influence of calibration parameter and bottom friction coefficient. $\alpha_1 = 0.0024\,s^{-1}$ in panel (a) and $\chi = 0.020\,m^2 s^{-3}$ in panel (b).

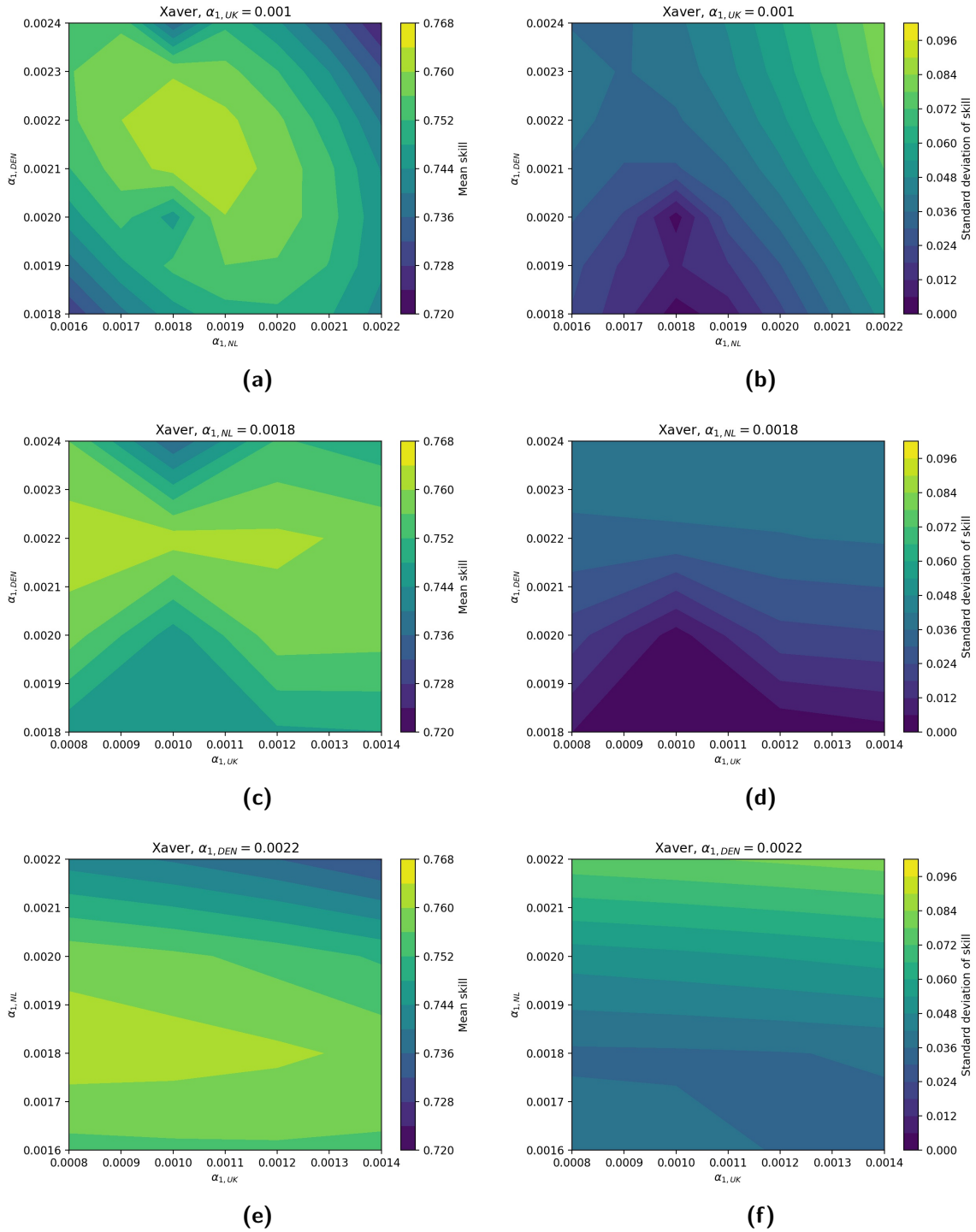

Figure 4-7: Xaver: The mean skill (left) and standard deviation (right) for constant $\chi = 0.010\,m^2s^{-3}$ and varying $\alpha_{1,NL}$ and $\alpha_{1,DEN}$ (a,b), varying $\alpha_{1,UK}$ and $\alpha_{1,DEN}$ (c,d), and varying $\alpha_{1,UK}$ and $\alpha_{1,NL}$ (e,f). (a,b): The yellow zone of left panel in the middle shows the range of the combinations with highest mean skill and the darkest zone in right panel deviates from the middle yellow zone of left panel. (c,e): The lightest yellow zone is nearly horizontal, indicating the variation of $\alpha_{1,UK}$ does not affect the optimum combination of $\alpha_{1,NL}$ and $\alpha_{1,DEN}$ much as long as $\alpha_{1,UK} < 0.0013\,s^{-1}$. (c,d): Smaller $\alpha_{1,DEN}$ gives lower standard deviation value and a low mean skill as well.

Chapter 5

Validation

This chapter presents the validation results showing the accuracy of the model. 3 representative storms showing the extreme ($H_{SS,max} > 10m$), moderate ($7m < H_{SS,max} < 10m$) and mild storm ($H_{SS,max} < 7m$) events will be presented and discussed separately.

5-1 Extreme storm: Xaver

Xaver is a large storm tracked from the northwest to southeast with the highest sea-swell wave magnitude of 11m close to the DEN coasts. The peak of the storm occurs at 2013-12-05 21:00. The SS bulk wave towards the DEN coasts is reflected and spread in all directions to the sea.

Focusing on the IG pattern when DEN radiates a large amount of free IG energy, they are observed reaching the opposite coasts at the south of UK, NL and BE coasts most. A part of them spread towards the NOR coast. Because of the channel surrounded in front of the NOR island, the IG wave energy can barely reach NOR coasts. The north of NL received more energy exposed directly to the radiation IG energy from DEN coastline while the south of NL and BE coasts received marginal energy.

Comparing the dashed green line and dashed red line representing the variation of the free IG wave height over storm Xaver in figure 5-1a at each location, there is minor discrimination between 2 combinations at A12, D15 and F16. A higher value in $\alpha_{1,DEN}$ leads to a higher energy release from DEN coasts as the major source contributing to the free IG energy in the open sea especially at peaks of storm. Apart from these stations located in the centre of the south North Sea, the refined combination applying varying α_1 for different coastlines does not improve the model-data match. This could be the reason that the energy from DEN is attenuated when reaching the remote coastlines such as NL and UK and energy radiated from DEN coastline is not the dominate one along local shorelines.

Looking into the different contributions of each coastline at different locations in figure 5-1b, EUR and Q1 are dominated by free IG energy from NL and the second rank is DEN over

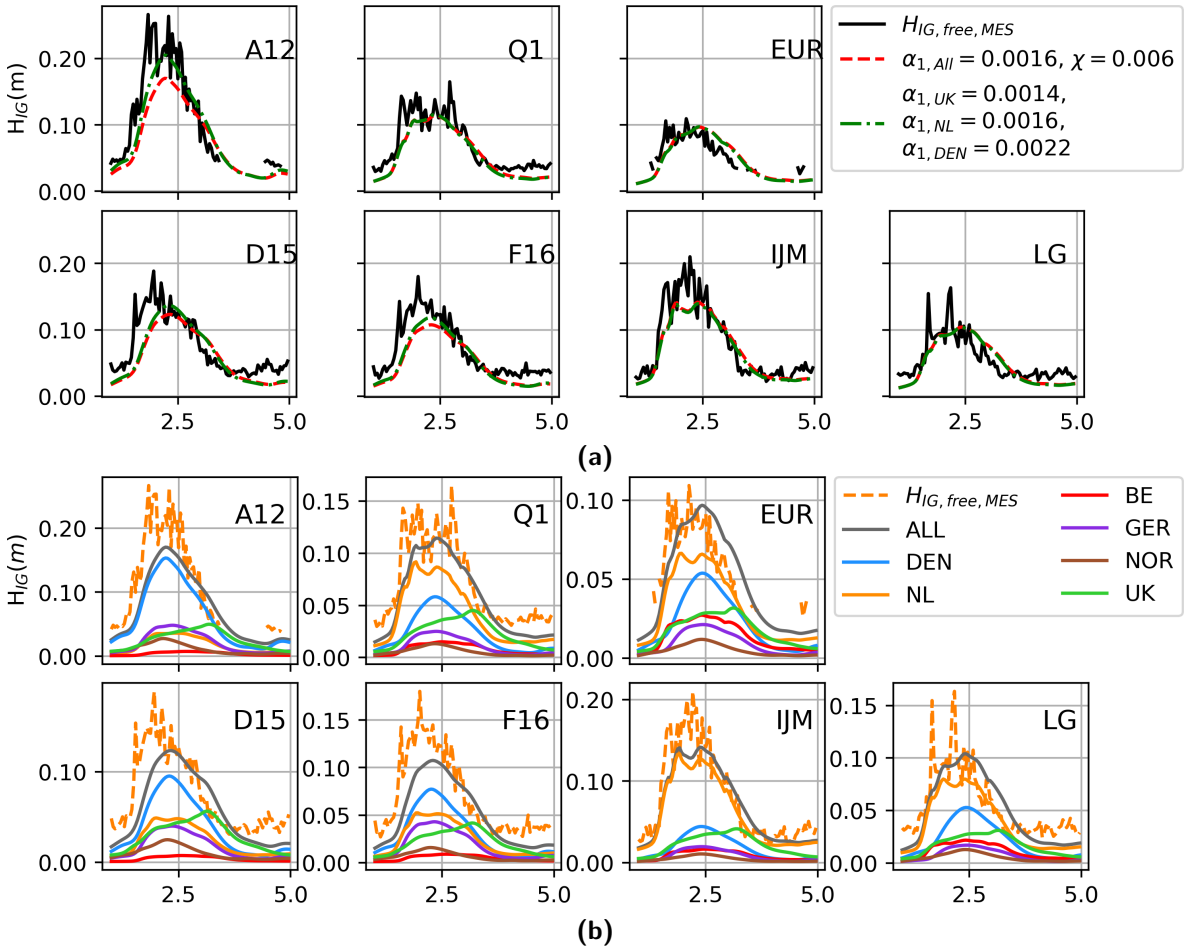

Figure 5-1: The variation of H_{IG} at same scales with 2 combinations indicated in legend (a), and the contributions from individual coasts to observed free IG wave height at different scales (b) in 7 observation stations over storm Xaver. (b): Colors of solid lines represent different original coastline. The solid black line in top panel (a) and the dashed orange line in bottom panel (b) all refers to free IG wave from observation.

entire storm period. At the tail of the storm, the contribution from UK grows and has the same magnitude as the decreasing NL and DEN. DEN accounts for the major IG wave energy at A12, almost follow the shape of the total IG wave line. DEN coastline dominate at D15 and F15, and NL coastline dominates at IJM and LG respectively.

5-2 Moderate storm: Axel

The burst of the Axel storm from north passes the salient part of Norway island and then approaches the DEN coastlines. Moving forward, the large SS wave hits the NL coastlines, the south border of the North Sea. The highest SS wave height is measured 9.7m at 2017-01-13 23:00. The track of the storm mainly influence the eastern border of the North Sea.

Free IG wave energy are mainly released from DEN coastline. North of NL is also under the direct impact of storm. With a time lagging, UK received the energy conveyed from DEN

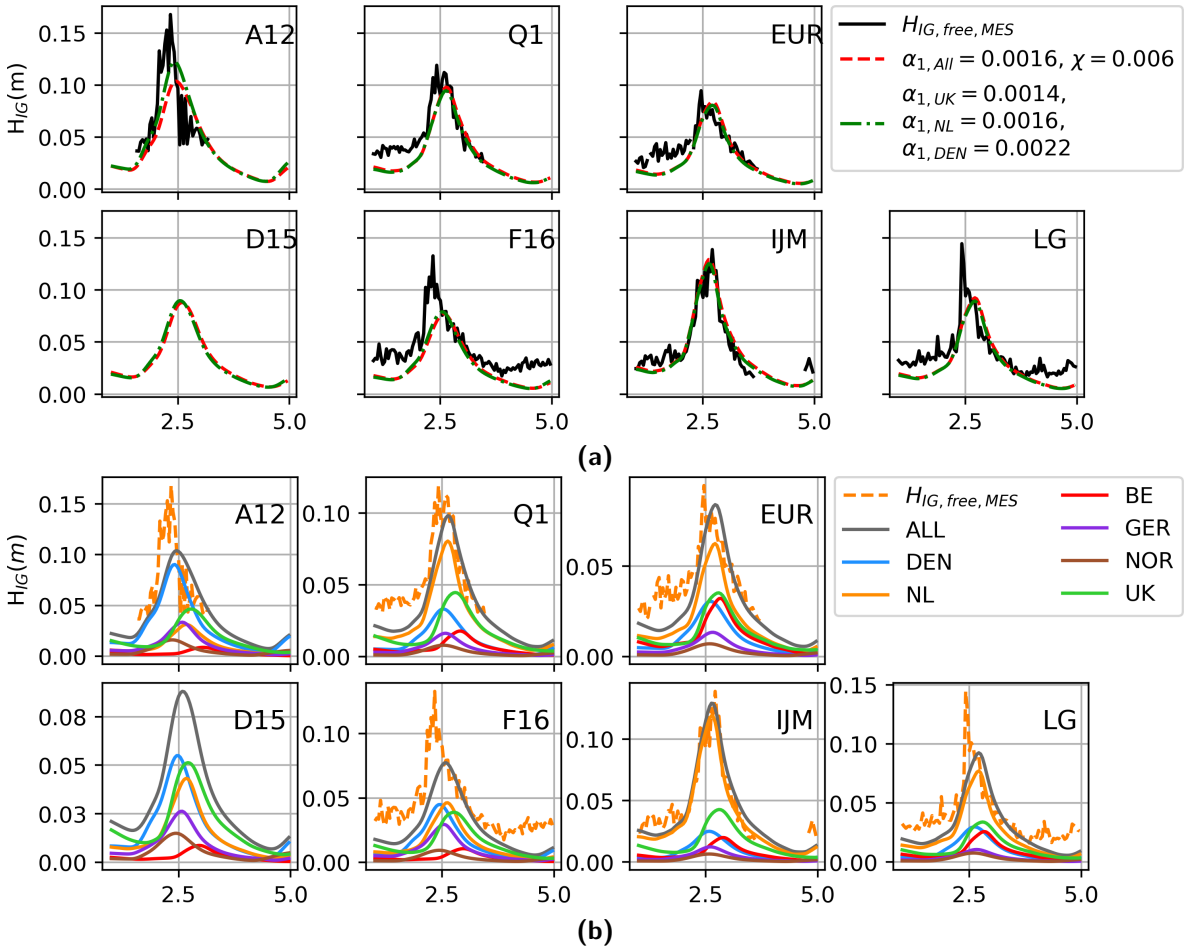

Figure 5-2: The variation of H_{IG} at same scales with 2 combinations indicated in legend (a), and the contributions from individual coasts to observed free IG wave height at different scales (b) in 7 observation stations over storm Axel.

and NL.

Comparing two combinations in figure 5-2a, decreasing the source energy of UK and increasing the source energy of DEN gives a better fit at A12. The general idea is that increasing the $\alpha_{1,DEN}$ cause the rise of predicted free IG line at A12 while it has marginal impacts on Q1 and EUR.

Looking at figure 5-2b, a large difference is shown in terms of the underprediction at both A12 and Q1 before the peak of the storm. After the peak of the storm, the two lines of measured and predicted free IG wave height can match pretty well especially at Q1 and EUR. We assume that free IG energy generated from other sources also play a role before the peak of the storm. The main contributor under storm Axel is DEN at A12 and NL at Q1 and EUR.

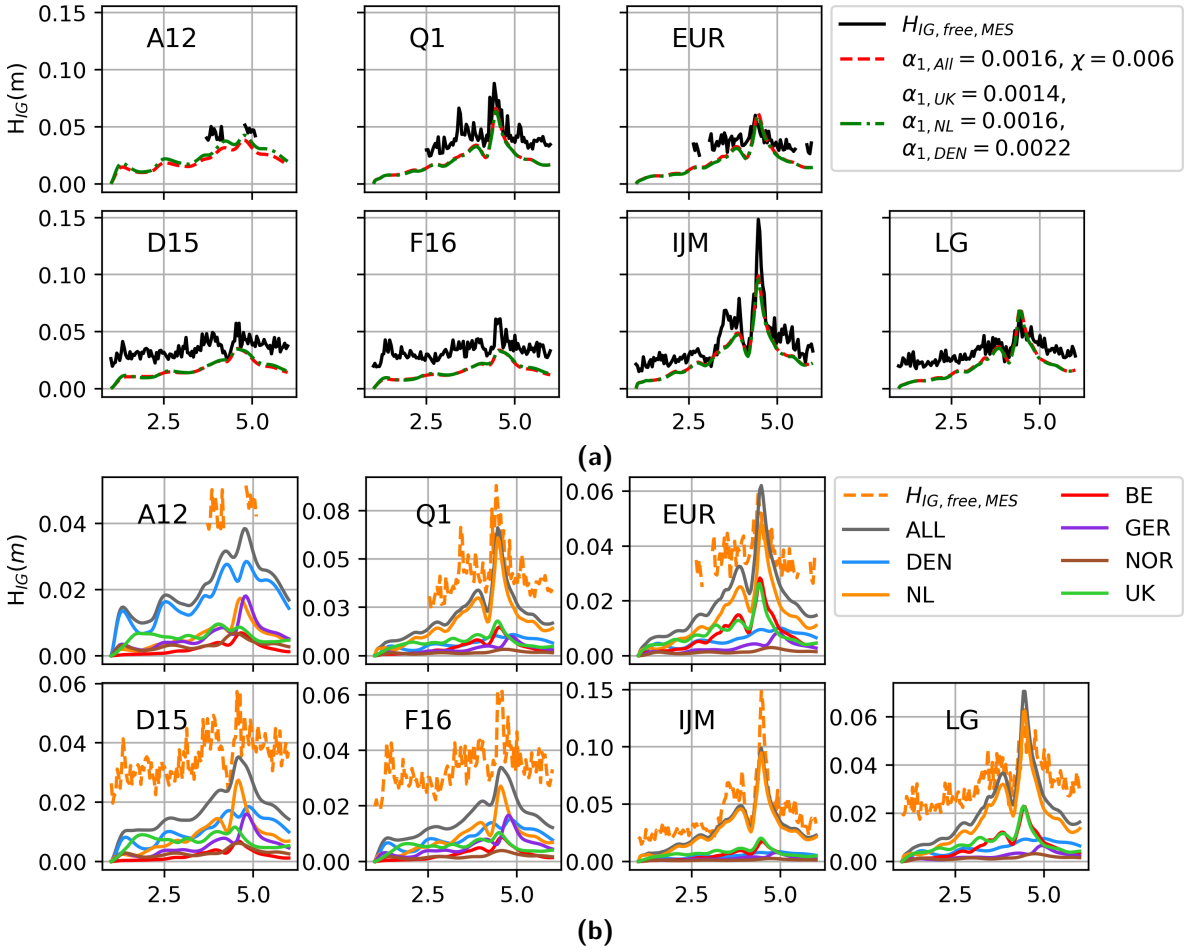

Figure 5-3: The variation of H_{IG} at same scales with 2 combinations indicated in legend (a), and the contributions from individual coasts to observed free IG wave height at different scales (b) in 7 observation stations over storm Christiaan.

5-3 Small storm: Christiaan

Christiaan is a small storm, the moving direction of which is from southwest to northeast along the east border of the North Sea. The centre of the storm cloud ends at the GER, influencing DEN and north of NL regions as well. The peak of the storm occurs at 2013-10-28 14:00 with the highest SS wave height 6.3m.

Following the track of the storm Christiaan, the maximum free IG wave height occurs at 8:00 at the bottom of UK. Later the concentration of free IG wave shows at NL coast at 12:00, and finally arrived at DEN at 14:00. The coastlines where energetic storm hit radiate free IG wave energy of different levels. The maximal SS wave energy level is observed close to the NL coast in which case the peak of measured total IG wave height is at Q1 with a magnitude of 10 cm. In contrast, the lowest measured total IG wave height show in station A12. NL coastline is the main contributor of free IG wave energy over Christiaan while DEN still accounts for the largest portion at A12 (see figure 5-3b).

Comparing two combinations in figure 5-3a, the impact of increasing $\alpha_{1,DEN}$ is minor at A12

due to a small magnitude of observed free IG wave variance compared to the extreme storm Xaver and moderate storm Axel. Though SWAN captures the peaks of observed free IG wave height properly but fails to explain the occurrence of marginal IG wave energy level at the onset and waning of the storm.

5-4 Overall result

The previous section analyse variation of free IG wave levels for different storms characteristics. To validate the SWAN model further using the two combinations (the first one: $\alpha_1 = 0.0016\,s^{-1}$, $\chi = 0.006\,m^2s^{-3}$; the second one: $\alpha_{1,UK} = 0.0014\,s^{-1}$, $\alpha_{1,NL} = 0.0016\,s^{-1}$, $\alpha_{1,DEN} = 0.0022\,s^{-1}$, $\chi = 0.010\,m^2s^{-3}$), the data set combining all storms and three main observation stations (A12, Q1 and EUR, where bound IG wave height is available) is used to examine the skill of the model. To get rid of the observed IG wave out of storm periods, a part of free IG wave with $H_{IG,measure} < 0.05m$ is excluded in the skill calculation.

As there are two different bound IG sources in different stations, first we can have a look at the accuracy of the data comparing the WAM-estimated $H_{IG,bound,WAM}$ to the measuring $H_{IG,bound,MES}$ as shown in figure 7-1. A good similarity of the two bound IG wave sources can provide another potential data source to do future verification of modeled results apart from observation.

The same results using the WAM-estimated bound IG wave are shown in figure 5-4c and 5-4d with a slightly lower skill in both combinations than the case using measuring bound IG terms. It shows that using WAM-estimated $H_{IG,bound}$ can provide a similar result as measured $H_{IG,bound}$ if observation data is not available.

For first combination with a constant $\alpha_{1,ALL}$ and χ, the output of the modeled IG wave height tends to be underpredicted (see figure 5-4a or 5-4c). Via decreasing $\alpha_{1,UK}$ and increasing $\alpha_{1,DEN}$, though the spreading of the scatter data is not improved, the underprediction and overprediction shows a symmetrical pattern, indicating an average promotion of different stations.

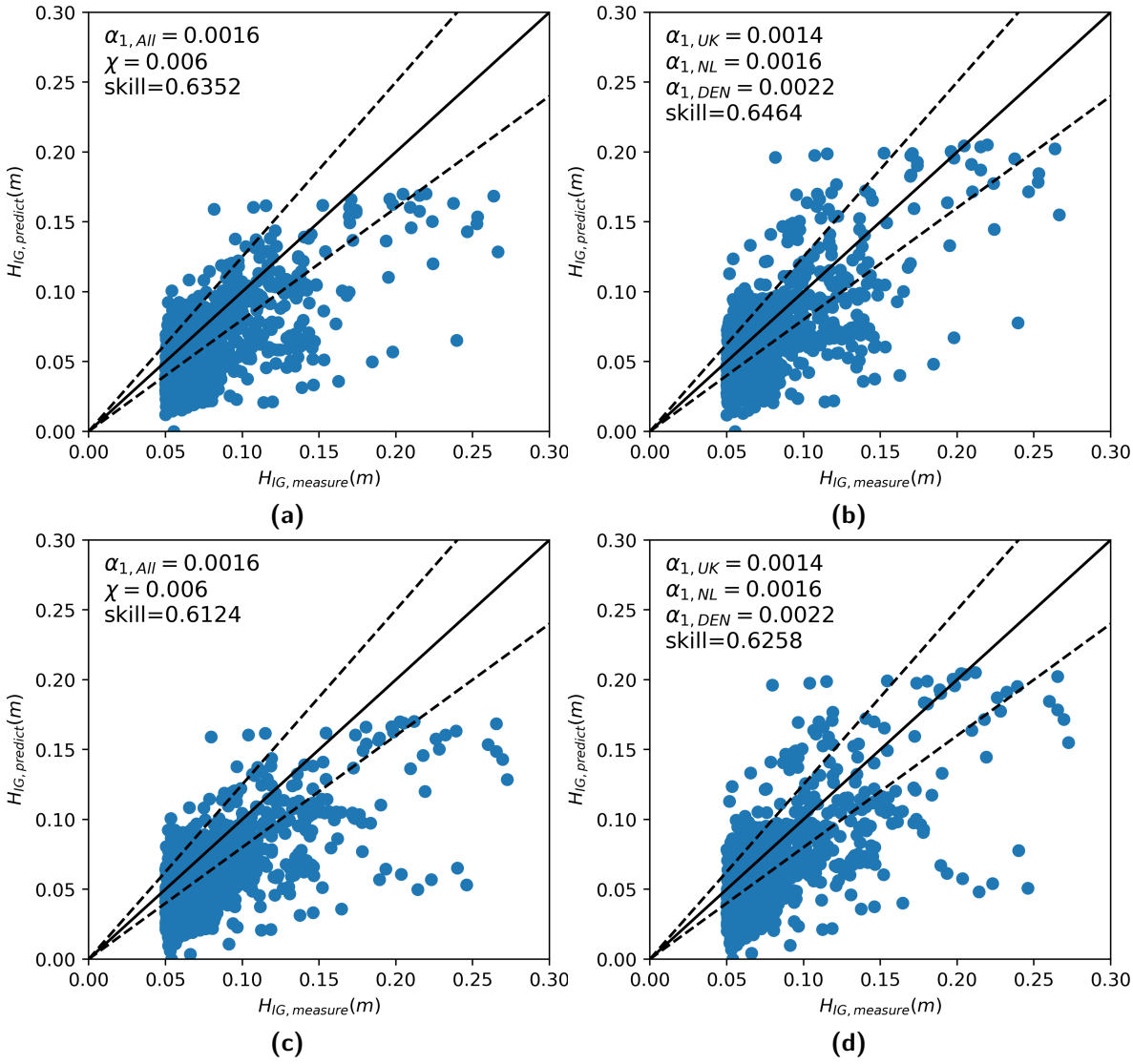

Figure 5-4: Scatter plot of the instantaneous modelled ($H_{IG,predict}$) versus measured ($H_{IG,measure}$) free IG wave height using data from station A12, Q1 and EUR for all 10 considered storm events using different bound IG sources. The top plots (panel a-b) use measured bound IG wave height from observation stations. The bottom plots (panel c-d) use WAM-estimated bound IG wave height to calculate the free IG wave height $H_{IG,measure}$. The left plots (a,c) shows the skill calculated using constant source calibration parameter $\alpha_{1,ALL}$ and friction parameter χ. The right plots (b,d) gives the result using varying α_1 and constant friction parameter $\chi = 0.01$.

Chapter 6

Origins of free infragravity waves

Based on the optimal combinations validated in the model, the origins of free infragravity waves in the North Sea and the dependence on the magnitude of observed free IG wave height is introduced here.

6-1 Origins and proportion of individual coastline

A spatial variation has been noted in the proportion of free IG components from the individual coastline. For different observation locations, the origins of free IG energy sources are represented in the pie chart, see figure 6-1. Based on this map, a general contribution from the source coastline and the corresponding proportion can be examined. DEN (blue), NL (orange), and NL (green) is the main contributor at each station and each has different dominate domain. DEN and NL dominate in the south of the North Sea and along Dutch coastlines respectively. Energy from UK explains the part of free IG components at different locations with a slightly smaller contribution. Comparing to the three main generation regions, NOR, BE and GER can be negligible in radiating free IG waves to the south of the North Sea based on current observation data. The table 6-1 specifies the exact values of the ratio between free IG wave height from the individual coastline and observed IG variance.

Station	UK	BE	NL	GER	DEN	NOR
A12	0.1412	0.0062	0.067	0.0664	0.6818	0.0376
Q1	0.1646	0.0268	0.563	0.0307	0.1982	0.0163
EUR	0.1625	0.0173	0.4873	0.1230	0.1844	0.0254
D15	0.2667	0.0100	0.2018	0.0749	0.4036	0.0426
F16	0.1643	0.0164	0.297	0.1182	0.3815	0.0227
IJM	0.0853	0.0239	0.7811	0.0145	0.0882	0.0077
LG	0.1487	0.0642	0.5273	0.0187	0.2212	0.0231

Table 6-1: Mean percentage of free IG wave energy level from each coastline

6-2 Dependence on infragravity wave height

Apart from observation location, the contribution of radiated free IG waves varies according to the characteristics of storms. It has been observed that the proportion of free IG components in the total IG variance is largely related to the significant SS wave height during storm events (see figure 4 in the paper [51]). In this section, the free IG energy from major contributing coastlines (DEN, NL, and UK) is analyzed as a function of the total IG variance due to the temporal varying contribution of each coastline during storm events. Three stations represent the different observation regions with A12 in the center of the southern North Sea, Q1 in the south of the Dutch coast, and EUR adjacent to the north of the Dutch coast.

At station A12, DEN accounts for the highest contribution to the total IG wave with a median value of around 75% (see figure 6-2a). The IG energy level from other coastlines is far beneath the one from DEN. It is noticed that UK has a large number of outliers out of the 25 to 75 percentiles range. The reason can be the growth of IG energy from UK that always occurs at the tail of the storm. With time deference, a small excitation of IG wave occurs at UK with an overall decrease in total IG wave height. Free IG wave takes time to travel from DEN to UK across the North Sea. NL accounts for a marginal contribution to the open sea which can be negligible. Combined with a strong radiation from NL coastlines observed in Q1 and EUR, the low energy level from NL at A12 can be attributed to three possible reasons. The first one is due to the location of A12 that is exposed directly to the waves from DEN coastline while NL faces the southern UK coastlines. Another reason can be the limitation of storm events with restricted number and magnitude of incident sea-swell waves generated along NL coastlines and lower radiation IG wave energy level from NL can reach the A12. In addition, the extreme storm (Xaver with $H_{SS} = 11m$) is found to hit the DEN coastline and the only storm causing excitation of sea-swell waves mainly at NL coastline is Christiaan ($H_{SS} = 6m$). The produced radiated free IG waves of a minor energy level are attenuated before they can impact the IG conditions at A12.

Next, we can have a look at the contribution of individual coasts at A12. For DEN (see figure 6-2b), the median proportion of the free IG waves to the total IG variance shows an increasing trend basically following the burst of IG wave height. However, for the case $15cm < H_{IG,total} < 20cm$ (representing the peak of the IG energy bursts), the contribution of DEN decreases slightly. A possible explanation is that the decreased contribution of free IG waves of DEN at higher total IG wave levels results from the increasing occurrence of forced bound IG components under energetic sea-swell motions [51]. Another assumption is due to

the restricted number of extreme storms of which Xaver is the only one with an observed free IG wave height over 20cm. NL accounts for very limited free IG energy to A12 independent of the variability of observed IG waves. The increasing contribution from UK is accompanied by a decrease in observed free IG wave height especially in outliers as an accidental contribution from occasional storms.

Station Q1 and EUR are dominated by energy from NL with a median proportion of 60% and 55%, respectively, in all IG variance. DEN and UK account for the remaining part of energy combined with the insignificant contribution from GER, NOR, and BE. Focusing on the contribution of DEN at Q1 and EUR (see figure 6-2f and 6-2j), there is an increasing free IG component in the IG wave height bin between 10 cm and 15 cm at Q1 while no energy radiating from DEN can reach the location of EUR with a higher total IG variance, indicating a larger radiation energy origins from the north of Dutch coastline at IJM and Q1 (see figure A-15i) compared to LG and EUR (see figure A-15m). In addition, UK accounts for the second major contribution at D15 (see figure A-15a), showing a relatively strong radiation capability to the open sea. However, based on the comparison between D15 and distant locations such as A12 and F16 (see figure A-15e), the decreasing contribution from UK could be caused by the dissipation by bottom friction or the limited magnitude of our studied storms.

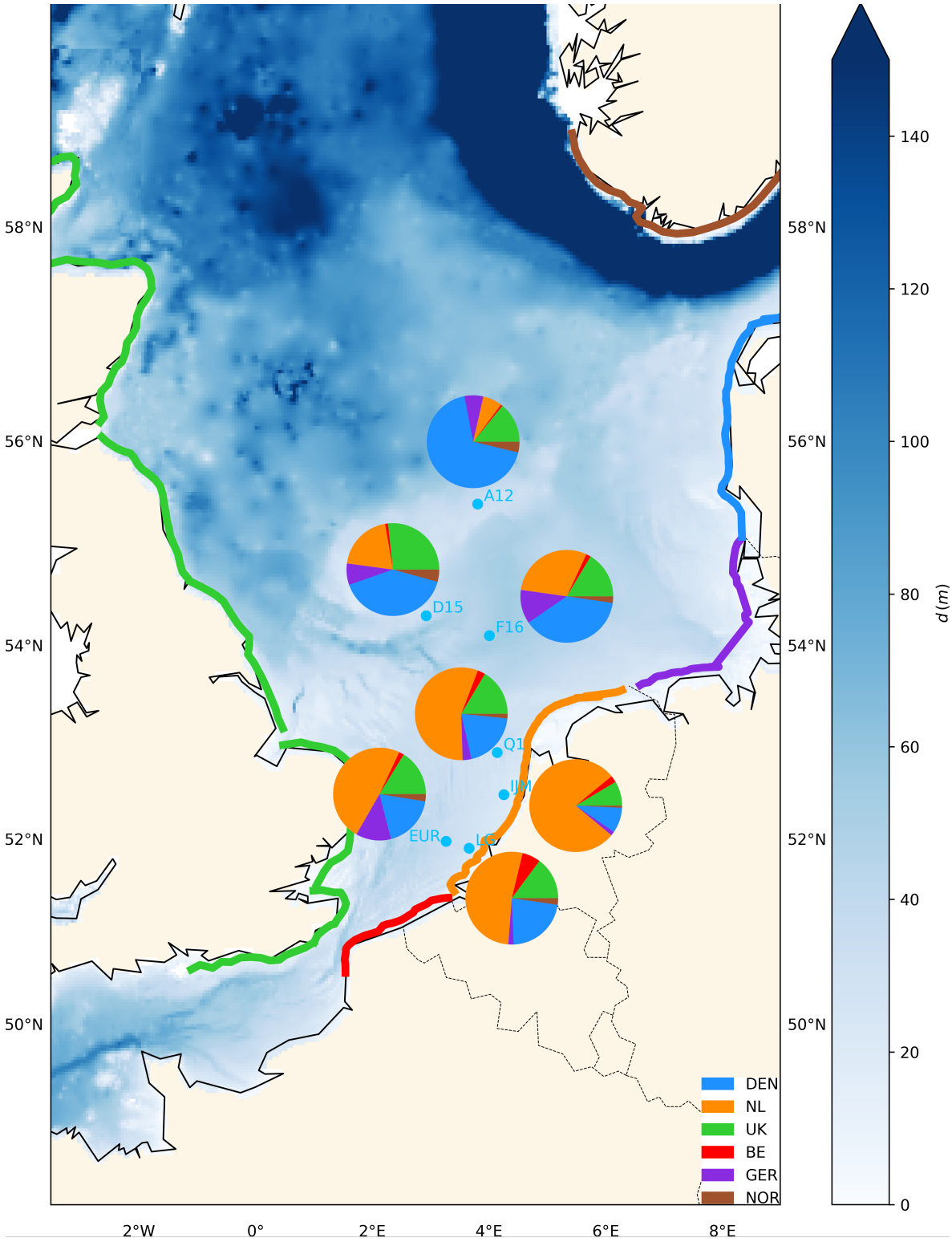

Figure 6-1: The pie charts show the origins of free IG wave energy observed at A12, D15, F16, Q1, IJM, EUR, and LG. The corresponding proportion is given in table 6-1. Different sources of free IG waves are indicated with different colors consistent with the color of source coastlines bordering the North Sea. The source coastline is labelled by the legend.

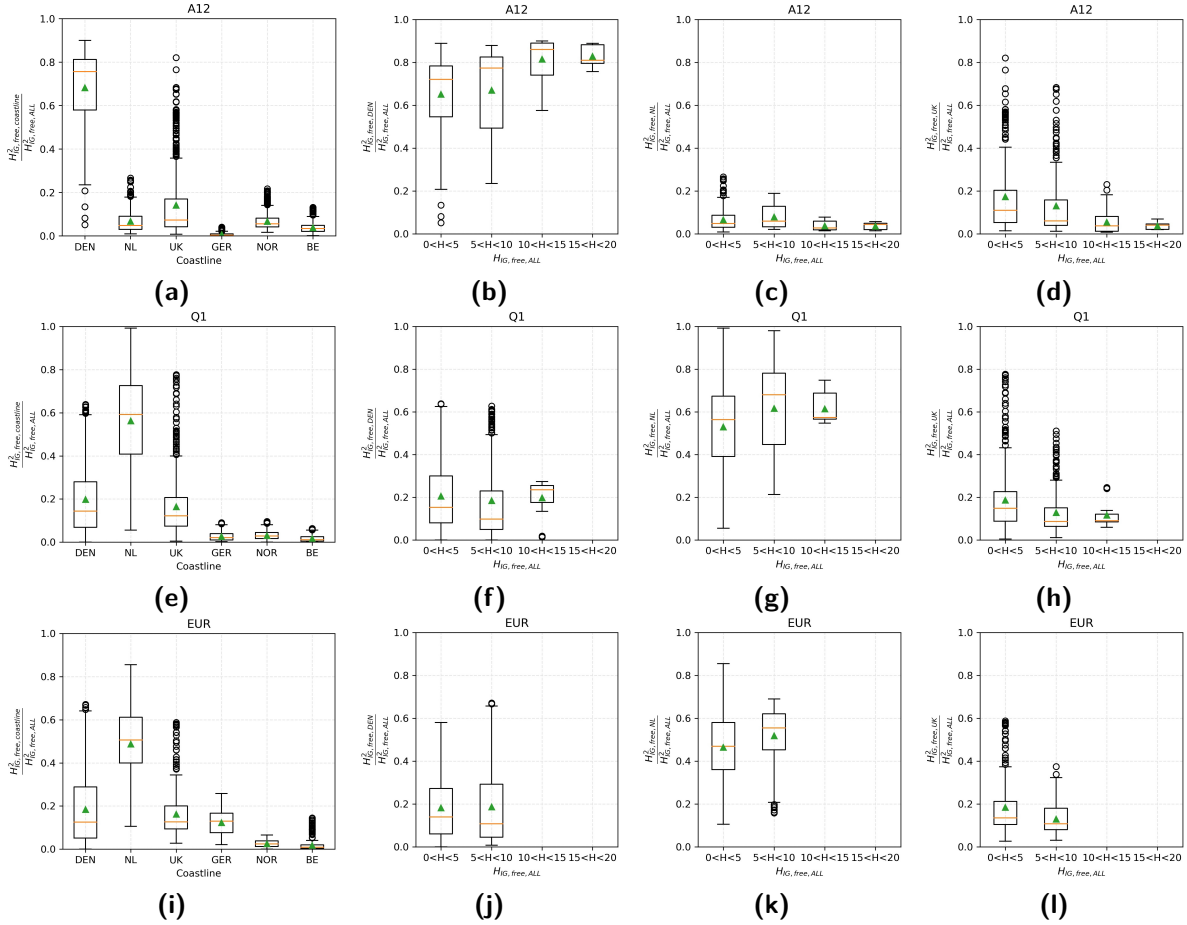

Figure 6-2: (a,e,i): Box-whisker plots of the contribution of the free IG waves from different coastlines at A12, Q1 and EUR respectively. Others: Box-whisker plots of the contribution of the free IG waves from DEN coastline (b,f,j), NL coastline (c,g,k) and UK coastline (d,h,l) to the total IG variance as a function of the binned IG wave height at A12, Q1 and EUR, respectively. The box includes the 25 to 75 percentiles with the median in red. Outliers are given by the black circle signs. Medians and mean values are marked by orange line and green triangular symbols, respectively.

Chapter 7

Discussion, conclusions and recommendations

7-1 Discussion

In this study, the simplified physical process contained in the model helps us to focus on the propagation pattern of free IG wave. This decreases the skill of the model and brings out the limitations of our simulations. The discrepancies between model results and measured data could be attributed to both measurement inaccuracies and modelling inaccuracies.

7-1-1 Measurement limitations

Two sources of bound wave estimates: measured and WAM-estimated bound wave

Using different bound wave origins has a slight difference of the skill results comparing figure 5-4a, 5-4b and 5-4c, 5-4d. For both combinations (the first one: $\alpha_1 = 0.0016\,s^{-1}$, $\chi = 0.006\,m^2s^{-3}$; the second one: $\alpha_{1,UK} = 0.0014\,s^{-1}$, $\alpha_{1,NL} = 0.0016\,s^{-1}$, $\alpha_{1,DEN} = 0.0022\,s^{-1}$, $\chi = 0.010\,m^2s^{-3}$), the results using WAM-estimated bound IG data shows a lower skill value. In general, WAM-estimated bound IG wave fits well with the measured one while sometimes at peak of the storm there exists a mismatch. In our study, model skill using different source of bound IG waves is compared at A12, Q1 and EUR, showing a slightly lower match in free IG wave height when WAM-estimated data is used.

Restricted frequency band of IG measurements (0.005-0.01 Hz only)

One major concern is the experimental limitations in measurement of IG wave. The available data only covers a subset of full IG frequency band (0.005 - 0.01Hz). The missing of a higher frequency band of IG waves underestimate the total energy of the IG band (0.005 - 0.05Hz). SWAN handles the simulation in the full IG wave range, the output of which is restricted

between the available measured range. A low frequency part of IG wave is capable of being reflected at both relatively steep and milder beach slopes [24] [14] [34]. Compared to the higher frequency, the radiation IG wave energy within current partial IG wave band is less dependent on the coastal bathymetry [53].

Additionally, the two sources of bound IG wave at different observation sites affect the assessment for the simulation capability of SWAN since there is no available measured data at some stations. It is noted though the measured bound IG wave height $H_{IG,bound,MES}$ and WAM-estimated bound IG wave height $H_{IG,bound,WAM}$ are similar under most circumstances, see figure 7-1. While sometimes the measured one would show a large difference compared to the WAM one especially at peak of the storm. It is difficult to judge whether the sudden peak of the storm height is a noise or an actual value, which produces uncertainties in our skill calculation. Thus it is also necessary to assess the fit between measurement and prediction visually to determine the optimum results.

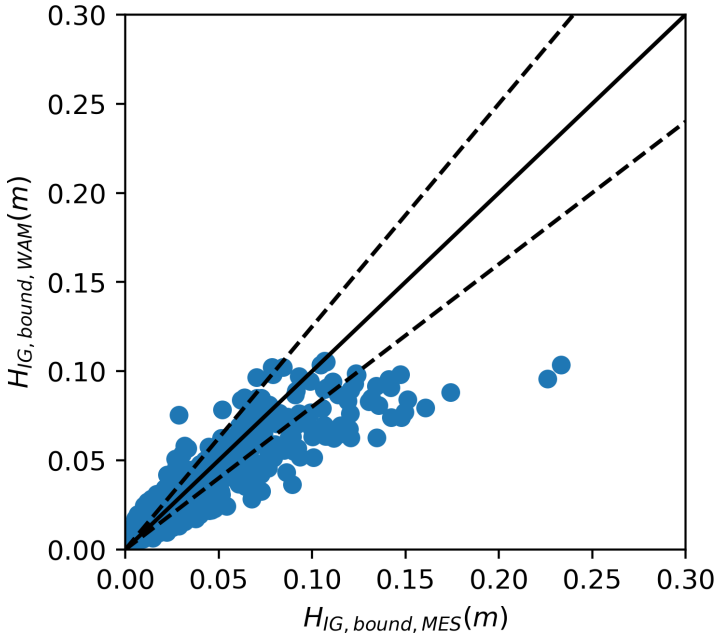

Figure 7-1: Comparison of different source of $H_{IG,bound}$

Base level of IG away from storm events

Though we give attention to the propagation of free IG wave during the extreme period of storm events. But the IG energy level present prior to and after the peak of storm are observed. It gives us two choices to calculate the skill using the predicted data during specific period.

To eliminate the effects from the "base level" of free IG wave, one way is to calculate the skill for only part of the storm when IG wave height exceeds a threshold. A small increase on the skill can be expected estimating the match between measured and modeled results. With regard to the study on distribution of the origins of IG energy level, the entire storm period is considered because of the dominant impacts from English coastline at the tail of the storm.

In addition, SWAN fails to capture the existence of base level out of the storm periods due to the unknown physics. A hypothesis is that this part of small IG wave energy level comes from the radiation IG wave during previous storm period. In this study, the application of varying α_1 and χ focus on the extreme periods. During extreme storm period, our assumption that free IG wave energy accounts for the major contribution in IG band works properly and the appropriate combination is sufficient to ignore the small impacts from base level. While for a mild storm period, the exclusion of the addition of base level could prompt the over prediction of source term α_1. Using an average value of base level might compensate for the impacts from this part of energy difference.

7-1-2 Modelling limitations

Source term

The parameterization of source IG term in the modeling of radiation free IG wave is based on the local equlibrium between incident SS wave forcing and the bound IG wave [27]. During a storm event, large amounts of sea swell waves are generated incident to the shorelines. The directionally incident bulk waves reaching shorelines is assumed to derive the radiation free IG wave, which brings out the two problems. The free IG wave energy level not caused by the object storm is ignored. It has been observed the radiation free IG wave generated at one coast could travel a long distance and arrive at another coast, in which case the source IG wave energy applied in modelling is underestimated. Another problems is associated with the process of energy transfer between sea swell waves and IG waves, and the process of wave propagation including the release of bound IG waves and reflection of free IG wave. It takes time and distance for waves to travel across the surf zone and accomplish the energy transfer. Thus our assumption overestimates the radiation IG energy level in this aspect.

Friction coefficient

Bottom friction is of minor importance to the evolution of wave in oceanic waters, while it can play an important role in dissipation over long distances. The wave energy dissipation depends on the wave field and on characteristics of the bottom. Hasselmann et al. (1973) represented the friction impacts using parameter χ based on the observation of swell [28]. The actual bottom dissipation is complicated and depends on the large variations in bottom conditions for instance bottom material, dynamic bottom shape related to wave motions and ripples [77]. To simplify this, a constant χ value is applied in the model. This experimental parameter is developed from numerous JONSWAP parametric spectral shapes focusing on swell waves instead of IG waves, resulting in the inaccuracies of the friction coefficient value.

IG wave generation regions

The generation regions of free IG wave spread over the North Sea is divided by nations. The original IG energy level from coastline is related to the bottom slope, type of beaches and nearshore topography. The rough division of the IG wave origins ignores the interior diversity. The generation IG energy level varies spatially and temporally per storm and each storm has

different characteristics. For instance, UK coastline cover a relative large distance from north to south and is considered as a whole region to radiate free IG wave while only the south of UK matters in most cases. NOR regions with steep and irregular coastlines along Norwegian Trench which hinders the generation of IG wave.

Other generation mechanisms

The sources of IG waves radiated from coastlines cannot explain all the energy level observed in the open sea. Our study on the origins of free IG wave reveals that other generation mechanisms could also play a role in the energy level in IG band.

When encountering a region shallow water on the North Sea such as the Dogger Bank, the bulk short waves experience shoaling and a part of free IG wave could be released in addition to the proportion radiated from distant coastlines. The free IG wave pattern under storm Xaver shows the a concentration of free IG wave close to the A12 can be found in figure 7-2a, figure 7-2b and figure 7-2c.

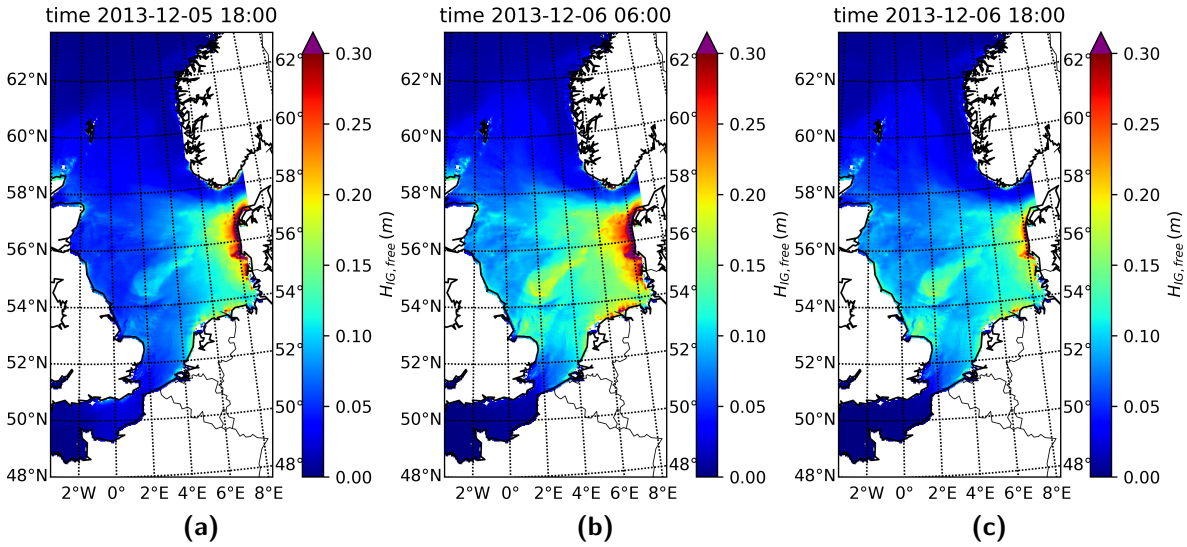

Figure 7-2: The free IG wave pattern on the North Sea during storm Xaver

Other possible generation mechanism could be wind gusts or the radiated free IG wave out of the interested period or coming from other coastlines [51].

7-2 Conclusions

Infragravity waves play an important role in nearshore regions, having an impact on the coastal safety. To understand its propagation patterns and driving mechanisms in the North Sea, we use SWAN to model the evolution of radiation free IG waves from coastlines over the open sea during 10 severe storm events (with $H_{SS,max}$ ranging from 6m to 11m). Bottom friction is accounted for in the model to inspect the IG wave attenuation with a friction parameter χ from JONSWAP experiments. The source IG term in the model is implemented

based on the parameterization for the SS wave parameters with a calibration parameter α_1. Different combination of α_1 and χ in the simulations give a specific picture of the dependence of free IG wave pattern.

The predicted data with optimum combination can give a relatively good match to the measured data. In general, SWAN can explain the appearance of total IG wave height with an accuracy up to 78% during storm events. It indicates that SWAN is capable of describing the prominent IG generation mechanism contributing to the excitation of observed IG wave during storm events in the North Sea.

The approach for the source radiation IG term is highly empirical since the source IG term is assumed isotropic at a location seaward of the surf zone due to the lack of directional distribution of radiated IG free waves. The broad distribution spreading to all directions could lead to a loss of radiated free IG wave energy. The part of the source IG waves incident to the shoreline vanish in the model, and the part propagate offshore is likely to experience a stronger trapping close to the surf zone compared to a narrower distribution.

Additional research questions are answered here.

The comparison between WAM and MES data

Comparing the measured bound IG wave and WAM-estimated bound IG wave shows a convincing result in general. Occasionally at the peak of a storm the measured bound IG wave height would exceed the estimated one (see figure 7-1). In mild IG wave conditions ($H_{IG} < 0.15m$) with a small measured bound IG height, WAM-estimated wave height can be a sound replacement to measured data. However, under energetic sea-swell waves, the error caused by WAM-estimated data can be nonnegligible which requires a critical look at the estimated bound parameters.

The contribution from free, bound waves to the total IG wave signal in the North Sea

During the storm peak, the bound IG wave largely generated based on the local equilibrium between SS wave spectrum and bound IG wave. A sudden increase of bound IG wave height can be observed around the peak, and the bound fraction has a minor contribution to the total IG wave height out of the peak period. The proportion of bound and free components in IG variance is associated with the magnitude of sea-swell waves (as observed in paper [51]) and large bound IG contributions can be expected under an energetic short wave conditions during storm events.

Impacts on the generation of free IG wave

The scale of the storm including storm track and storm magnitude influences the generation of the free IG wave most. The source IG wave is implemented based on the empirical relationship with incident SS wave spectrum. The magnitude of SS significant height and wave period affects the corresponding wave height of free IG. For storm Xaver, the maximum SS wave height $11\,m$ could result in a maximum free IG wave height around $25\,cm$. For a smaller storm for instance Christiaan, a maximum SS wave height of $6.3\,m$ corresponds to a maximum free

IG wave height of $8\,cm$. On top of the storm magnitude, different geographic features also play a role in the shoaling and reflection of free IG wave close to the coastline. Though NOR is exposed to the storm but few storm surges can induce the concentration of IG wave along the Norway coastlines due to the existence of Norwegian Trench.

Impacts of bottom friction on the propagation of free IG wave

The impacts of bottom friction on the propagation of free IG wave is explored based on the simulation results from SWAN model. Excluding bottom friction, the dominant source coastline remain unchanged at A12, indicating the dissipation of bottom friction to the free IG wave from Dutch coastline to A12 is not the main factor preventing the release of free IG wave from nearshore regions to the open sea. For the stations close to NL, it is noted the simulation with bottom friction dissipates the energy from DEN to the location of A12, which improves the fit between measured and predicted one.

The simulation of SWAN model on the propagation of free IG wave in the North Sea shelf

The propagation of free IG wave after reflection towards the open sea is our main concerns. The extreme storm events can substantially promote the burst of bound IG wave, facilitating our observations on amplification of free IG wave signals as well. Bottom friction are excluded first and then included to inspect the origin of measured free IG wave and the distribution. Through varying the calibration parameter of source IG wave and friction coefficient during 2 storm periods Xaver and Friedhelm, we can calibrate the model aiming to find out the optimum combination. Then the propagation pattern of free IG wave during different storm periods are looked into with a view to the validity of the model.

Although for different measuring stations the performance of SWAN varies. The prevalence of the underprediction before the storm peak at A12 (also D15 and F16) cannot be captured, denoting the deficiency of our physical understanding. while for other stations, it gives a reliable estimation during severe or moderate storm period in terms of the free IG wave. The undulation of free IG wave around the peak of the storm can be captured pretty well. Regarding a small storm or a calm climate event, there is always a difference between the measured and predicted IG wave height. The origin of the background IG level observed in the North Sea is unclear and requires more information to be verified.

In addition, the modelled wave period and propagation speed is inspected based on the hypothesis that the source IG energy radiating along shorelines is isotropic over all directions and frequencies in the range of 0.005 - 0.01Hz. The mean wave period T_{m0} is around $130.8s$. The depth of observation locations is ranged from $18m$ to $47m$, the propagation velocity of free IG waves in very shallow water varies from $14m/s$ to $22m/s$ correspondingly in terms of the modelled process. The unavailability of measured wave period of IG wave unable us to verify the agreement with measured wave speed.

The source of IG waves incident to the Dutch coast

When the storm passed by or directly hits the Dutch coastlines, the energy level of bound IG wave increase appreciably inducing the large release of free IG wave height as well. Without bottom friction, the DEN dominated storm radiates free IG wave and is able to diffuse all over the North Sea. Part of the energy from the DEN can be detected in Q1 as well with a small time difference in respect of the peak of separate coastline time series. Including bottom friction largely dissipate the free IG wave energy during propagation. The significant maginitude of free IG wave height observed at the previous storm peak has a marginal response out of storm period. In addition to the bound IG wave, there is one notable source of IG waves incident to the Dutch coast namely the release of bound IG wave induced by storm. Also the radiated free IG wave energy from DEN and UK can be observed as the second contribution.

Contribution of the radiated free IG to the total measured energy

Different coastlines dominate at different stations concerning the location of the stations and bathymetric changes surrounding. DEN always contribute most free IG wave energy to the total IG energy at A12. Ignoring the mismatch before the peak of the storm, it shows a 75% reliability to account for the measured energy from distant coastlines. For the storms with a distinct time difference before peak at A12, the peak time of predicted free IG energy from DEN deviates from the peak time of measured bound IG energy. It denotes that at A12, the radiation free IG wave cannot fully explain the measured energy in the open sea. The peak of measured free IG wave always follow those of total one and matches well with those of bound IG wave, it is assumed that there should be a source of free IG energy directly related to the storm instead of the radiation portion from distant coastlines.

Contribution of each coastline bordering the North Sea

DEN is the most influential coastline distributing free IG energy in the North Sea. DEN dominate at A12 and the free IG wave originating from DEN can be identified at all the other available observation stations in a nonnegligible level. The major contributor is NL standing in the locations close to NL especially at IJM. The major part of free IG energy detected in the open sea at A12, D15 and F16 is constituted by the energy from DEN in each storm even though F16 is closer to NL in most instances. Only when NL dominates during the storm period for instance storm Christiaan it accounts for the largest portion of the origin of free IG wave.

7-3 Recommendations

In the process of the calibration, the impact of calibration parameter α_1 and friction coefficient χ are inspected. A correlation between the two variables is observed. A large source energy combined with a large friction coefficient could give a reasonable prediction for the generation and propagation of free IG wave in the North Sea and vice versa. Our original goal is to find an optimum combination of these two variables using the approach of Ardhuin et. al., (2014)

to validate the SWAN model. It proves that this exploration direction into the validation is not sufficient to give a very satisfying explanation. However, if a more detailed correlation between these two variables are concerned, from the user point of view the relationship can be formulated via the least square method. As a result, users can specify only one variable and the other one can be computed correspondingly.

More measurement data including the spectral shape of IG wave are required to gain further insight. To understand the amount of energy that is dissipated due to the bottom friction further, a comparison at several locations along the propagation track of free IG wave should be implemented. It is known that DEN is the main contributor to the free IG wave observed in the North Sea and could radiate IG energy to UK and NL. New measurement stations located close to DEN coastline and the south of UK coastline are required to inspect the track and the attenuation of free IG wave over the North Sea region.

In terms of the SWAN model, currently we only simulate the propagation of free IG wave offshore in the open sea and did not inspect the wave motions nearshore. However the free IG wave is mostly generated from nearshore regions during extreme storm events. Since our implemented source IG term is positioned at intermediate water depth around 20m. The incident wave transformation containing shoaling, breaking, refraction and trapping occurs nearshore calling for the detailed research in shallower water. Combined with a look into frequency and direction distribution of IG wave, a finer resolution of free IG wave from the nearshore regions can improve the accuracy of source IG term we imposed in this study since the physical processes of wave propagation nearshore especially refraction is highly frequency dependent.

In addition, the incident free IG waves vanish towards the shoreline in the model, and thus "re-refraction" mechanism cannot occur. However, it could lead to a loss in radiation free IG components since a concentration of free IG waves with sufficiently high energy levels can "bounce" horizontally in a bounded regional sea theoretically. This additional energy that origins from a different storm might explain the underprediction before the peak of the storm at the center of the southern North Sea which requires further verification based on the advanced model set in the nearshore region.

To investigate the origins of free IG waves in the North Sea, the coastlines bordering the North Sea are divided by countries and ignoring the variation along shorelines in bathymetry, bed slope which can have an impact on the wave interactions of sea-swell wave forcing. A detailed exploration in the local geometry changes deserves further research close to nearshore region relate to variables such as water depth, beach slope, relative angle between the shoreline and incident sea-swell waves influencing wave transformations and generation of trapped and leaky IG waves.

Chapter A

Figures and tables

This appendix shows the additional figures and tables in calibration and validation process of the model.

A-1 Calibration details

A-1-1 Calibration via varying the source calibration parameter for entire coastlines and friction coefficient

χ	Skill	$\alpha_{1,All}$												
		0.0012	0.0014	0.0016	0.0018	0.0020	0.0022	0.0024	0.0026	0.0028	0.0030	0.0032	0.0034	0.0036
0	1				0.7484									
	2			0.7602										
	3	0.7232												
	4			0.7225										
	5			0.777										
	6			0.7419										
0.01	1						0.752							
	2					0.7805								
	3			0.751										
	4					0.7332								
	5					0.7802								
	6					0.7581								
0.02	1									0.7568				
	2							0.7908						
	3					0.7641								
	4								0.7288					
	5								0.783					
	6							0.7614						
0.03	1													0.7576
	2								0.7989					
	3						0.7728							
	4										0.7131			
	5											0.7838		
	6									0.7508				

Table A-1: Skill of model from storm Xaver at each different station. Different types of skill are calculated. $1\tilde{6}$ represents A12, Q1, EUR, combined skill from 3 above stations, partial A12, and combined skill with partial A12, Q1 and EUR, respectively. The table shows how optimum skills develop along the increasing $\alpha_{1,All}$ and χ. Different colors in each cell represent different skill types. If we focus on the optimum skill at a certain station in the table in cells with same color, a diagonal line can be observed indicating a correlation between the two variables. It means if we improve both $\alpha_{1,All}$ and χ, the optimum skill for the combination along this diagonal line remains stable. As a result, many different combinations can provide a similar accuracy as the "optimum" one as long as we combine a proper variable to the other.

A-1-2 Calibration via varying the source calibration parameter for different coastlines with a constant friction coefficient

A supplement description of the constant α_1 for one part of the coastlines is given here. If we keep one variable for instance $\alpha_{1,UK}$ out of three constant and vary another one $\alpha_{1,NL}$, the optimum combined skill shows when $\alpha_{1,UK}$ is around 0.0014 with the highest probability.

χ	Skill	$\alpha_{1,All}$ 0.0012	0.0014	0.0016	0.0018	0.0020	0.0022	0.0024	0.0026	0.0028
0	1		0.5423							
	3	0.6559								
	4		0.5598							
	5	0.8042								
	6	0.5598								
0.01	1				0.5452					
	3				0.7306					
	4				0.5738					
	5		0.7924							
	6			0.7599						
0.02	1						0.5466			
	3						0.7705			
	4						0.5794			
	5				0.7981					
	6					0.7724				
0.03	1									0.5502
	3									0.7763
	4									0.5831
	5							0.7977		
	6							0.7817		

Table A-2: Skill of model from storm Friedhelm at each different station. Different types of skill are calculated. $1\tilde{6}$ represents A12, Q1, EUR, combined skill from 3 above stations, partial A12, and combined skill with partial A12, Q1 and EUR, respectively.

A-2 Validation details

A-2-1 Other storms

A-2-2 Origins of free infragravity wave dependent on the wave height at other stations

$\alpha_{1,UK}$	$\alpha_{1,NL}$	$\alpha_{1,DEN}$	skill
0.0014	0.0014	0.0022	0.7414
	0.0018	0.0022	0.7699
	0.0022	0.0018	0.7534
	0.0026	0.0018	0.707
0.0018	0.0014	0.0022	0.7447
	0.0018	0.0022	0.7651
	0.0022	0.0018	0.7473
	0.0026	0.0018	0.6964
0.0022	0.0014	0.0022	0.7442
	0.0018	0.0022	0.7555
	0.0022	0.0018	0.7366
	0.0026	0.0018	0.6814
0.0026	0.0014	0.0022	0.7381
	0.0018	0.0018	0.7411
	0.0022	0.0018	0.7206
	0.0026	0.0018	0.6619

Table A-3: The source of constant calibration parameter for UK $\alpha_{1,UK} = 0.0014$

$\alpha_{1,NL}$	$\alpha_{1,UK}$	$\alpha_{1,DEN}$	skill
0.0014	0.0014	0.0022	0.7414
	0.0018	0.0022	0.7447
	0.0022	0.0022	0.7442
	0.0026	0.0022	0.7381
0.0018	0.0014	0.0022	0.7699
	0.0018	0.0022	0.7651
	0.0022	0.0022	0.7555
	0.0026	0.0018	0.7411
0.0022	0.0014	0.0018	0.7534
	0.0018	0.0018	0.7473
	0.0022	0.0018	0.7366
	0.0026	0.0018	0.7206
0.0026	0.0014	0.0018	0.707
	0.0018	0.0018	0.6964
	0.0022	0.0018	0.6814
	0.0026	0.0018	0.6619

Table A-4: The source of constant calibration parameter for NL $\alpha_{1,NL} = 0.0018$

$\alpha_{1,DEN}$	$\alpha_{1,UK}$	$\alpha_{1,NL}$	skill
0.0014	0.0014	0.0022	0.7185
	0.0018	0.0022	0.7183
	0.0022	0.0022	0.7152
	0.0026	0.0018	0.7095
0.0018	0.0014	0.0022	0.7534
	0.0018	0.0018	0.751
	0.0022	0.0018	0.7488
	0.0026	0.0018	0.7411
0.0022	0.0014	0.0018	0.7699
	0.0018	0.0018	0.7651
	0.0022	0.0018	0.7555
	0.0026	0.0018	0.74
0.0026	0.0014	0.0018	0.7437
	0.0018	0.0018	0.7341
	0.0022	0.0014	0.7263
	0.0026	0.0014	0.7133

Table A-5: The source of constant calibration parameter for DEN $\alpha_{1,DEN} = 0.0022$

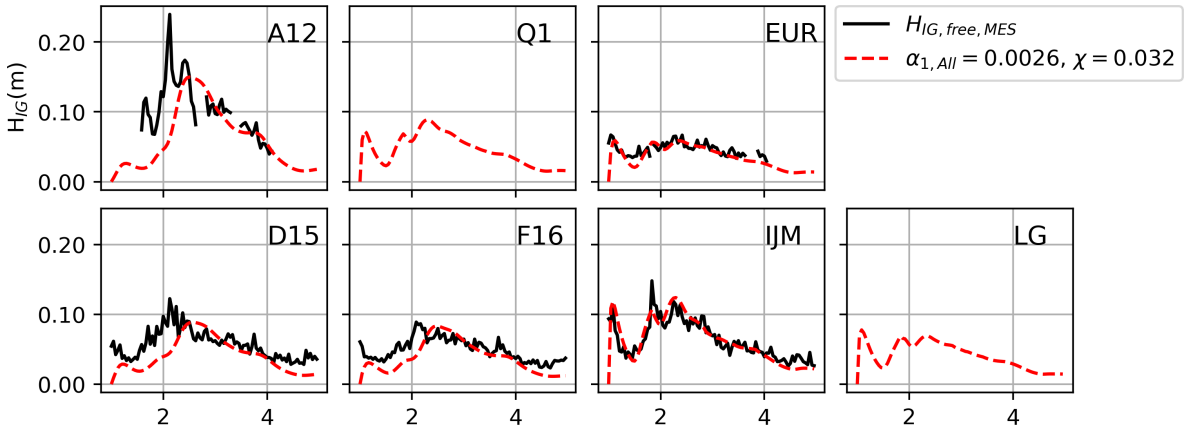

Figure A-1: Combination 1

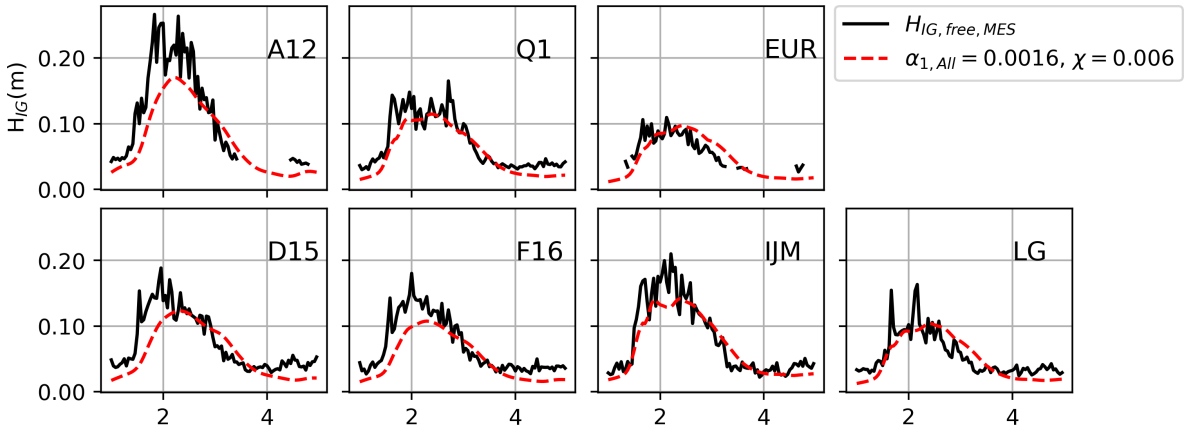

Figure A-2: Combination 2

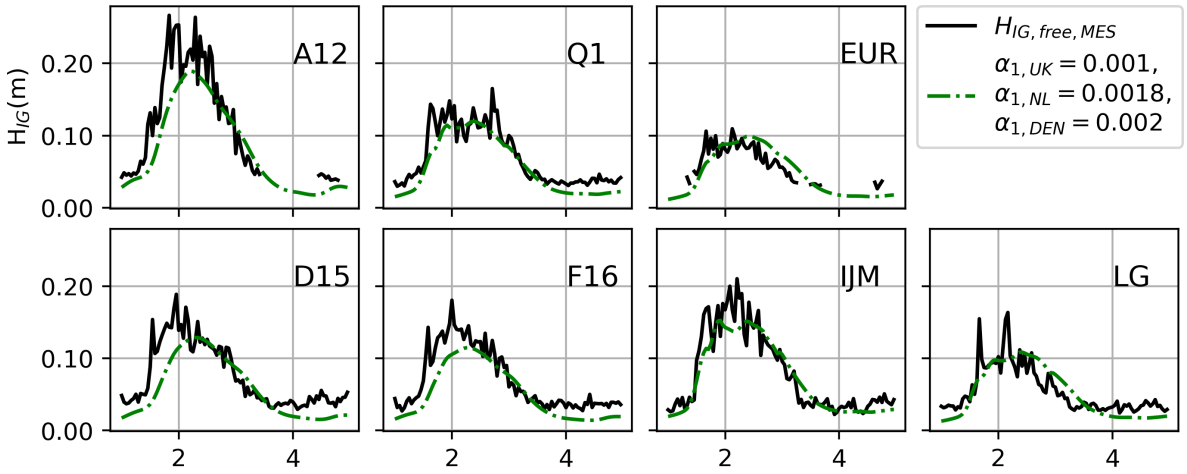

Figure A-3: Combination 3

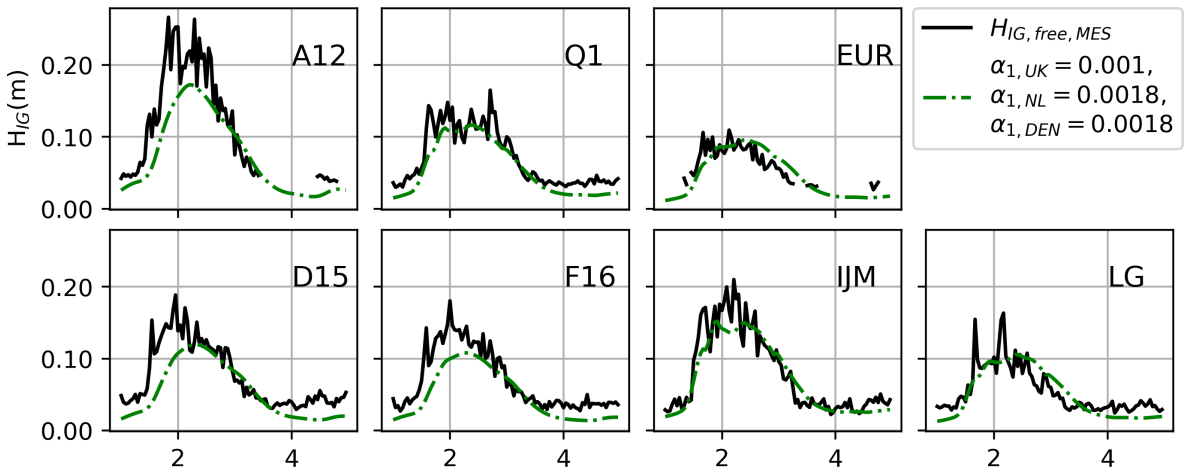

Figure A-4: Combination 4

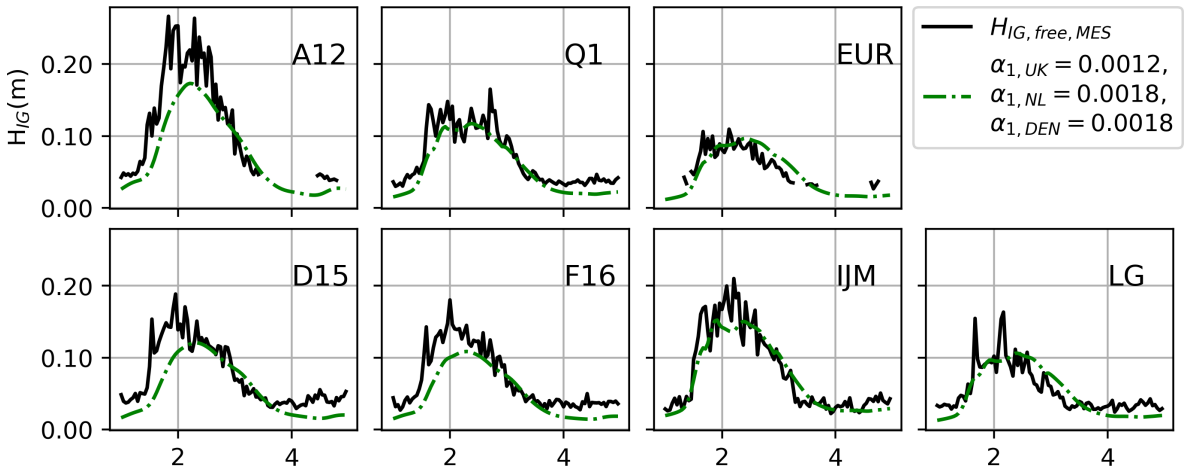

Figure A-5: Combination 5

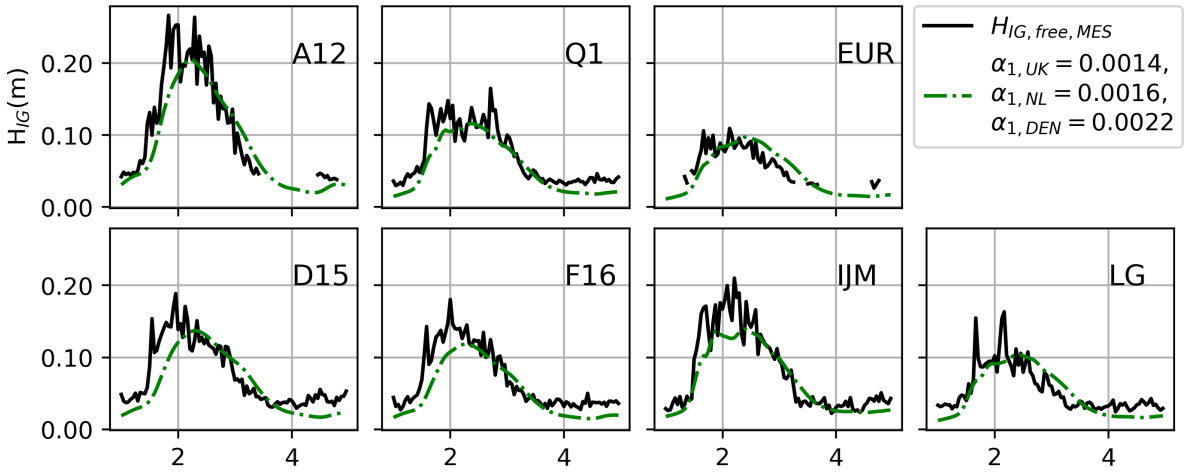

Figure A-6: Combination 6

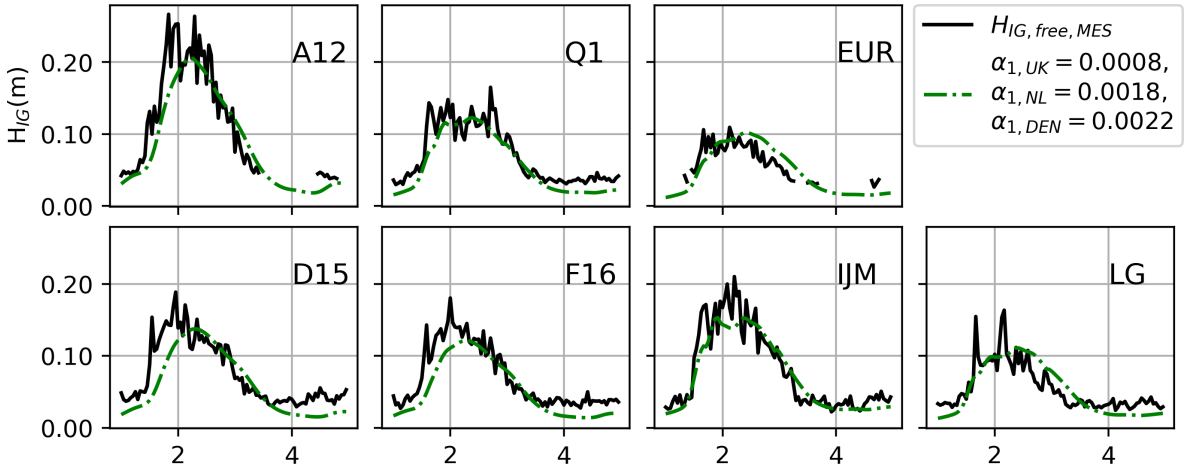

Figure A-7: Combination 7

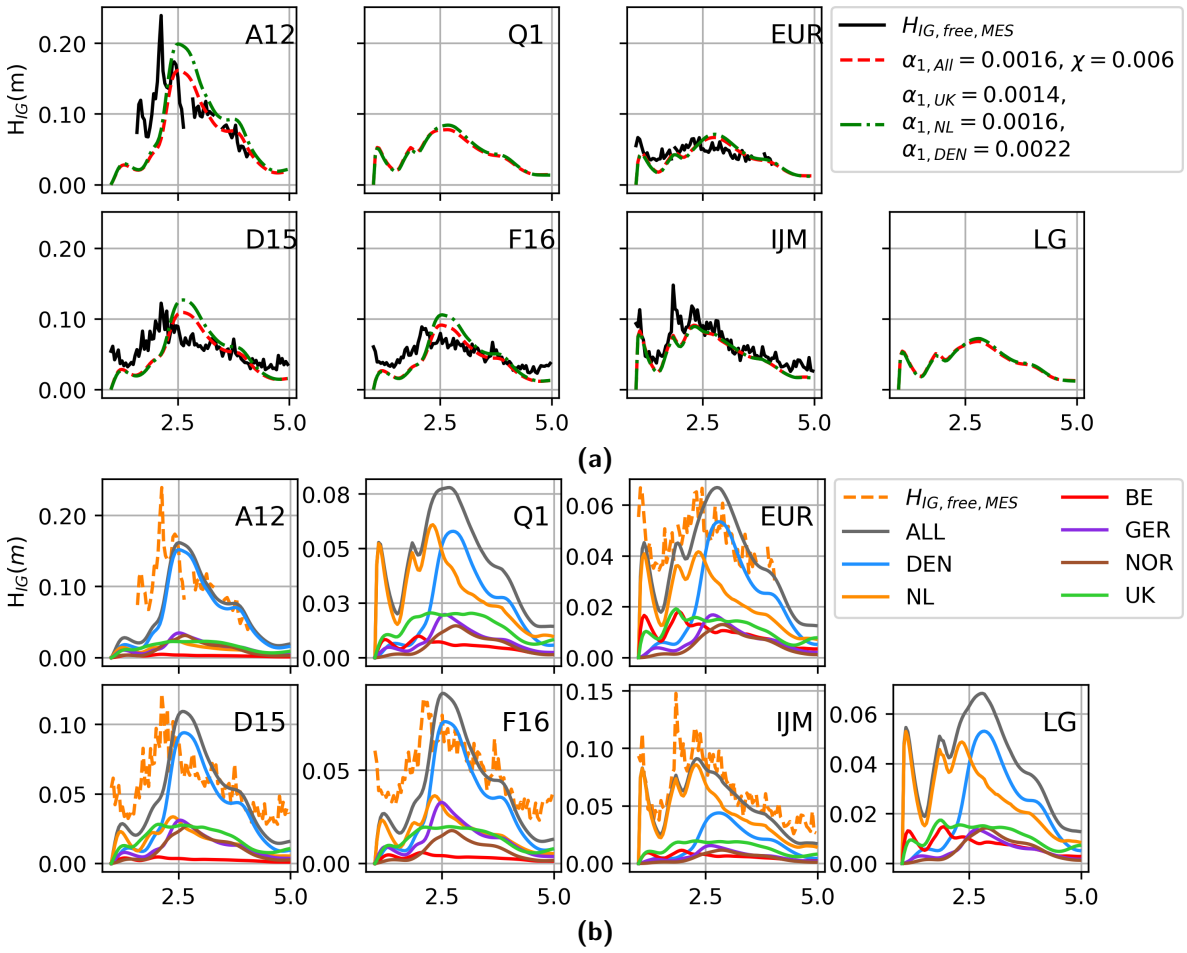

Figure A-8: The variation of H_{IG} at same scales with 2 combinations indicated in legend (a), and the contributions from individual coasts to observed free IG wave height at different scales (b) in 7 observation stations over storm Friedhelm.

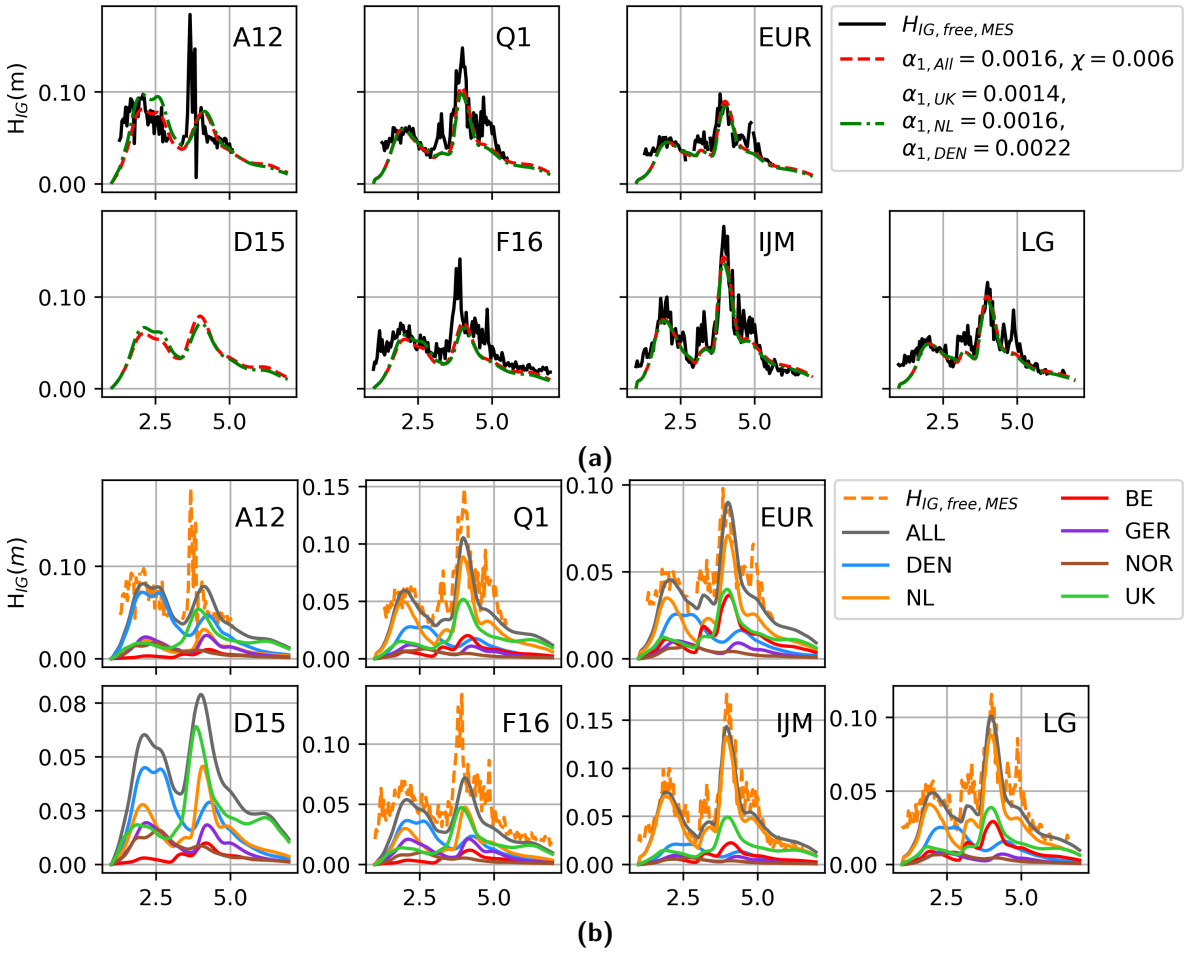

Figure A-9: The variation of H_{IG} at same scales with 2 combinations indicated in legend (a), and the contributions from individual coasts to observed free IG wave height at different scales (b) in 7 observation stations over storm Egon.

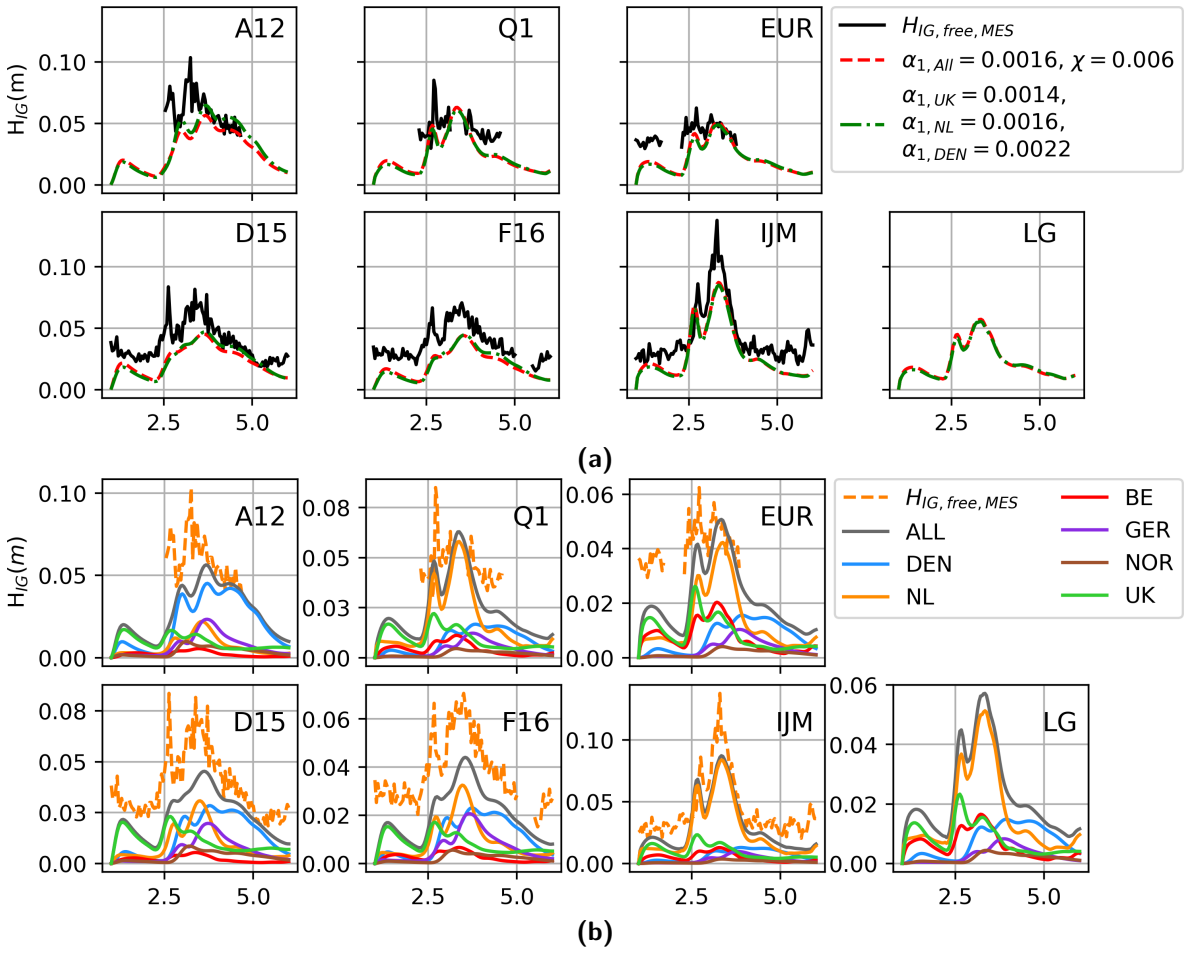

Figure A-10: The variation of H_{IG} at same scales with 2 combinations indicated in legend (a), and the contributions from individual coasts to observed free IG wave height at different scales (b) in 7 observation stations over storm Carmen.

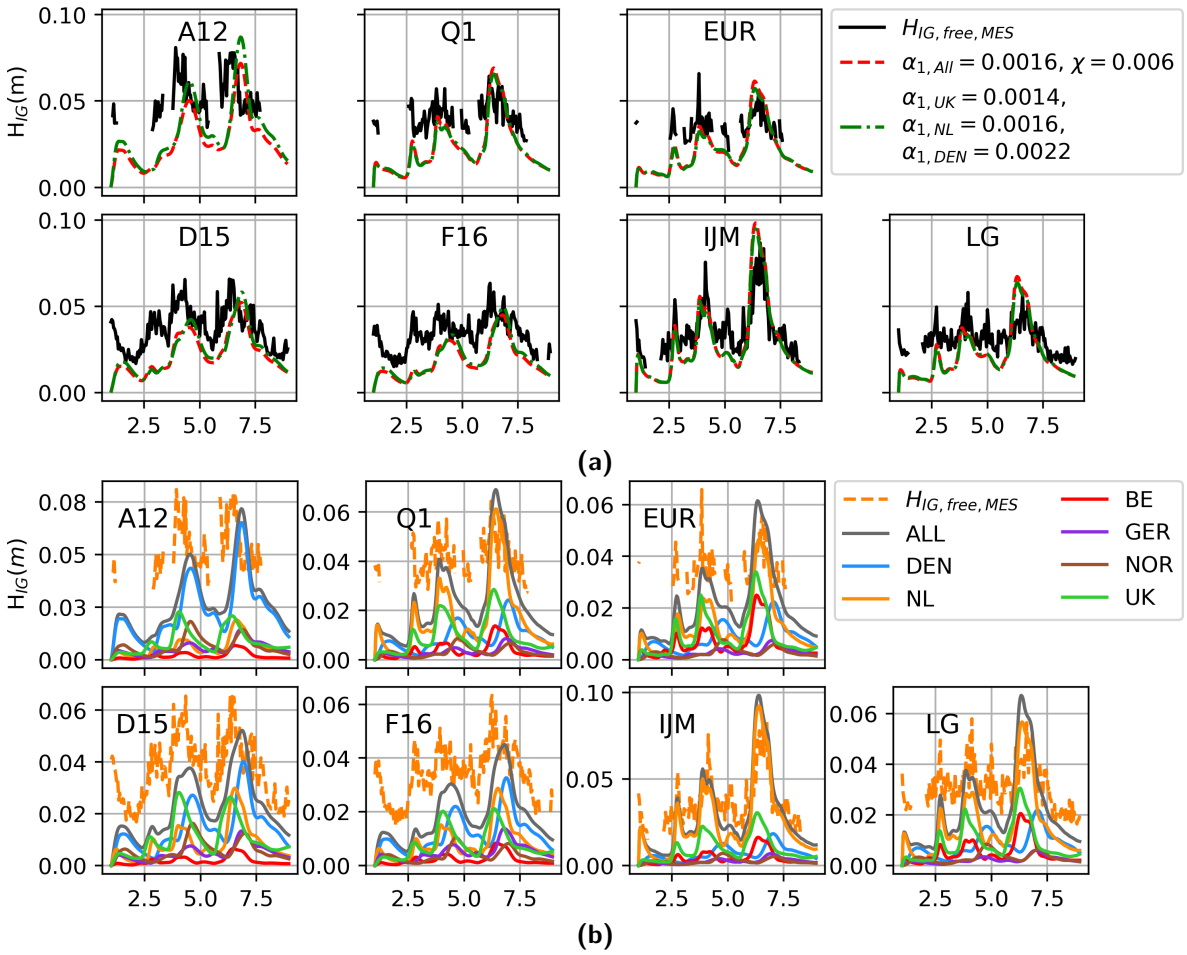

Figure A-11: The variation of H_{IG} at same scales with 2 combinations indicated in legend (a), and the contributions from individual coasts to observed free IG wave height at different scales (b) in 7 observation stations over storm Tini.

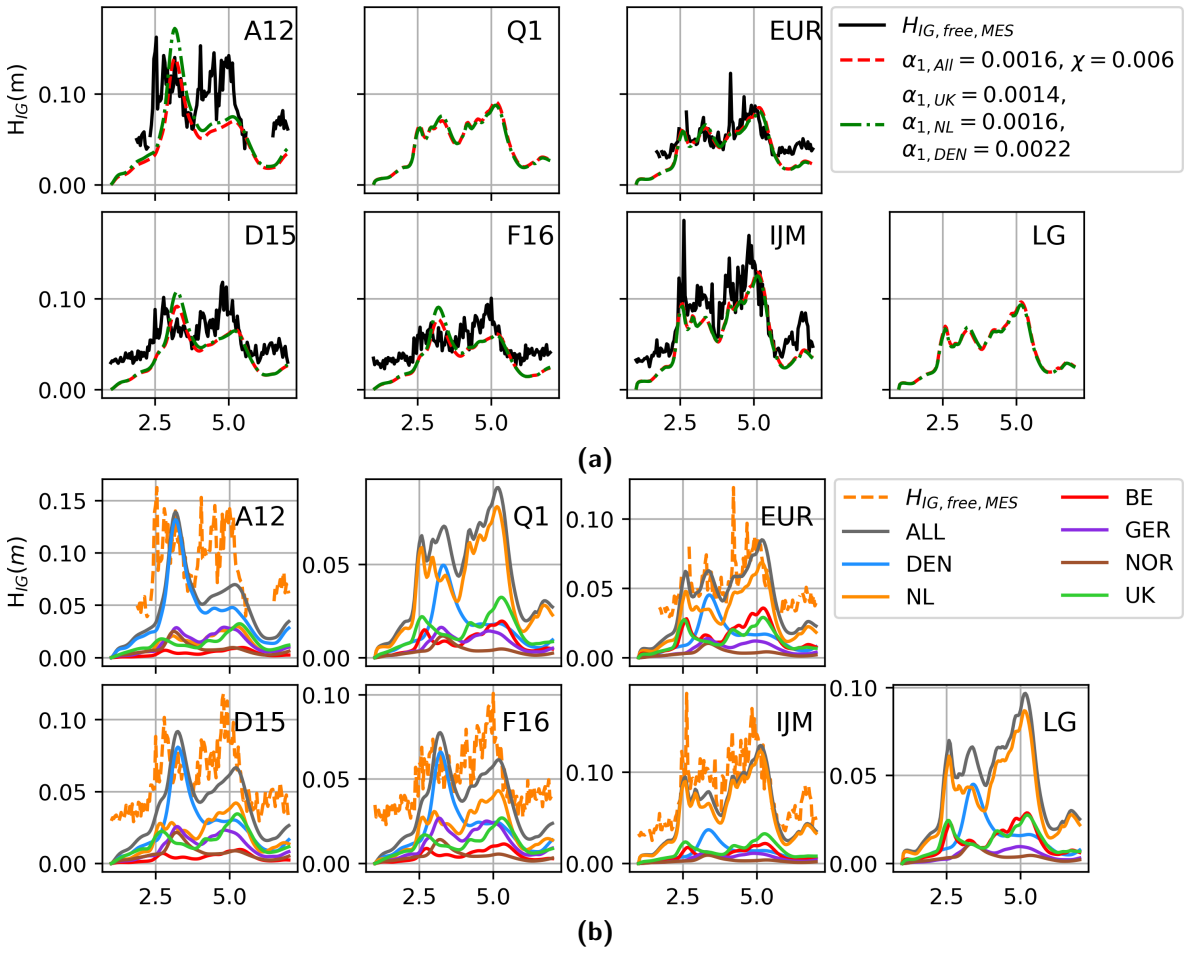

Figure A-12: The variation of H_{IG} at same scales with 2 combinations indicated in legend (a), and the contributions from individual coasts to observed free IG wave height at different scales (b) in 7 observation stations over storm Ulli.

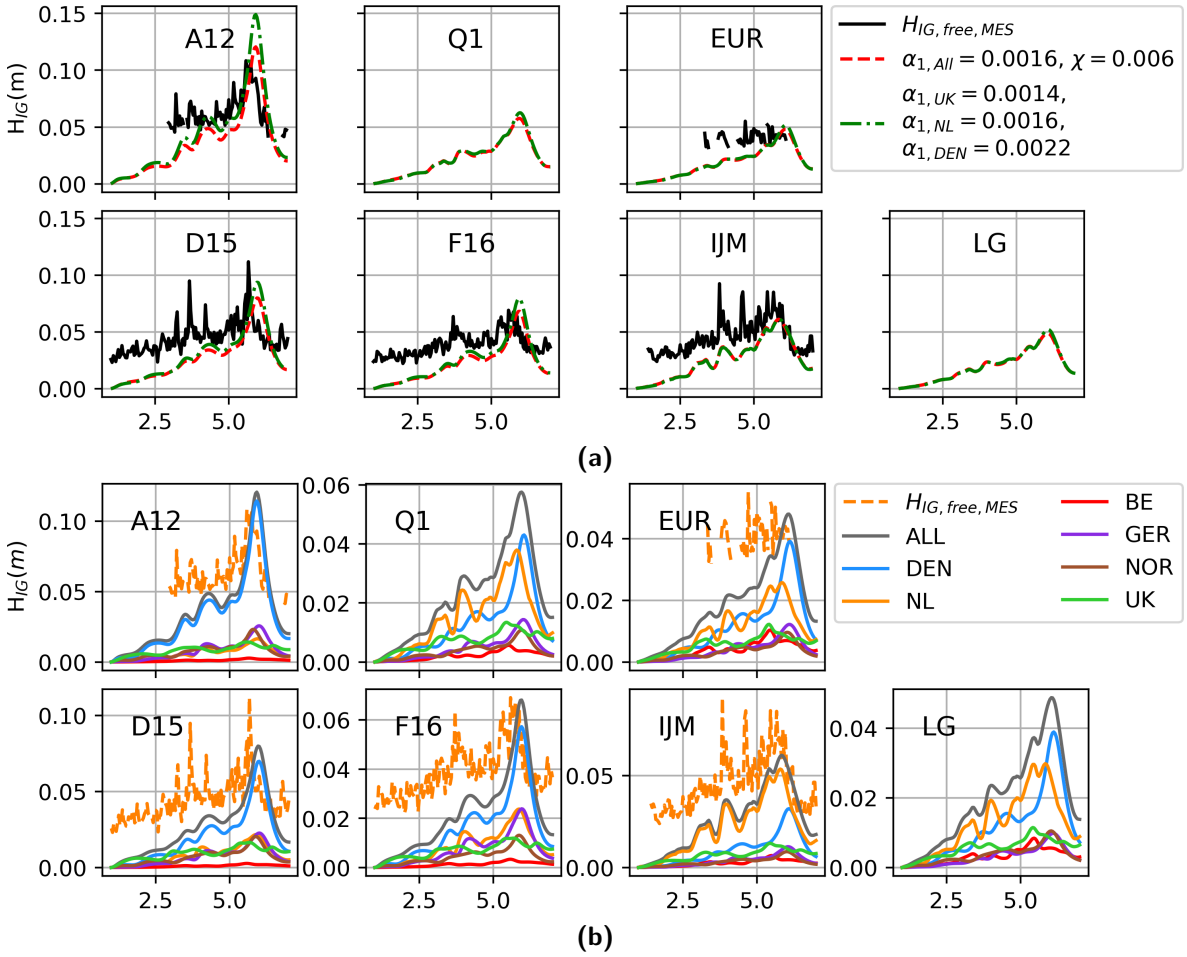

Figure A-13: The variation of H_{IG} at same scales with 2 combinations indicated in legend (a), and the contributions from individual coasts to observed free IG wave height at different scales (b) in 7 observation stations over storm Berit.

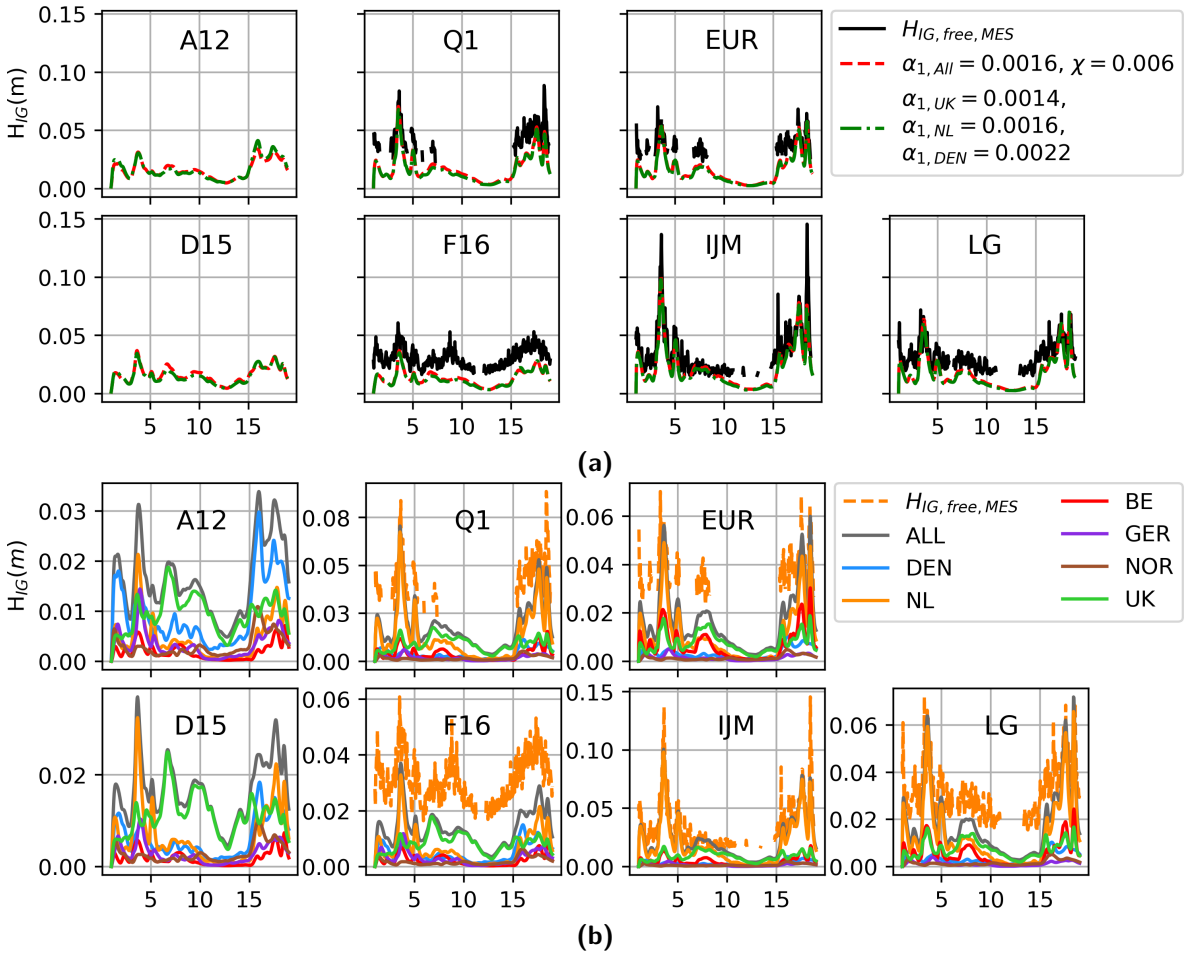

Figure A-14: The variation of H_{IG} at same scales with 2 combinations indicated in legend (a), and the contributions from individual coasts to observed free IG wave height at different scales (b) in 7 observation stations over storm Eleanor.

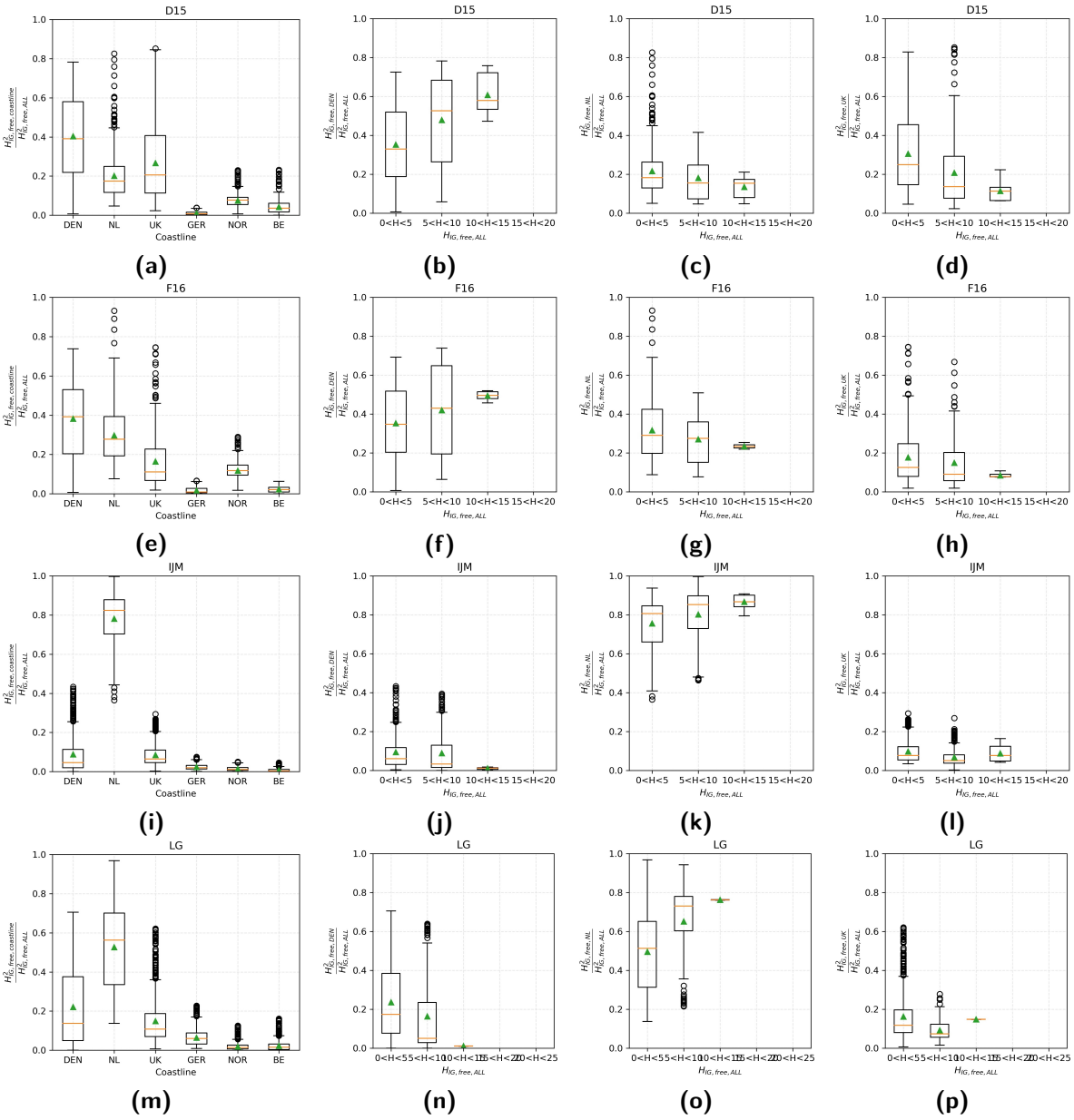

Figure A-15: Box-whisker plots of the proportion of original free IG energy as a function of IG wave height at three stations

Bibliography

[1] Fabrice Ardhuin, Arshad Rawat, and Jerome Aucan. A numerical model for free infragravity waves: Definition and validation at regional and global scales. *Ocean Modelling*, 77:20, 2014.

[2] Martin Austin, Tim Scott, Jeff Brown, Jenna Brown, Jamie MacMahan, Gerd Masselink, and Paul Russell. Temporal observations of rip current circulation on a macro-tidal beach. *Continental Shelf Research*, 30(9):1149–1165, 2010.

[3] JA Battjes, HJ Bakkenes, TT Janssen, and Ap R van Dongeren. Shoaling of subharmonic gravity waves. *Journal of Geophysical Research: Oceans*, 109(C2), 2004.

[4] J Baumann, Eric Chaumillon, X Bertin, J-L Schneider, B Guillot, and M Schmutz. Importance of infragravity waves for the generation of washover deposits. *Marine Geology*, 391:20–35, 2017.

[5] Xavier Bertin, Anouk De Bakker, Ap Van Dongeren, Giovanni Coco, Gael Andre, Fabrice Ardhuin, Philippe Bonneton, Frederic Bouchette, Bruno Castelle, Wayne C Crawford, et al. Infragravity waves: From driving mechanisms to impacts. *Earth-Science Reviews*, 177:774–799, 2018.

[6] Xavier Bertin and Maitane Olabarrieta. Relevance of infragravity waves in a wave-dominated inlet. *Journal of Geophysical Research: Oceans*, 121(8):5418–5435, 2016.

[7] Judith Bosboom and Marcel JF Stive. *Coastal dynamics I: lectures notes CIE4305*. 2012.

[8] AJ Bowen and DA Huntley. Waves, long waves and nearshore morphology. *Marine Geology*, 60(1-4):1–13, 1984.

[9] Anthony J Bowen and Douglas L Inman. Edge waves and crescentic bars. *Journal of Geophysical Research*, 76(36):8662–8671, 1971.

[10] Peter D Bromirski, Olga V Sergienko, and Douglas R MacAyeal. Transoceanic infragravity waves impacting antarctic ice shelves. *Geophysical Research Letters*, 37(2), 2010.

[11] Stephanie Contardo, Ryan J Lowe, Jeff E Hansen, Dirk P Rijnsdorp, François Dufois, and Graham Symonds. Free and forced components of shoaling long waves in the absence of short-wave breaking. *Journal of Physical Oceanography*, 51(5):1465–1487, 2021.

[12] A. T. M. de Bakker, M. F. S. Tissier, and B. G. Ruessink. Beach steepness effects on nonlinear infragravity-wave interactions: A numerical study. *Journal of Geophysical Research: Oceans*, 121(1):554–570, 2016.

[13] ATM De Bakker, JA Brinkkemper, Florian Van der Steen, MFS Tissier, and BG Ruessink. Cross-shore sand transport by infragravity waves as a function of beach steepness. *Journal of Geophysical Research: Earth Surface*, 121(10):1786–1799, 2016.

[14] ATM De Bakker, MFS Tissier, and BG Ruessink. Shoreline dissipation of infragravity waves. *Continental Shelf Research*, 72:73–82, 2014.

[15] MPC De Jong and JA Battjes. Low-frequency sea waves generated by atmospheric convection cells. *Journal of Geophysical Research: Oceans*, 109(C1), 2004.

[16] MPC De Jong, LH Holthuijsen, and JA Battjes. Generation of seiches by cold fronts over the southern north sea. *Journal of Geophysical Research: Oceans*, 108(C4), 2003.

[17] Ryan B Elandt, Louis-Alexandre Couston, Ruth A Lambert, and Mohammad-Reza Alam. Bragg resonance of gravity waves and ocean renewable energy. In *Integrated Systems: Innovations and Applications*, pages 211–225. Springer, 2015.

[18] Dimitrios A Evangelidis. Infragravity waves on the continental shelf. Technical report, NAVAL POSTGRADUATE SCHOOL MONTEREY CA, 1996.

[19] Julia W Fiedler, Pieter B Smit, Katherine L Brodie, Jesse McNinch, and RT Guza. The offshore boundary condition in surf zone modeling. *Coastal Engineering*, 143:12–20, 2019.

[20] Jens Figlus, Nobuhisa Kobayashi, Christine Gralher, and Vicente Iranzo. Wave overtopping and overwash of dunes. *Journal of Waterway, Port, Coastal, and Ocean Engineering*, 137(1):26–33, 2011.

[21] Jean Henri Filloux. Pressure fluctuations on the open ocean floor over a broad frequency range: New program and early results. *Journal of Physical Oceanography*, 10(12):1959–1971, 1980.

[22] Brent Gallagher. Generation of surf beat by non-linear wave interactions. *Journal of Fluid Mechanics*, 49(1):1–20, 1971.

[23] Edith L Gallagher, Steve Elgar, and RT Guza. Observations of sand bar evolution on a natural beach. *Journal of Geophysical Research: Oceans*, 103(C2):3203–3215, 1998.

[24] Rafael MC Guedes, Karin R Bryan, and Giovanni Coco. Observations of wave energy fluxes and swash motions on a low-sloping, dissipative beach. *Journal of geophysical research: Oceans*, 118(7):3651–3669, 2013.

[25] Robert T Guza and Edward B Thornton. Swash oscillations on a natural beach. *Journal of Geophysical Research: Oceans*, 87(C1):483–491, 1982.

[26] RT Guza and Edward B Thornton. Observations of surf beat. *Journal of Geophysical Research: Oceans*, 90(C2):3161–3172, 1985.

[27] Klaus Hasselmann. On the non-linear energy transfer in a gravity-wave spectrum part 1. general theory. *Journal of Fluid Mechanics*, 12(4):481–500, 1962.

[28] Klaus F Hasselmann, Tim P Barnett, E Bouws, H Carlson, David E Cartwright, K Eake, JA Euring, A Gicnapp, DE Hasselmann, P Kruseman, et al. Measurements of wind-wave growth and swell decay during the joint north sea wave project (jonswap). *Ergaenzungsheft zur Deutschen Hydrographischen Zeitschrift, Reihe A*, 1973.

[29] Miles O Hayes. General morphology and sediment patterns in tidal inlets. *Sedimentary geology*, 26(1-3):139–156, 1980.

[30] Stephen M Henderson, RT Guza, Steve Elgar, THC Herbers, and AJ Bowen. Nonlinear generation and loss of infragravity wave energy. *Journal of Geophysical Research: Oceans*, 111(C12), 2006.

[31] THC Herbers, Steve Elgar, and RT Guza. Generation and propagation of infragravity waves. *Journal of Geophysical Research: Oceans*, 100(C12):24863–24872, 1995.

[32] Leo H Holthuijsen. *Waves in oceanic and coastal waters*. Cambridge university press, 2010.

[33] DA Huntley and AJ Bowen. Comparison of the hydrodynamics of steep and shallow beaches. In *Nearshore sediment dynamics and sedimentation*, pages 69–109. Wiley London, 1975.

[34] Kris Inch, Mark Davidson, Gerd Masselink, and Paul Russell. Observations of nearshore infragravity wave dynamics under high energy swell and wind-wave conditions. *Continental Shelf Research*, 138:19–31, 2017.

[35] TT Janssen, JA Battjes, and AR Van Dongeren. Long waves induced by short-wave groups over a sloping bottom. *Journal of Geophysical Research: Oceans*, 108(C8), 2003.

[36] Gerbrand J Komen, Luigi Cavaleri, Mark Donelan, Klaus Hasselmann, S Hasselmann, and PAEM Janssen. *Dynamics and modelling of ocean waves*. 1996.

[37] Shaowu Li, Zhiling Liao, Ye Liu, and Qingping Zou. Evolution of infragravity waves over a shoal under nonbreaking conditions. *Journal of Geophysical Research: Oceans*, 125(8):e2019JC015864, 2020.

[38] Michael S Longuet-Higgins and RW Stewart. Radiation stress and mass transport in gravity waves, with application to 'surf beats'. *Journal of Fluid Mechanics*, 13(4):481–504, 1962.

[39] Jamie H MacMahan, Ed B Thornton, and Ad JHM Reniers. Rip current review. *Coastal Engineering*, 53(2-3):191–208, 2006.

[40] Hajime Mase. Frequency down-shift of swash oscillations compared to incident waves. *Journal of Hydraulic Research*, 33(3):397–411, 1995.

[41] Gerhard Masselink. Group bound long waves as a source of infragravity energy in the surf zone. *Continental Shelf Research*, 15(13):1525–1547, 1995.

[42] Ana Matias, Jon J Williams, Gerhard Masselink, and Óscar Ferreira. Overwash threshold for gravel barriers. *Coastal Engineering*, 63:48–61, 2012.

[43] Y. Matsuba, T. Shimozono, and S. Sato. Wave-breaking modulation by infragravity waves during an extreme typhoon. *PLoS One*, 15(4):e0231242, 2020.

[44] Robert T McCall, JSM Van Thiel De Vries, NG Plant, AR Van Dongeren, JA Roelvink, DM Thompson, and AJHM Reniers. Two-dimensional time dependent hurricane overwash and erosion modeling at santa rosa island. *Coastal Engineering*, 57(7):668–683, 2010.

[45] Robert Timothy McCall. Process-based modelling of storm impacts on gravel coasts. 2015.

[46] Okey Nwogu and Zeki Demirbilek. Infragravity wave motions and runup over shallow fringing reefs. *Journal of waterway, port, coastal, and ocean engineering*, 136(6):295–305, 2010.

[47] Michele Okihiro, RT Guza, and RJ Seymour. Excitation of seiche observed in a small harbor. *Journal of Geophysical Research: Oceans*, 98(C10):18201–18211, 1993.

[48] Joan Oltman-Shay and RT Guza. Infragravity edge wave observations on two california beaches. *Journal of Physical Oceanography*, 17(5):644–663, 1987.

[49] Arshad Rawat, Fabrice Ardhuin, Valerie Ballu, Wayne Crawford, Carlos Corela, and Jerome Aucan. Infragravity waves across the oceans. *Geophysical Research Letters*, 41(22):7957–7963, 2014.

[50] A. J. H. M. Reniers, A. R. van Dongeren, J. A. Battjes, and E. B. Thornton. Linear modeling of infragravity waves during delilah. *Journal of Geophysical Research: Oceans*, 107(C10):1–1–1–18, 2002.

[51] Ad J.H.M. Reniers, Remy Naporowski, Marion F. S. Tissier, Matthieu A. de Schipper, Gal Akrish, and Dirk P. Rijnsdorp. North sea infragravity wave observations. *Journal of Marine Science and Engineering*, 9(2):141, 2021.

[52] A.J.H.M. Reniers, M.J. Groenewegen, K.C. Ewans, S. Masterton, G.S. Stelling, and J. Meek. Estimation of infragravity waves at intermediate water depth. *Coastal Engineering*, 57(1):52–61, 2010.

[53] Dirk P Rijnsdorp, Ad JHM Reniers, and Marcel Zijlema. Free infragravity waves in the north sea. *Journal of Geophysical Research: Oceans*, page e2021JC017368, 2021.

[54] Dirk P Rijnsdorp, Gerben Ruessink, and Marcel Zijlema. Infragravity-wave dynamics in a barred coastal region, a numerical study. *Journal of Geophysical Research: Oceans*, 120(6):4068–4089, 2015.

[55] Volker Roeber and Jeremy D Bricker. Destructive tsunami-like wave generated by surf beat over a coral reef during typhoon haiyan. *Nature communications*, 6(1):1–9, 2015.

[56] Dano Roelvink, Ad Reniers, AP Van Dongeren, Jaap Van Thiel De Vries, Robert McCall, and Jamie Lescinski. Modelling storm impacts on beaches, dunes and barrier islands. *Coastal engineering*, 56(11-12):1133–1152, 2009.

[57] Andrea Ruju, Javier L Lara, and Inigo J Losada. Radiation stress and low-frequency energy balance within the surf zone: A numerical approach. *Coastal engineering*, 68:44–55, 2012.

[58] Ted Scambos, Helen Amanda Fricker, Cheng-Chien Liu, Jennifer Bohlander, James Fastook, Aitbala Sargent, Robert Massom, and An-Ming Wu. Ice shelf disintegration by plate bending and hydro-fracture: Satellite observations and model results of the 2008 wilkins ice shelf break-ups. *Earth and Planetary Science Letters*, 280(1-4):51–60, 2009.

[59] Leo Sembiring, Ap Van Dongeren, Gundula Winter, and Dano Roelvink. Dynamic modelling of rip currents for swimmer safety on a wind-sea–dominated mesotidal beach. *Journal of Coastal Research*, 32(2):339–353, 2016.

[60] Nadia Senechal, Philippe Bonneton, and Helene Dupuis. Field observations of irregular wave transformation in the surf zone. In *Coastal Dynamics' 01*, pages 62–71, 2001.

[61] Takenori Shimozono, Yoshimitsu Tajima, Andrew B Kennedy, Hisamichi Nobuoka, Jun Sasaki, and Shinji Sato. Combined infragravity wave and sea-swell runup over fringing reefs by super typhoon haiyan. *Journal of Geophysical Research: Oceans*, 120(6):4463–4486, 2015.

[62] PB Smit, TT Janssen, THC Herbers, T Taira, and BA Romanowicz. Infragravity wave radiation across the shelf break. *Journal of Geophysical Research: Oceans*, 123(7):4483–4490, 2018.

[63] Graham Symonds, David A Huntley, and Anthony J Bowen. Two-dimensional surf beat: Long wave generation by a time-varying breakpoint. *Journal of Geophysical Research: Oceans*, 87(C1):492–498, 1982.

[64] Graham Symonds and R Ranasinghe. On the formation of rip currents on a plane beach. In *Coastal Engineering 2000*, pages 468–481. 2001.

[65] Jim Thomson, Steve Elgar, Britt Raubenheimer, THC Herbers, and RT Guza. Tidal modulation of infragravity waves via nonlinear energy losses in the surfzone. *Geophysical Research Letters*, 33(5), 2006.

[66] MFS Tissier, Philippe Bonneton, and BG Ruessink. Infragravity waves and bore merging. In *Proceedings Coastal Dynamics 2017*, pages 451–460, 2017.

[67] Ap Van Dongeren, Martijn De Jong, Cock Van der Lem, Alex Van Deyzen, and Joost Den Bieman. Review of long wave dynamics over reefs and into ports with implication for port operations. *Journal of Marine Science and Engineering*, 4(1):12, 2016.

[68] ARJA Van Dongeren, J Battjes, T Janssen, J Van Noorloos, K Steenhauer, G Steenbergen, and AJHM Reniers. Shoaling and shoreline dissipation of low-frequency waves. *Journal of Geophysical Research: Oceans*, 112(C2), 2007.

[69] Leo C van Rijn. Prediction of dune erosion due to storms. *Coastal Engineering*, 56(4):441–457, 2009.

[70] JSM Van Thiel de Vries. Dune erosion during storm surges. 2009.

[71] T Vrećica, R Soffer, and Y Toledo. Infragravity wave generation by wind gusts. *Geophysical Research Letters*, 46(16):9728–9738, 2019.

[72] Anna Wargula, Britt Raubenheimer, and Steve Elgar. Wave-driven along-channel subtidal flows in a well-mixed ocean inlet. *Journal of Geophysical Research: Oceans*, 119(5):2987–3001, 2014.

[73] Gerald Beresford Whitham. *Linear and nonlinear waves*, volume 42. John Wiley & Sons, 2011.

[74] Megan E Williams and Mark T Stacey. Tidally discontinuous ocean forcing in bar-built estuaries: The interaction of tides, infragravity motions, and frictional control. *Journal of Geophysical Research: Oceans*, 121(1):571–585, 2016.

[75] G Winter, RJ Lowe, G Symonds, JE Hansen, and AR Van Dongeren. Standing infragravity waves over an alongshore irregular rocky bathymetry. *Journal of Geophysical Research: Oceans*, 122(6):4868–4885, 2017.

[76] Lynn D Wright and Andrew D Short. Morphodynamic variability of surf zones and beaches: a synthesis. *Marine geology*, 56(1-4):93–118, 1984.

[77] M Zijlema, G Ph Van Vledder, and LH Holthuijsen. Bottom friction and wind drag for wave models. *Coastal Engineering*, 65:19–26, 2012.